Using iPSC-derived cortical organoids to study disease mechanisms of POLG-disease and explore new therapeutic strategies

Bjørn Christian Lundberg

This thesis is submitted in partial fulfilment of the requirements for the degree of Master in Biomedical Sciences.

Department of Biomedicine / Department of Clinical Medicine (K1)

University of Bergen

Spring 2023

Acknowledgements

Table of Contents

Abbreviations

AHS - Alpers-Huttenlocher Syndrome

ANS – Ataxia Neuropathy Spectrum

ATP – Adenine Triphosphate

C1 – Complex I

cDNA – Complementary DNA

CJ – Cristae Junction

CO – EM Organoid

CO2 – Carbon Dioxide

CoQ - Ubiquinone

Cyt.C – Cytochrome C

DA GLU Neuron – Dopamine-Glutamine Co-expressing Neuron

EB – Embryoid Body

ESC – Embryonic Stem Cell

ETC – Electron Transport Chain

FADH2 – Flavin adenine dinucleotide

FBS – Fetal Bovine Serum

FSC-A – Forward Scatter Area

FSC-H – Forward Scatter Height

GFAP – Glial Fibrillary Acidic Protein

GTP – Guanosine Triphosphate

H2O2 – Hydrogen Peroxide

IBM – Inner Boundary Membrane

IMM – Inner Mitochondrial Membrane

IMS – Inter Membrane Space

IntDen - Integrated Density

iPSC – Induced Pluripotent Stem Cell

L/D – Live/Dead

MAP2 – Microtubule Associated Protein

MFI – Median Fluorescent Intensity

mtDNA – Mitochondrial DNA

mtSSB – Mitochondrial Single Strand Binding Protein

NAD+ - Nicotinamide Adenine Dinucleotide

NADH - Nicotinamide adenine dinucleotide

NAM – Nicotinamide

NAMPT – Nicotinamide Phosphoribosyl Transferase

NDM – Neural Differentiation Medium

NDM-A – Neural Differentiation Medium – Vitamin A

nDNA – Nuclear DNA

NIM – Neural Induction Medium

NR – Nicotinamide Riboside

OMM – Outer Mitochondrial Membrane

OXPHOS – Oxidative Phosphorylation

PEO - Progressive External Ophthalmoplegia

POLG – Polymerase Gamma (gene)

POLRMT – Mitochondrial RNA Polymerase

Pol-γ – Polymerase Gamma (protein)

Pol-γA – Polymerase Gamma Catalytic Subunit

Pol-γB – Polymerase Gamma Accessory Subunit

PSC – Pluripotent Stem Cell

RNA – Ribonucleic Acid

mRNA – Messenger RNA

rRNA – Ribosomal RNA

tRNA – Transfer RNA

ROS – Reactive Oxygen Species

RT – Room Temperature

SOX2 – Sex-determining Region Box-2

SSC-A – Side Scatter Area

SSC-H – Side Scatter Height

TFAM – Mitochondrial Transcription factor A

VDAC – Voltage Dependent Anion Channel

Summary

POLG-related diseases are a set of severe mitochondrial myopathies caused by a mutation in the *POLG* gene. The *POLG* gene encodes for the catalytic subunit of the mitochondrial DNA (mtDNA) polymerase gamma (Pol-γ). Pol-γ is responsible for the replication and maintenance of mtDNA, and dysfunction of Pol-γ due to mutations in the *POLG* gene leads to mtDNA depletion and an accumulation of mtDNA deletions over time. This impairment of the mtDNA leads to dysfunctions in the mitochondrial respiratory chain, leading to severe cellular energy depletion as a result of reduced adenine triphosphate (ATP) production.

POLG-related diseases have a large degree of variance in the age that symptoms manifest and the severity of the symptoms. POLG-related diseases manifest mainly in postmitotic tissues such as those of the brain, skeletal muscle and liver, and mutations in the *POLG* gene have been associated with several disorders such as Alpers-Huttenlocher syndrome (AHS), progressive external ophthalmoplegia (PEO), and childhood myocerebrohepatopathy syndrome (MCHS). POLG-related disorders often manifest severe neurological symptoms, and there are currently no effective treatments available for POLG-diseases.

One of the main challenges in conducting studies of POLG-related disease is the limited availability of patient tissues available for study. To overcome this challenge, we have in this study developed a method for generating cortical organoids (COs) from patient derived induced pluripotent stem cells (iPSCs). In this study we have generated COs from iPSCs from a patient carrying the mutations p.Ala467Thr and p.Trp748Ser, known to be associated with several POLG-related neurodegenerative disorders including AHS. In this thesis we attempt to determine the ability of generated POLG COs to accurately model the phenotypic features of POLG-disease, as well as an initial investigation into nicotinamide riboside (NR) as a potential novel therapeutic treatment option.

We discovered distinct differences in the growth patterns of POLG COs, notably a tendency for POLG COs to fuse together in culture at a far greater rate than the control. Flow cytometry analysis also revealed POLG COs had lowered cell viability, and overall decreased expression of markers indicating depletion of neuronal mass, loss of mitochondrial mass, complex I (C1) depletion and loss of mtDNA volume. However, when normalizing the mitochondrial mass to the

neuronal mass, and normalizing mtDNA volume and C1 to the mitochondrial mass a reduction was no longer observed.

NR supplementation was seen to have a rescuing effect on the POLG COs, increasing cell viability and increasing expression of markers indicating increased overall neuronal mass, mitochondrial mass, C1 and mtDNA. But the same trend was not observed in normalized values.

This study is part of our preliminary investigations into the utilization of COs as a potential modeling system for POLG-related disease, as such this study was conducted on a limited number of repeats and lacks any statistical analysis. Therefore, it is important to keep in mind that these are preliminary findings, and that further investigation is required to confirm if these findings are significant. Furthermore, the methodology revealed a certain degree of limitations including difficulties with imaging, variable staining efficiency, and an overall low viable cell population throughout samples showing that there is still a need to improve and optimize our protocols. However, the findings of this study have given valuable insight into the cellular impacts of POLG mutations and serve as a foundation for further research in this field. In conclusion, this study has opened a new frontier in the study of POLG and other mitochondrial diseases and holds promise for the development of novel therapeutic strategies.

1. Introduction

Mitochondria are essential components to human life, playing key roles in energy production and other metabolic functions. Mitochondrial dysfunctions can significantly affect an individual's health, and in extreme cases, may be fatal. Mitochondrial diseases are among the most frequently occurring metabolic disorders, affecting approximately 1 in 5000 individuals (Parikh et al., 2015). The most common cause of mitochondrial diseases is the mutations of the *POLG* gene, which encodes for the catalytic Pol-γ, an enzyme crucial for the replication and repair of mtDNA. To date, over 300 pathogenic variants have been identified in the *POLG* gene (Nicholas Russo et al., 2022). Depending on the specific mutation present, a variety of symptoms and syndromes may arise, with vast differences in age of onset, severity of disease, and lethality. Diseases induced by mutations in the *POLG* gene are collectively referred to as POLG-related diseases. Noteworthy syndromes associated with POLG-disease include AHS, progressive external ophthalmoplegia, and childhood myocerebrohepatopathy syndrome (Longley et al., 2005; Stumpf et al., 2013). These diseases often manifest symptoms in the brain, muscles, and liver. Neurological symptoms are typically severe and may include seizures, cognitive impairments, and loss of motor functions. Unfortunately, no effective treatments currently exist for POLG-related diseases, and research progress is hampered by the scarcity of patient tissues available for study.

This thesis is part of a broader project aimed at developing a model system for investigation of POLG-diseases. The system under development leverages COs derived from iPSCs to model and study POLG-related diseases and explore new therapeutic strategies.

1.1 Mitochondria and mitochondrial function

1.1.1 Mitochondrial structure

The mitochondria, a ubiquitous organelle in eukaryotic organisms, is often referred to as the 'powerhouse of the cell' due to its essential role in generating ATP - the primary energy source of the cell. This energy production is carried out through a process known as oxidative phosphorylation (OXPHOS). The mitochondria possess unique characteristics that distinguish it from other organelles, such as a double membrane structure and its own circular DNA – mtDNA, which regulates its functions.

The mitochondrion is enclosed within two distinct phospholipid membranes: the inner mitochondrial membrane (IMM) and the outer mitochondrial membrane (OMM) (**Figure 1.1**). Each membrane has unique properties in terms of permeability, form, and function. The OMM permits passive transport of small molecules and ions across the membrane through voltage dependent anion channels (VDAC). On the other hand, the inner membrane is far less permeable, allowing only passage of small molecules like water, oxygen and CO2 and heavily relying on active transport proteins for transferring substances across it (Protasoni and Zeviani, 2021). The IMM hosts mitochondrial complexes I-V, the driving forces of the OXPHOS process. IMM's efficiency is enhanced by its folded structure, known as cristae, which greatly increases the surface area available for OXPHOS. The area within the IMM is called the mitochondrial matrix, while the space between the mitochondrial membranes is known as the intermembrane space (IMS). The mitochondria's unique attributes are believed to have emerged from its origin as an endosymbiotic bacterium within early eukaryotic cells. (Cavalier-Smith, 2006).

Mitochondrial morphology within cells varies greatly, often forming extensive, branching tubular structures. The dynamic structures continually undergo fusion and fission in response to shifts in energy demand and nutrient availability (Tilokani et al., 2018). Mitochondrial fusion facilitates mitochondrial proteins, metabolites and mtDNA to be shared between mitochondrial units. Mitochondrial fragmentation, on the other hand, enables the removal of dysfunctional or damaged mitochondria via a degradation process known as mitophagy. Additionally, fragmentation aids in mitochondrial motility, ensuring distribution throughout various regions of the cell. Mitochondrial transport is a critical component to ensure energy production meets demand in the right time and place, especially crucial in neuronal cells where mitochondrial

distribution along the axon and to the synaptic terminals is fundamental for proper function (Hollenbeck and Saxton, 2005). Mitochondrial motility is mediated through microtubules structures spanning the cell, with motor proteins driving the mitochondrial transport along the structures (Yi et al., 2004).
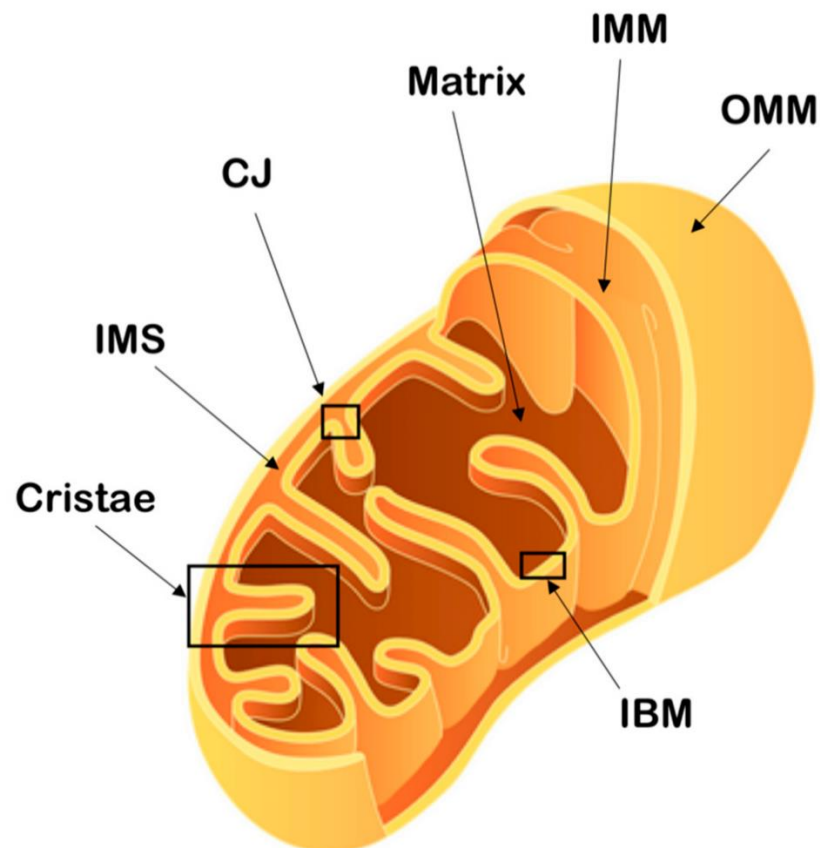
Figure 1.1 Overview of mitochondrial membrane structure. The Outer mitochondrial membrane (OMM), the Inner mitochondrial membrane (IMM), and the Intermembrane space (IMS) are located between the OMM and IMM. Cristae are folds of the IMM. Cristae junctions (CJ) mark the opening of the Cristae into the IMS. The area within the IMM is called the matrix. Inner boundary membrane (IBM) are sections of the IMM that run parallel to the OMM. Figure from (Protasoni and Zeviani, 2021).

1.1.2 Mitochondrial functions

The main function of the mitochondria is often regarded as its role as energy producer, by the formation of ATP. However, mitochondria also serve important functions in adjusting the calcium concentration of the cell, and as a regulator of apoptosis.

The production of ATP, a fundamental aspect of eukaryotic life, is a sophisticated, multi-stage process. It starts with the degradation of glucose into carbon dioxide (CO_2) and water through a series of steps. The first step of this process, glycolysis, takes place in cell cytoplasm. Glycolysis is a mitochondrial-independent and oxygen-free process that breaks down glucose into two pyruvate molecules, generating a net of two ATP molecules While glycolysis produces less ATP compared to OXPHOS, it does provide a limited source of energy production under anerobic circumstances.

However, the primary ATP generation process occurs within the mitochondria, in a cycle called the Krebs cycle. This cycle, which is oxygen-dependent, uses pyruvate from glycolysis and coenzyme-A to create acetyl coenzyme-A. Acetyl coenzyme-A enters the Krebs cycle by combining it with oxaloacetic acid to produce citric acid. Through a series of complex redox reactions, citric acid is then degraded back into oxaloacetic acid, producing six nicotinamide adenine dinucleotide (NADH), two flavine adenine dinucleotide (FADH2) and one guanosine triphosphate (GTP) as byproducts. The cycle can then be repeated with the addition of another acetyl coenzyme-A molecule. The NADH and FADH2 produced in the Krebs cycle are utilized as electron donors for the next stage of ATP production, the electron transport chain (ETC). Thus, through these interconnected pathways, the cell is able to efficiently convert glucose into the energy-rich molecule ATP.

The ETC (**Figure 1.2**), located within the IMM, is a fundamental component of oxidative phosphorylation, responsible for generating the majority of cellular ATP. The ETC comprises five distinct protein complexes, designated I-V. The initial four complexes (I, II, III, and IV) play crucial roles in creating and sustaining the proton gradient required for ATP synthesis. They accomplish this by pumping protons from the mitochondrial matrix into the IMS. This process involves structural changes within the respiratory chain complexes, although the precise mechanisms are not yet fully understood. The resultant proton gradient forms the driving force for ATP production. Complex V, also known as ATP synthase, harnesses this energy to

phosphorylate ADP, thereby producing ATP. The starting point of the ETC is the donation of electrons from NADH. These electrons are transferred from one complex to another through a series of oxidation and reduction reactions, facilitated by intermediate electron carriers that can permeate the membrane. Through these interconnected stages, the ETC effectively converts the energy derived from NADH into usable ATP.
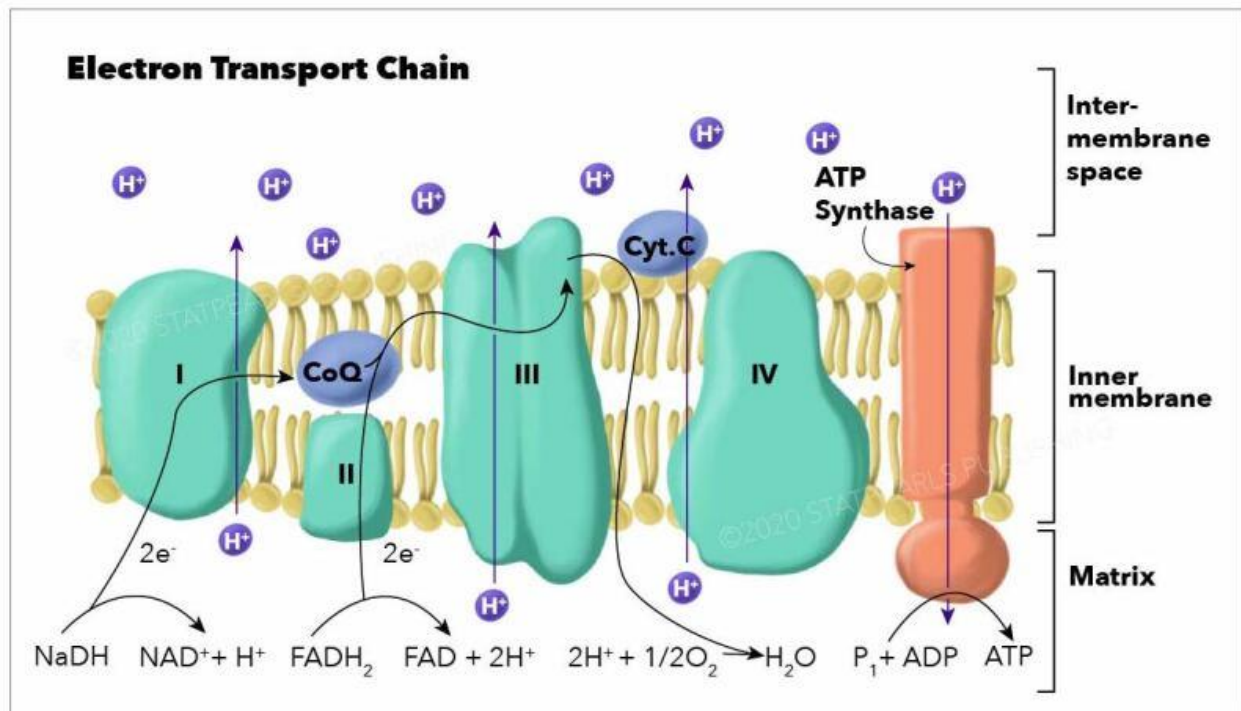
Figure 1.2 Representation of the ETC. Complexes I, III, and IV create the proton gradient by transporting H+ across the IMM to the IMS. NADH serves as the electron donor for C1. FADH2 serves as the electron donor for complex II. Ubiquinone (CoQ) and Cytochrome C (Cyt.C) serve as intermediates for electron transport. ATP synthase forms ATP by phosphorylation of ADP using the proton gradient as an energy source, by allowing protons to diffuse back into the matrix. Image from (Ahmad et al., 2023).

C1, also known as NADH dehydrogenase, represents the initial stage of the ETC. The complex serves as the electron acceptor for NADH, through reduction to nicotinamide adenine dinucleotide (NAD+). The electrons are transported through the complex via a series of iron-sulfur clusters, ending in donating the electrons further to ubiquinone converting it to ubiquinol. The energy transfer from C1 to ubiquinone also facilitates the transport of protons across the IMM, facilitating the buildup of the proton gradient across the membrane (Vinothkumar et al.,

2014). C1 is a substantial structure assembled from 44 different protein subunits. These subunits originate from both mitochondrial and nuclear encoded proteins. The assembly of C1 is a multilayered process that demands numerous assembly factors (Guerrero-Castillo et al., 2017).

In addition to ATP production, mitochondria also contribute significantly to cellular homeostasis through calcium regulation and the production of reactive oxygen species (ROS). Calcium primarily acting as a signaling molecule, is intricately managed within cells, and mitochondria function as a critical storage center for it (Berridge et al., 2003). This reservoir of calcium in the mitochondria plays a crucial role, particularly in neurons, where it maintains the electrochemical gradient that drives the action potential (Walters and Usachev, 2023).

Another pivotal function f mitochondria lies in the generation of ROS, which participate in various signaling pathway (D'Autréaux and Toledano, 2007). However, ROS are double-edged swords. While they serve functional roles at moderate levels, their overproduction can lead to cellular damage, referred to as oxidative stress. ROS, due to their high reactivity, can inflict oxidative damage to lipids, proteins, and DNA, causing DNA mutations and, over time, potentially contributing to aging-related health issues (Pizzino et al., 2017). Oxidative stress, a condition caused by the overproduction of ROS, occurs when the generation of these highly reactive molecules exceeds the cell's antioxidant defense capacity. This overabundance of ROS can trigger severe health complications and is believed to be a key contributor to the detrimental effects associated with aging (Balaban et al., 2005). This oxidative stress has particularly pronounced effects on energy-intensive, postmitotic tissues, such as neurons, muscles, and liver cells. It's theorized that these tissues, in response to oxidative stress, are more inclined to exclude defective mitochondria during mitosis, which can impact cellular function Remarkably, mitochondria is considered the primary source of ROS, accounting for nearly 90% found within cells (Balaban et al., 2005). The generation of ROS in mitochondria mainly stems from electron leakage from complexes I and III, which reacts with water to form hydrogen peroxide (H_2O_2).

1.1.3 MtDNA and its replication

The mitochondrial genome (**Figure 1.3**), also known as mtDNA, resides in the mitochondrial matrix, with each mitochondrion housing hundreds to thousands of copies. Remarkably, the mtDNA encodes 37 different genes, which include 11 genes that produce messenger ribonucleic acid (mRNA) translating into 13 proteins integral to the ECT complexes I, III, IV, and V. In

addition, 2 ribosomal RNAs (rRNAs) and 22 transfer RNAs (tRNAs) are also encoded by the mtDNA (Protasoni and Zeviani, 2021). Despite the relatively small number of genes encoded by the mtDNA, the function of mitochondria involves nearly 1200 different proteins (Calvo et al., 2016). This underscores the importance of the nuclear genome in mitochondrial regulation, with a large proportion of mitochondrial proteins being produced in the nucleus before being transported into the mitochondria. For instance, none of the proteins associated with the respiratory chain complex II are encoded by the mtDNA; instead, they are entirely regulated by the nuclear genome.

One intriguing aspect of mtDNA is its exclusively maternal inheritance, as an individual's mitochondrial population originates from those present in the egg at conception. Consequently, mitochondrial defects are typically passed down through the maternal lineage. Moreover, because each cell contains numerous copies of mtDNA, the impact of mutations differs from that in nuclear DNA. The effect of a mutation is often dependent on the proportion of mtDNA copies carrying that mutation, which can result in highly variable expression of mitochondrial defects. This variability can lead to a wide range of severity in the manifestation of mitochondrial deficiencies and can even result in spatially localized deficiencies (Chinnery, 1993).
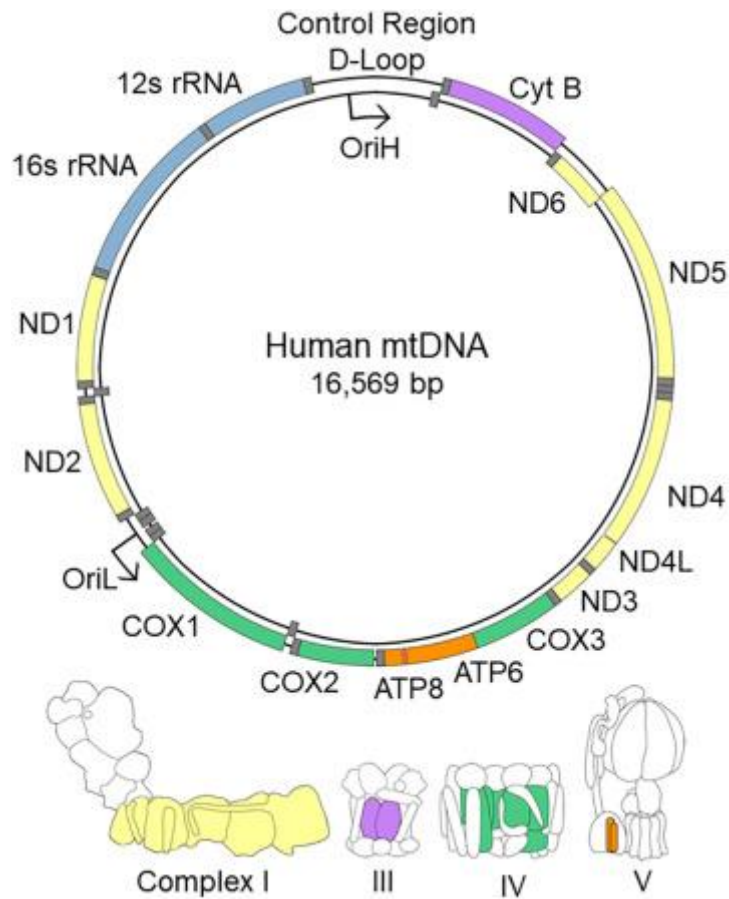
Figure 1.3 Representation of the mitochondrial genome. The mitochondrial genome consists of 16,569 base pairs (bp). Genes associated with respiratory chain complexes are highlighted; Yellow C1, Purple complex III, green complex IV, and orange for complex V. Highlighted areas of structural representation of respiratory chain complexes shows localization of proteins encoded in mitochondrial genome. Image from (Chocron et al., 2019).

The mtDNA exhibits a circular structure resembling that of bacterial nucleoids and consists of a heavy chain strand and a light chain strand (**Figure 1.3**) (Alberts et al., 2002). Compared to the nuclear DNA (nDNA) replication, The machinery for mtDNA replication is somewhat simplified. The fundamental principles, though, are identical, involving the unwinding of double-stranded DNA into single strands, polymerization in the 5' to 3' direction, with leading strand and a lagging strand synthesis (Bogenhagen and Clayton, 1974). The initiation of mtDNA replication relies on the mitochondrial helicase TWINKLE, to unwind the mtDNA into single strands, thereby forming the mtDNA replication fork. This process facilitates binding of DNA polymerase gamma Pol-γ to the single-strand DNA and kick-starts polymerization (Fusté et al., 2010).

Pol-γ, an essential component for mtDNA replication and maintenance, comprises a catalytic subunit (Pol-γA) and two accessory subunits (Pol-γB). All the genes of Pol-γ are encoded in the nuclear genome, with *POLG*-gene encoding Pol-γA and *POLG*2-gene encoding Pol-γB (Kaguni, 2004). Pol-γA, the catalytic subunit, is responsible for adding new nucleotides to the synthesized mtDNA and proofreading it. In contrast, the accessory subunits Pol-γB serve various functions in the Pol-γ complex, with one close and one distal in relation to the Pol-γA subunit. Pol-γB enhances the binding affinity of the Pol-γ complex and boosts the polymerization rate of Pol-γA (Lim et al., 1999).

The mitochondrial single strand binding protein (mtSSB) stabilizes the single strands of mtDNA during replication, preventing the single strands from winding back the opposing strand. Lastly, the mitochondrial RNA polymerase (POLRMT) forms the RNA-primer necessary for lagging strand syntheses (Falkenberg et al., 2007).

1.2 Mitochondrial disease and mitochondrial defect

Mitochondrial diseases represent a serious group of conditions, estimated to affect approximately 1 in 5000 adults. These diseases exhibit a high degree of heterogeneity in terms of their manifestation and timing. Mitochondrial diseases demonstrate substantial variance in both the severity of symptoms and the age of onset, even among cases with identical underlying genotype (Russell et al., 2020). Primarily caused by mutations in either the nuclear genome or the mitochondrial genome, mitochondrial diseases negatively impact mitochondrial respiration. These mutations can directly hamper the respiratory chain of OXPHOS or associated pathway. A related phenomenon, known as 'mtDNA depletion' occurs when there is a reduction in the number of mtDNA copies, leaving mitochondria with insufficient mtDNA to sustain their function. As a consequence of these conditions, symptoms of mitochondrial diseases often stem from insufficient energy production in the form of ATP to meet cellular demands. Tissues that are energy intensive such as neurons, skeletal muscle, and liver cells, are most often affected by these diseases. This effect is intensified due to the fact that mitochondrial diseases often severely impact post-mitotic tissues more than mitotic tissues, due to mitotic tissues having a better capability to select for healthy mitochondrion through mitotic division (Balaban et al., 2005).

Mitochondrial diseases are unique in that they can be caused by both mutations in nDNA and mtDNA. A substantial portion of mitochondrial proteins are encoded in the nucleus.

Consequently, while mtDNA is solely maternally inherited, mitochondrial disease that originates due to mutation in nDNA can also be inherited paternally. Another characteristic of these diseases is the way phenotypic expression depends on the number of mtDNA copies carrying a mutation. When all mtDNA copies share the same genotype, it is referred to as homoplasmy of the mitochondrial genome. The degree to which a mutation is present in the mitochondrial genome is termed heteroplasmy, represented as a percentage of the total mtDNA copies that carry the mutation. This leads to a unique mechanism where phenotypic expression depends on the degree of heteroplasmy, typically requiring over 60% heteroplasmy for phenotype manifestation (Rossignol et al., 2003). This phenomenon is known as the 'Threshold effect'. Notably, heteroplasmy levels can vary across different tissues and organs within the same individual (Chinnery, 1993). The threshold effect may be one of the reasons why there is a large amount of heterology when it comes to the onset and severity of mitochondrial diseases.

Symptoms of mitochondrial disease are incredibly diverse in their presentation, severity, and age of onset. They can include myopathies (muscle weakness or exercise intolerance) and encephalopathies (neuron weakness, potentially leading to sensory loss, ataxia, and seizures). A combination of neurological and muscle symptoms, known as encephalomyelopathy, can also occur. The severity of these conditions can range drastically, some might only experience difficulties with during intense exercise, while others may struggle to perform everyday tasks, such as lifting a cup, or struggle with basic functions such as swallowing due to weakness of the associated muscles. The age of onset is highly varied, with symptoms potentially appearing in newborn infants or manifesting as late as in a person's late sixties. Several factors may influence the age of onset such as mutations of nuclear or mitochondrial genome, the threshold factor of mtDNA mutation, and the phenomenon of mtDNA depletion.

1.3 Pol-γ and POLG related disorders

1.3.1 Pol-γ

POLG related disorders, or POLG diseases, are severe primary mitochondrial diseases caused by mutations in the *POLG* gene. This gene codes for the Pol-γA catalytic subunit of the Pol-γ holoenzyme, which is crucial for mtDNA replication and maintenance. POLG-related disorders are among the most common causes of primary mitochondrial diseases, and they are associated with a range of serious syndromes with varying onset ages. Symptoms can include

neurodegeneration, myopathy, and liver failure. The manifestation of POLG-related diseases stems from the diminished ability of Pol-γ to replicate and maintain the mitochondrial genome, leading to a decline in cellular energy due to impaired OXPHOS.

As previously mentioned, the Pol-γ mtDNA replication complex is a heterotrimer consisting of one catalytic Pol-γA, and two Pol-γB accessory subunits encoded by nuclear genes *POLG* and *POLG*2 located at chromosomal locus 15q25 and 17q24.1, respectively (Chan and Copeland, 2009). The catalytic subunit Pol-γA serves three distinct catalytic roles, firstly, it acts as a 5' – 3' DNA polymerase providing the ability for mtDNA replication, secondly, it functions as a 3' – 5' exonuclease providing proofreading mechanism, and finally, 5' deoxyribose phosphate lysate providing DNA ligase functionality. Pol-γA is comprised of three domains. The N'-terminal domain, the C'-terminal domain and a spacer linking region domain. The 5' – 3' DNA polymerase region is found in the C'-terminal region, the polymerase domain of Pol-γA shares structural similarities with other polymerase complexes and contains 3 subdomains termed the palm, the fingers, and the thumb. The N'-terminal domain consists of the 3'-5' exonuclease region, while the spacer region is the area of the protein separating these two regions. The active site of the 5' deoxyribose phosphate lysate has not yet been identified (Euro et al., 2011).

1.3.2 *POLG* mutations and POLG-related disorders

Mutations in the *POLG* gene have been linked to a wide array of diseases that exhibit significant differences in phenotype, severity, and age of onset. To date, over 200 individual mutations have been found to be associated with diseases linked to POLG mutations (Copeland, n.d.). These mutations have been linked to a broad spectrum of conditions, ranging from severe early onset acute syndromes such as AHS, Childhood Myocerebrohepatophy Spectrum Disorder (MCHS) and Leigh Syndrome. To late onset chronic progressive syndromes such as PEO, and Ataxia Neuropathy Spectrum (ANS). A comprehensive overview of the discovered mutations associated with syndromes caused by POLG mutations can be found in **Figure 1.4**.

Early onset disorders such as AHS and MCHS typically present from birth or within the first few years of life. They are characterized by severe neuropathy, including symptoms like ataxia, epilepsy, and sensory deprivation, migraines, and loss of combined with myopathy which manifests as muscle weakness, exercise intolerance, decreased muscle development, and weakness of muscles in the hearth (cardiomyopathy) or surrounding the lungs. These symptoms

are often accompanied by decreased liver function, which can escalate to total liver failure. The prognosis for early onset POLG-related diseases is generally poor, with outcomes often leading to death within a year from the onset of symptoms but can range from a few months to over a decade (Hikmat et al., 2017).

Late onset POLG-related syndromes, such as PEO, and ANS often exhibit similar but less severe symptoms as the early onset syndromes. These include neuropathic symptoms like ataxia, sensory deprivation, epilepsy, and parkinsonism, and myopathies such as exercise intolerance and muscle weakness. This weakness is often characteristically located in the muscles controlling the movement of the eye and eyelids, leading to drooping of the eyelids (ptosis). Late onset syndromes are characterized by less severe symptoms at onset, but with a steady progression. The onset of symptoms for these late onset syndromes can occur at virtually any point in adulthood, as early as from 18 years of age to as late as 40 years of age ("Progressive external ophthalmoplegia," n.d.).
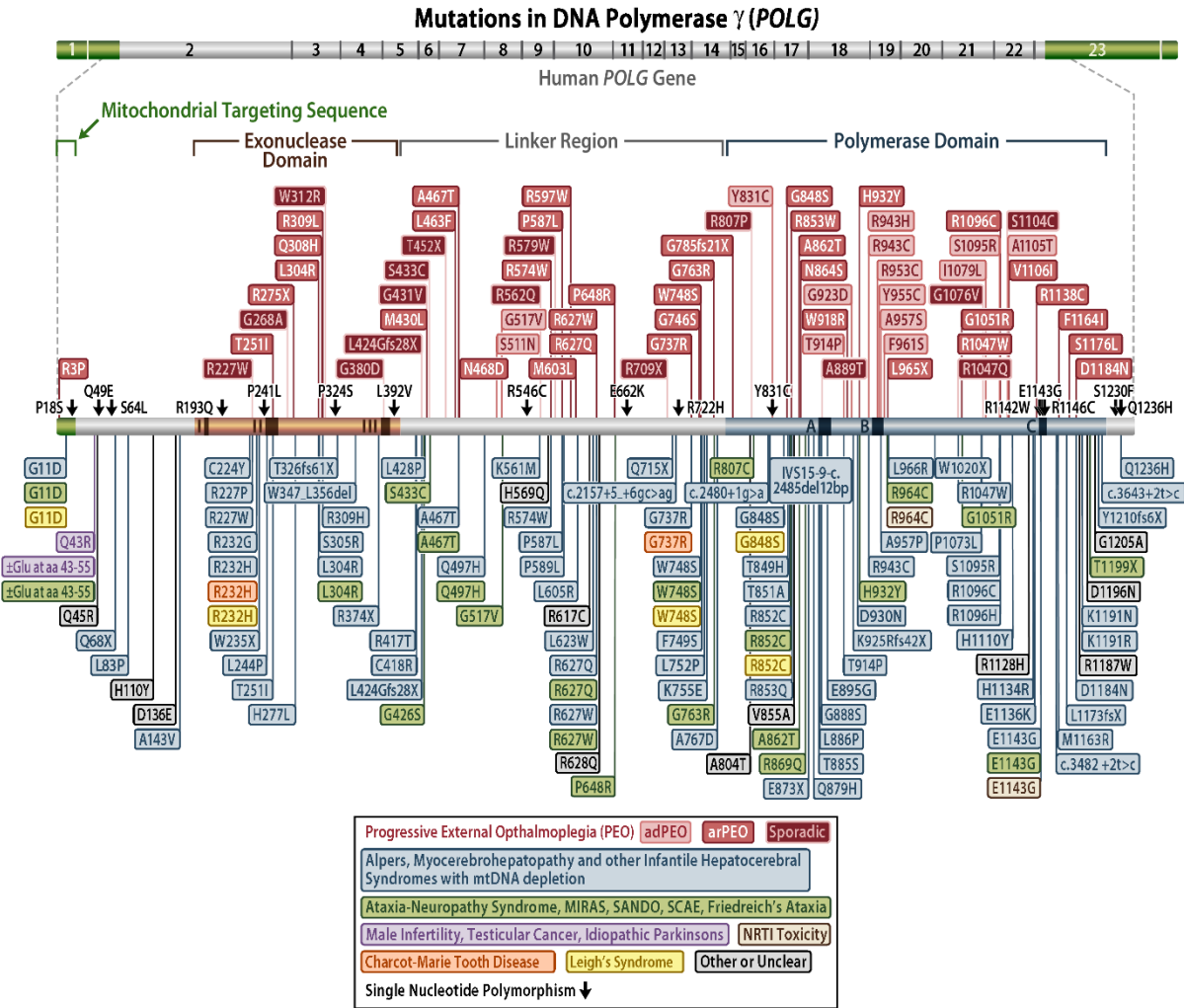
Figure 1.4 Overview of POLG-mutations and their associated clinical phenotypes by location on the POLG gene. Mutations shown in red are associated with PEO, (Pink – autosomal dominant PEO, Red – autosomal recessive PEO, Dark red – Sporadic PEO) Blue: AHS, MCHS, and other Infantile Hepatocerebral Syndromes. Green: ANS, MIRAS, SANDO, SCAE, and Friedreich's Ataxia. Purple: Male Infertility, Testicular Cancer, Idiopathic Parkinson's. White: NRTI Toxicity. Orange Charcot-Marie Tooth Disease. Yellow: Leigh's Syndrome. Gray: Other or Unclear syndromes. Black arrows show single nucleotide polymorphisms (Copeland, n.d.).

Mutations in the *POLG* gene primarily result in diminished mtDNA replication ability, leading to mtDNA depletion, and compromised maintenance and proofreading capabilities. This, in turn, results in the gradual accumulation of mtDNA mutations over time, including point mutations and deletions, due to Pol-γ dysfunction. This damage to mtDNA gradually erodes the ability of the mitochondria to sustain energy production through OXPHOS.

13

This dysfunction is believed to stem from an inability to properly form the ETC complexes located at the IMM. The failure of the ETC complexes leads to a reduction in the mitochondrial membrane potential, hampering the production of ATP by NADH dehydrogenase. Furthermore, ETC dysfunction is thought to cause an increase in the production of ROS. Accumulation of ROS is believed to inflict further damage to various mitochondrial components, including the mtDNA through oxidative stress.

Early onset syndromes are thought to be connected to an early depletion of mtDNA, while late-onset syndromes are thought to be triggered by the accumulation of numerous mtDNA mutations over time, leading to the progressive natures of these syndromes (Rahman and Copeland, 2019). Interestingly, however, it has been found that the same *POLG* gene genotype has been associated with several POLG-related disorders. For instance, the A467T mutation is associated with both AHS, ANS, and PEO as demonstrated in **Figure 1.4**. It remains unclear how the same genotype can cause such varying phenotypes.

Previous studies performed in our lab have shown that postmortem tissues of patients with POLG-related diseases display both a decrease in mtDNA copy numbers and an accumulation of mtDNA deletions (Tzoulis et al., 2013). This was observed to detrimentally impact chain function, primarily through C1 depletion. Notably, these patients were found to have significant neurodegeneration, particularly a reduction in dopaminergic neurons of the substantia nigra (Tzoulis et al., 2013). Interestingly, within this study, C1 was the sole mitochondrial complex exhibiting severe depletion. No changes were noted in complexes II, and III, and in complex IV. Consequently, it was inferred that C1 depletion could be the primary cause of OXPHOS dysfunction in POLG-related diseases.

1.4 Human stem cell model system

Conducting studies of neurodegenerative diseases comes with considerable challenges, primarily due to the limited availability of neuronal tissues for examination. The use of patient post-mortem tissues often only reflects the terminal of the disease and therefore give limited insights into the progression of the disease (Yu et al., 2014). Animal models, while useful, often fail to provide sufficiently reliable representations for studying neurodegenerative diseases. This is primarily due to significant interspecies variation, leading to the inability of animal models to accurately mimic the phenotypes seen in human patient (Dawson et al., 2018; Silva-Pinheiro et al., 2021).

Yeast models, while popular for mitochondrial functional studies, are not viable for researching specific disease functions. This is due to the factors of heteroplasmy, variance in the capability to maintain healthy mitochondria in mitotic versus post-mitotic tissues and nuclear to mitochondrial interactions, as these are not viable to study the tissue specific functions of mitochondrial diseases (Lasserre et al., 2015). These limitations underscore the need for the development of alternate modeling systems to further our understanding of neurodegenerative diseases.

1.4.1 Human iPSCs

iPSCs, derived from humans, have recently emerged as a promising advancement in stem cell technology for exploring neurodegenerative diseases in human models. iPSCs are obtained by reprogramming somatic tissues derived from humans to achieve a state of pluripotency. Shinya Yamanaka, a researcher at the university of Kyoto, pioneered the concept of iPSCs in 2006, by successfully inducing pluripotency in adult somatic cells of mice with the induction of four transcription factors (Takahashi and Yamanaka, 2006). Yamanaka's study showed that iPSCs exhibit similar morphology and growth properties embryonic stem cells (ESCs), along with comparable differentiation capacity, enabling them to differentiate into cells of any of the three germ layers (Takahashi et al., 2007; Takahashi and Yamanaka, 2006). Subsequently, Yamanaka and his team demonstrated that this protocol could be used to produce human-derived iPSCs from adult human somatic tissues (Takahashi et al., 2007). The four transcription factors used in this process, namely Oct4, Sox2, Klf4 and cMyc, have been named the Yamanaka factors and are commonly employed in reprogramming of somatic cells to iPSCs. While much of stem cell research in the past revolved around ESCs, this field faced significant controversy due to ethical considerations surrounding the use of human embryos. The harvesting of the blastocytes from a fertilized human embryo, necessary for obtaining ESCs, has led to a large amount of controversy, especially from within conservative and religious communities. They debate when an embryo should be considered a human life. iPSCs circumvent these ethical concerns since they can be derived from adult tissues through minimally invasive methods, eliminating the need for human embryos. Additionally, iPSCs possess the same ability to proliferate and differentiation capabilities as ESCs across the three germ layers (Halevy and Urbach, 2014).

The original method developed for delivering the transcription factors utilized a retroviral delivery system. However, this approach has limitation: the delivered transcription factors would

integrate into the host cell's DNA, potentially interfering with some downstream differentiation pathways (Kunitomi et al., 2022). A later development offered a solution to this issue. The Sendai-virus delivery system delivers non-integrating transcription factors that are expressed in the cytoplasm, leading the eventually cessation of their expression and allowing for greater specificity in downstream differentiation. (Kunitomi et al., 2022).

1.4.2 Applications of iPSCs

The main advantages iPSCs have are 1.) That they are readily available. Since iPSCs are obtained from adult somatic cells they can easily be obtained in a non-invasive manner, additionally once iPSCs have been generated they can be continuously expanded almost indefinitely. 2.) iPSCs can be generated from patient tissues, causing them to natively carry patient DNA. This makes iPSCs uniquely useful in the study of genetic diseases, with no need to perform gene editing. This also gives an advantage in the modeling of complex multisystem disorders, such as those that are caused by more than one gene mutation (Halevy and Urbach, 2014). 3.) They have the ability to be differentiated into virtually any cell type of the three germ layers. This feature combined with the ability to be derived from patient somatic cells, make them uniquely useful in several aspects. One potential use is in disease modeling, being derived from patient cells means that the iPSCs carry the complete genotype of the patient and opens up the opportunity to investigate patient specific mechanisms, and treatments. Additionally, the differentiation capacity of iPSCs make them uniquely useful in studying disease mechanisms in tissues that may be hard to otherwise obtain such as brain, heart, or liver tissues without the need for intrusive procedures. The expansion capability of the iPSCs also lends them the opportunity to be useful in large scale drug screening studies. Another promising application for iPSCs is within the field of regenerative medicine. Tissues for use in grafting for injuries can be generated from patient somatic cells because the generated cells carry the patient's genes the risk of autoimmune rejection is minimal compared to a transplant. Additionally, there is potential to transplant tissues generated from gene corrected patient iPSCs to combat genetic diseases.

1.4.3 iPSCs studies in POLG disorders

The unique attributes of iPSCs render them an invaluable tool for investigation of POLG-related diseases. These conditions are multifaceted, resulting from both genetic and mitochondrial influences, and often present in post-mitotic tissues that are difficult to access. Given these

complexities, iPSCs serve as an excellent model for studying POLG-related diseases. Previous research conducted in our laboratory has successfully produced neural tissues from iPSCs derived from somatic cells of POLG patients. The iPSC-derived neuronal stem cells faithfully recreated the patient phenotypes observed in post-mortem tissues, including mtDNA depletion, C1 deficiency, compromised membrane potential, and ETC malfunction. Moreover, these POLG-iPSC derived neuronal cultures displayed elevated levels of ROS, an outcome of respiratory chain dysfunction, mirroring the conditions found in POLG-related diseases (Liang et al., 2020).

1.5 3D organoid modeling system

Recently established as a novel three-dimensional modeling system, Organoids are derived from pluripotent stem cells (PSCs). These stem cell clusters have the potential to emulate the development of various tissues and tissues and organs in vitro when provided with appropriate differentiation signals. Characterized by their sophisticated multicellular configurations, organoids encapsulate comparable cell types and autonomously forge structural patterns that mirror those found in analogous tissues or organs within living organisms (Kim et al., 2020).

Organoids serve as a valuable research tool as they offer the opportunity to probe mechanisms within a complex multicellular environment that closely resembles in vivo conditions. In addition, their derivation from human cells allows them to bypass limitations associated with animal models, better recapitulating species-specific mechanisms. Stemming from PSCs, organoids possess the capacity to be genetically manipulated or tailored to specific disease conditions, thus broadening their application in biomedical research. This feature allows for a more nuanced understanding of human developmental biology, disease modeling, and the possibility of personalized medicine.

Another significant aspect of organoid technology is its capacity for extended self-organization and self-renewal. Organoids can continue to develop, mimic complex tissue structures and functions over time, and can be maintained for prolonged periods, which is particularly beneficial for long-term studies. Moreover, organoids offer a promising platform for drug discovery and toxicity testing. They provide a more physiologically relevant model compared to traditional two-dimensional cell culture systems and can help predict drug responses more accurately. This can potentially expedite the process of drug development and increase its safety and efficacy. However, it is important to note that while organoids provide a remarkably accurate model of

human organ development and function, they still lack some critical elements, such as the complete representation of all cell types in a particular organ and the interaction with the body's immune system. Ongoing research and technological advancements are striving to overcome these limitations and enhance the potential applications of organoids in biomedical research.

In conclusion, the potential of organoids as a robust tool in biomedicine is vast, ranging from elucidating complex biological processes, disease modeling, drug testing, and even potential use in regenerative medicine. As we continue to refine and improve this technology, the full scope of their application is only beginning to be realized.

1.5.1 Generation of brain organoids

Brain organoids mimic certain aspects of the human brain's architecture and function, providing an unprecedented means to study human brain development and various neurological disorders (Lancaster et al., 2013). Many different organoid models have been developed to date, modeling different organs and tissues. These organoids can be designed to resemble different regions of the human brain, such as the cerebral cortex, midbrain, hippocampus, hypothalamus, and others. This allows researchers to model brain development and disease in the specific areas of the brain that are most relevant (Lee and Sun, 2022). Among these several models for brain organoids modeling various regions of the brain have been developed. Brain organoids replicate the cellular composition as found in the developing embryonic brain, including neural progenitors, diverse neuron subtypes, oligodendrocytes, and astrocytes.

The generation of brain organoids begins with the cultivation of human PSCs. These cells are first differentiated into neuroectoderm, which are early-stage cells that will eventually develop into nervous system tissue. The neuroectoderm cells are then patterned into brain region-specific neural progenitor cells using a combination of small molecules and growth factors. These neural progenitor cells are then coaxed to form spheroids, which continue to grow and differentiate into mature neurons and glial cells, organizing themselves into structures reminiscent of the human brain (Quadrato et al., 2017). The resulting brain organoids offer a unique platform to study human neural development and disease, providing insights that are difficult or impossible to obtain through traditional 2D cell cultures or animal models. They hold promise for improving our understanding of complex neurological conditions such as autism, schizophrenia, and neurodegenerative diseases like Alzheimer's and Parkinson's (Qian et al., 2019).

1.5.2 Applications of brain organoids

Brain organoids are a revolutionary tool in the field of neuroscience. They are 3D cell culture models derived from human iPSCs that organically form structures characteristic of the human brain. These miniature versions of the brain open new frontiers in neuroscience, allowing for advances in various applications:

Disease Modelling

Brain organoids provide a unique platform to model neurological diseases in the lab. By using iPSCs derived from patients, researchers can create organoids that carry the same genetic makeup as the patient, allowing them to study the cellular and molecular mechanisms of diseases such as Alzheimer's, Parkinson's, autism, and schizophrenia. These "disease-in-a-dish" models can also be used to identify novel therapeutic targets (Eichmüller and Knoblich, 2022; Lancaster et al., 2013).

Drug Testing and Personalized Medicine

Traditional drug testing often relies on animal models and 2D cell cultures that may not accurately reflect human biology. Brain organoids provide a more accurate, human-relevant model for testing new drugs and therapies. In personalized medicine, patient-derived organoids can be used to predict an individual's response to a drug, potentially allowing for customized treatments (Gonzalez et al., 2018; Lee and Sun, 2022).

Developmental Biology

Brain organoids offer insights into human brain development. They can be used to study the processes of neuronal differentiation, migration, and maturation. This is particularly relevant for studying early brain development, a stage that is inaccessible in living humans (Lee and Sun, 2022).

Regenerative Medicine

In the future, brain organoids could potentially be used for tissue replacement therapy in patients with neurodegenerative disorders or brain damage. However, this application is currently in its early stages and faces many challenges, including the integration of organoid-derived neurons into existing brain circuits.

Despite the exciting applications of brain organoids, it is important to acknowledge the ethical and technical challenges they pose. For instance, the ethical implications of creating brain tissue in the lab, the limitations in organoid size due to the lack of a vascular system, and the variability between individual organoids. As technology and methods improve, brain organoids are set to become increasingly valuable tools in neuroscience and medicine (Kim et al., 2020; Mansour et al., 2018).

1.6 Nicotinamide riboside (NR)

NAD+ is a critical molecule that propels OXPHOS by acting as the electron donor that is reduced to NADH by C1, underscoring its crucial role in proper mitochondrial function. A deficiency in NAD+ has been associated with neurodegenerative conditions such as Alzheimer's and Parkinson's disease, as well as a potential role in the aging process (Fang et al., 2017). There are three primary pathways that maintain NAD+ levels within cells: the de novo synthesis pathway, the Priess-Handler pathway, and the salvage pathway. The presence of multiple routes to produce and maintain NAD+ emphasizes its vital importance to cellular health. These pathways include: 1). De Novo Synthesis: This pathway commences with tryptophan and involves a multi-step process that ultimately results in NAD+. However, this process is generally considered inefficient and is not the primary source of NAD+ for most tissues (Nikiforov et al., 2011). 2). Priess-Handler pathway: This pathway generates NAD+ from nicotinic acid via a series of enzymatic reactions. Although this pathway can contribute significantly to NAD+ levels in certain tissues, its overall contribution to cellular NAD+ levels is often lesser than that of the salvage pathway (Preiss and Handler, 1958). 3). Salvage Pathway: This pathway is considered the primary source of cellular NAD+. It involves recycling the NAD+ breakdown product, nicotinamide (NAM), back to NAD+ via the enzyme nicotinamide phosphoribosyl transferase (NAMPT). NR, being a precursor to NAD+, can be directly converted to NAD+ via this pathway, bypassing the need for NAMPT, which is often a rate-limiting step in NAD+ synthesis (Bieganowski and Brenner, 2004). These pathways, along with NAD+ supplementation strategies such as NR, are subjects of active research due to their potential therapeutic roles in aging and neurodegenerative diseases.

1.6.1 NR and mitochondrial dysfunction

Mitochondrial dysfunction is characterized by a decrease in mitochondrial biogenesis, reduced efficiency in the electron transport chain, and an increase in the production of ROS. These events

lead to a decline in ATP generation, impairing cellular energy metabolism.NR supplementation has been found to improve mitochondrial function through various mechanisms. One of these is the enhancement of NAD+ levels, a coenzyme central to mitochondrial metabolism. NR, as an NAD+ precursor, can boost NAD+ concentrations, which, in turn, can stimulate sirtuins, a family of metabolic regulatory proteins that have been linked to lifespan extension and improved mitochondrial function (Verdin, 2015). Further, studies in mouse models have shown that NR supplementation can reverse mitochondrial myopathy by normalizing NAD+ levels, inducing mitochondrial biogenesis, and improving mitochondrial function (Khan et al., 2014).

1.6.2 NR and neurodegeneration

Neurodegenerative diseases, such as Alzheimer's and Parkinson's, often involve the progressive loss of structure or function of neurons, including their death. Mitochondrial dysfunction and oxidative stress are common characteristics of these diseases. NR has shown promise in preclinical studies as a potential neuroprotective agent. Studies in mouse models of Alzheimer's disease have found that NR supplementation can increase brain NAD+ levels, reduce amyloid beta toxicity, enhance synaptic plasticity, and improve cognitive function (Hou et al., 2018). Similarly, in models of Parkinson's disease, NR has been shown to protect against neurodegeneration by preserving neuronal NAD+ levels, reducing oxidative stress, and improving mitochondrial function (Schöndorf et al., 2018).

While studies on NR's effects on mitochondrial dysfunction and neurodegeneration are encouraging, most research to date has been conducted in animal models. Therefore, clinical trials in humans are necessary to further evaluate NR's safety, efficacy, and therapeutic potential in these contexts.

2. Aims

Our goal is **to use 3D COs derived from patient-specific iPSCs as models of POLG-associated diseases to study disease mechanisms and explore new therapeutic approaches.**

Specific aims:

1). Differentiate patient-specific iPSCs into 3D COs: The second aim is to induce the differentiation of patient-specific iPSCs from individuals with POLG-associated diseases into 3D COs. By mimicking the developmental processes that occur in the developing brain, these organoids will recapitulate the complex cellular composition and architecture of cortical tissue. The differentiation protocols will be optimized to ensure the generation of mature cortical neurons and glial cells within the organoids.

2). Characterize disease mechanisms in POLG-associated diseases using 3D COs: The second aim is to investigate disease mechanisms associated with POLG mutations using the patient-derived 3D COs. Various analyses will be performed, including assessment of mitochondrial features, DNA maintenance defects, neuronal loss, and dysfunction of specific neuronal subtypes. The organoids will be compared to healthy control organoids to identify disease-specific alterations.

3). Validate therapeutic candidates and explore mechanisms of action: The third aim is to validate the identified therapeutic candidates using the POLG organoid model. The effects of the candidate compounds on mitochondrial function, DNA maintenance, and neuronal survival will be further characterized.

By addressing these specific aims, the project aims to enhance our understanding of POLG-associated diseases, identify potential therapeutic targets, and facilitate the development of novel treatments. The utilization of patient-specific 3D COs will provide a valuable platform for studying disease mechanisms and screening therapeutic candidates in a more relevant and complex human cellular context.

3. Materials & methods

Ethics Approval

The project was approved by the Western Norway Committee for Ethics in Health Research (REK nr. 2012/919). Tissues were acquired with written informed consent from the patient, and the experiments conformed to the principles set out in the WMA Declaration of Helsinki and the Department of Health and Human Services Belmont Report.

3.1 Source of iPSCs

Skin fibroblasts were obtained from a patient carrying compound heterozygous *POLG* mutations, p.A467T (c.1399G>A) and p.P589L (c.1766C>T), fibroblasts were collected through a punch biopsy procedure. As for the control group, a clone of CRL2097 fibroblasts (ATCC, CRL-2097™) was used. Pluripotency was induced in the fibroblasts through transfection of the coding regions of the Yamanaka factors Sox2, Oct4, KLF4, and c-Myc, through a Sendai-virus viral delivery system. Through this process, two clones of the patient specific iPSCs were generated. These clones were referred to as Patient 1 and Patient 2 in the experiments described in this research paper.

3.2 Cell Cultures

All cell culture work was carried out under sterile conditions in a Class 2 Mars Fume hood Cabinet (Labogene.). To maintain a clean workspace, the work environment and equipment were disinfected with 75% ethanol before and after each procedure was performed. All cell lines were maintained at a temperature of 37°C in a humidified CO_2 incubator with 5% CO_2 (Thermo Fisher Scientific, Cat. No. 51033557).

For the iPSC cultures, E8 Complete medium was utilized. The E8 complete medium was prepared by combining Essential 8 Supplement 50X (Thermo Fisher Scientific, Cat. No. A15171-01) in a 1:50 ratio with Essential 8 Basal Medium (Thermo Fisher Scientific, Cat. No. A151669-01). To ensure the absence of mycoplasma contamination, regular checks were performed on all cells using a mycoplasma detection kit (Lonza, Cat. No. LT07-218). This step was taken to maintain the integrity and quality of the cell cultures.

3.2.1 Preparation of Geltrex-coated well plates

To facilitate the growth of iPSCs, Geltrex-coated well plates were used for the culturing of iPSCs. The gel coating process involved preparing a Geltrex coating matrix by diluting Geltrex solution (Thermo Fisher Scientific, Cat. No. A14132-01) at a ratio of 1:100 in Advanced DMEM (Thermo Fisher Scientific, Cat. No. 12634-010). The Geltrex matrix was kept cold on ice before coating to prevent premature gelling. The Geltrex coating matrix provides a synthetic basement membrane that supports cell adhesion and growth. Each well of a 6-well plate (Thermo Fisher Scientific, Cat. No. 140675) was coated with 1 ml of cold Geltrex coating matrix. After ensuring that the Geltrex matrix evenly covered the entire surface of the wells, the covered well plates were incubated for 60 min at 37°C. After incubation, the remaining medium was aspirated, and the Geltrex-coated plates were prepared for sowing of the iPSCs.

3.2.2 Thawing of iPSCs

All iPSC lines were stored in liquid nitrogen storage prior to culturing. Thawing of frozen iPSCs was performed as follows. ROCK-inhibitor supplemented medium was prepared by supplementing E8 complete medium with 10 μM of Y-27632 dihydrochloride (ROCK-inhibitor) (Tocris Bioscience, Cat. No. 1254). The medium used in the thawing process was supplemented with ROCK-inhibitor to increase the growth of iPSCs following cryopreservation (Claassen et al., 2009; Li et al., 2008). To initiate the thawing process, cryovials were taken out and allowed to thaw at room temperature until only a small shard of ice remained. To resuspend the cells, 1ml of ROCK supplemented medium prewarmed to room temperature (RT), was added dropwise to the cryovial to resuspend the cells. The medium was added gently to avoid damaging the cells due to osmotic shock. The cell suspension was then transferred to a pre-prepared Geltrex-coated well containing 3ml of medium supplemented with ROCK inhibitor and the well plates were gently stirred to ensure even cell distribution, before being placed in the incubator. After 24 hours, the ROCK supplemented medium was replaced with 3 ml of un-supplemented E8 complete medium, promoting further growth and survival of the iPSCs.

3.2.3 Maintenance and splitting of iPSCs.

The iPSC cultures were maintained in incubator at 37°C with 5% CO_2. The cells were fed daily with 3ml of E8 complete medium. Regular visual assessments under a Leica DM IL LED

inverted light microscope (Leica Microsystems) were conducted to evaluate the purity and confluence of the iPSC cultures. Splitting was performed When the iPSCs reached approximately 70%-80% confluency. Differentiated colonies were carefully removed by scraping with a pipette tip or a cell scraper. while undifferentiated iPSCs were identified by their tightly packed colonies with well-defined edges, following Thermo Fishers protocol on Culturing Pluripotent Stem Cells in E8 medium ("Culturing Pluripotent Stem Cells (PSCs) in Essential 8^{TM} Medium - NO," 2016)

The splitting process involved several steps. First, the medium in the wells was removed, and the cells were washed twice with 3ml of DPBS-/-. After the washes, the DPBS-/- was aspirated, and 1ml of 0.5 mM EDTA (Invitrogen, Cat. No. 15575020) was added to each well to detach the cells. EDTA effectively breaks down the extracellular matrix without disrupting the cell membrane. The iPSCs in EDTA were incubated for 3-5 minutes, and the breakdown of the extracellular matrix was evaluated by observing it under a light microscope. Once the matrix was sufficiently deteriorated, the EDTA was aspirated. To detach the iPSCs from the wells, 4ml of E8 complete medium was gently sprayed over the cells, and a 2ml cell suspension was transferred to fresh Geltrex-coated wells. The cells were then returned to their regular maintenance conditions for further cultivation.

3.2.4 Cryopreservation of iPSCs

To prepare the cryopreservation medium, a mixture of 10% DMSO and 10µM of ROCK-inhibitor was added to E8 complete medium. Prior to cryopreservation, the iPSCs were washed with DPBS-/- and then treated with 1ml of EDTA to detach the cells. Subsequently, 1ml of cryopreservation medium was gently sprayed onto the cells to facilitate detachment, and the cell suspension was transferred to a 2ml cryovial. The cryovial was placed in a Coolcell freezing container (Corning) and stored at in -20°C for 24 hours. The purpose of the freezing container was to enable gradual cooling of the cryovial, preventing damage caused by rapid temperature changes. After the initial 24-hour period at -20°C, the freezing container, along with the cryovials, was transferred to -80°C and stored for an additional 24 hours. Finally, the cryovial was moved to liquid nitrogen storage for long-term preservation.

3.3 Differentiation of COs from iPSCs.

The differentiation of iPSCs into COs and maintenance of COs and the subsequent maintenance of COs were carried out following established protocols as described in previous work (Xiang et al., 2018). The specific details of these protocols can be found in the referenced study.

3.3.1 Formation of Embryoid Bodies (EBs) and Neural Induction.

The EBs were formed from iPSCs by the following method. After one week of seeding iPSCs in Geltrex-coated plates or reaching 80% confluency, the cells were visually inspected under a light microscope, and any differentiated colonies were carefully removed by scraping with a pipette tip or cell scraper. The old medium was aspirated, and the cells were washed with 1ml of DMEM/F12 per well to eliminate debris and dead cells. Detachment of iPSCs was achieved by adding 1ml of Accutase (Life Technologies, Cat. No. A11105-01) and incubating at 37°C for 10 minutes. Accutase was used instead of EDTA as it facilitated dissociation into single cells while detaching them from the well surface. The detachment and dissociation were confirmed by examination under light microscope. The remaining cells were gently sprayed with a 1ml pipette to detach them, and the detached cells were transferred to a 15 ml tube containing 5ml of pre-prepared DMEM/F12. The tubes were centrifuged for 3 minutes at 1100 RPM at room temperature, and the supernatant was aspirated. The cell pellet was resuspended in 1ml of Neural Induction Medium (NIM) following the composition specified in **Table 3.1**. Cell counting was performed using a Countess II automatic cell counter by mixing 10 µl of the cell suspension with 10 µl of 0.4% Trypan blue stain and loading the mixture into each chamber of a Countess cell counting chamber slide. The cell suspension was diluted in NIM to a concentration of 60,000 live cells per ml. The diluted cell suspension was supplemented with a final concentration of 50 µM Y-27632 Rock Inhibitor and 5% (v/v) heat-inactivated Fetal Bovine Serum (FBS). Subsequently, 150 µl of the cell suspension were seeded in each well of an ultra-low attachment 96-well plate to achieve a seeding density of 9000 live cells per well. The outer wells of the plate were filled with DPBS-/- to compensate for evaporation. The day of iPSC seeding into the 96-well plate was designated as day 0 of the differentiation protocol.

Table 3.1. Composition of Neural Induction Medium used for neural induction of EBs.

Neural Induction Medium. (NIM)			
Reagent Name	Supplier	Catalogue number.	Concentration.
DMEM/F12 Hepes	Thermo Fisher Scientific.	11330-032	
Knockout Serum Replacement.			15 % (v/v)
MEM-Non-Essential Amino Acids (100X)	Thermo Fisher Scientific.	11140-050	1 % (v/v)
GlutaMAX supplement (100X)	Thermo Fisher Scientific.	35050-061	1 % (v/v)
Stemolecule™ LDN-193189	Reprocell.	04-0074	100 nM
SB431542 (TGF-β RI Kinase Inhibitor VI)	Sigma-Aldrich.	616461	10 μM
XAV939	Sigma-Aldrich.	X3004	2 μM
Beta-mercaptoethanol	Sigma-Aldrich.	M3148	100 μM

3.3.2 Generation of COs

On day 10 of the differentiation process, the differentiated EBs were transferred to spinning culture to differentiate, where they would continue to differentiate without the addition of any regionalization factors. Under these conditions, the EBs would differentiate to organoids containing growth patterns resembling those of the cortical regions of the embryonic stage brain (Lancaster et al., 2013).

Before being transferred to spinning culture, EBs were embedded in Matrigel droplets following a modified version of the Stemcell™ Technologies protocol for Neural Organoid Culture ("Protocol for Neural Organoid Culture," 2020). The Matrigel Matrix (Corning, Cat. No. 356234) was thawed while kept cold on ice, and an Organoid embedding sheet (Stemcell™ Technologies Cat. No. 8579) was prepared in a 100ml petri dish. The EBs were transferred from the culture in a 96-well plate onto the embedding sheet using a 1ml pipette with a cut tip, with one EB placed per well. Excess medium was removed, and 15μl of ice-cold Matrigel Matrix was added to each well to encase the EBs. The EBs were gently shifted using a 20μl pipette tip to center them within the Matrigel droplets. The embedding sheet with the EBs was then incubated for 30 minutes at 37°C to allow the Matrigel droplets to solidify around the EBs. Subsequently, 5-8 embedded EBs were

gently washed off the embedding sheet by spraying them with Neural Differentiation Medium – Vitamin A (NDM-A) and dropped into the wells of an Ultralow attachment 6-well plate (Corning®, Cat. No. 3471) containing 3ml of NDM-A as specified in **Table 3.2**. The plates were incubated on an orbital rotary shaker at 80 RPM, with the medium being changed every 2 days until and including day 16 of the differentiation process.

Table 3.2. Composition of Neural Differentiation Medium – Vitamin A used for differentiation of EBs to COs.

Neural Differentiation Medium – Vitamin A (NDM-A)			
Reagent Name	**Supplier**	**Catalogue number**	**Concentration**
DMEM/F12 Hepes	Thermo Fisher Scientific	11330-032	
Neurobasal® Medium (1X)	Thermo Fisher Scientific	21103-049	
Insulin, Human recombinant (yeast)	Sigma-Aldrich	11376497001	0.025% (v/v)
MEM-Non-Essential Amino Acids. (100X)	Thermo Fisher Scientific	11140-050	0.5% (v/v)
Glutamax supplement (100X)	Thermo Fisher Scientific	35050-061	1.0% (v/v)
Penicilin/Streptomycin			1.0% (v/v)
N2 Supplement (100X)	Thermo Fisher Scientific	17502-048	0.5% (v/v)
B27 Supplement – Vitamin A	Thermo Fisher Scientific	12587-010	1.0% (v/v)
Beta-Mercaptoethanol	Sigma-Aldrich	M3148	50 µM

3.3.3 Maturation of COs

On day 18 of differentiation, the medium was replaced with 5 ml Neural Differentiation Medium (NDM), to allow the differentiated organoid for long-term maintenance and maturation. The composition of NDM is listed in **Table 3.3.** Medium was changed every 3 days. When changing the medium, 1ml of old medium was left in the wells, and 4 ml of fresh medium was added in order to avoid any damage to the COs. The COs were further maintained in incubator at 37°C on an orbital rotary shaker at 80 RPM for up to 3-4 months.

Table 3.3. Composition of NDM used for long term maintenance of COs.

Neural Differentiation Medium. (NDM)			
Reagent Name	Supplier	Catalogue number	Concentration
DMEM/F12 Hepes	Thermo Fisher Scientific	11330-032	
Neurobasal® Medium (1X).	Thermo Fisher Scientific	21103-049	
Insulin, Human recombinant (yeast)	Sigma-Aldrich	11376497001	0.025% (v/v)
MEM-Non-Essential Amino Acids (100X)	Thermo Fisher Scientific	11140-050	0.5% (v/v)
Glutamax supplement (100X)	Thermo Fisher Scientific	35050-061	1.0% (v/v)
Penicilin/Streptomycin			1.0% (v/v)
N2 Supplement (100X)	Thermo Fisher Scientific	17502-048	0.5% (v/v)
B27 Supplement	Thermo Fisher Scientific	12587-010	1.0% (v/v)
Beta-Mercaptoethanol	Sigma-Aldrich	M3148	50 µM
Brain Derived Neurotrophic Factor (BDNF)			20 ng/ml
Ascorbic Acid	Sigma-Aldrich	92902-500G	

3.4 Compound treatment with NR

To test the effects of NR on COs, organoid cultures were supplemented with NR. The NR used in this study was kindly provided by Evandro Fei Fang at University of Oslo. NR supplementation was carried out by adding 1.0 mM NR directly into organoid cultures at a concentration of 1 µl per ml of NDM. NR supplementation was carried out from day 20 of differentiation and treated until 3–4-month-old.

3.5 Immunofluorescent staining of COs

3.5.1 Staining protocol

COs were moved from culture over to a Superfrost™ adhesion slide (Thermo Fisher Scientific, Cat. No. J1800AMNZ) using a 1 ml pipette with a cut tip to give a wide opening, ensuring transfer of whole organoids without disturbance. Excess medium was aspirated from the slide, and the slide was left to dry until completely dehydrated. The COs were then fixed by using 4%

(v/v) EM grade PFA in 1X PBS for 30 minutes at RT. PFA solution was then aspirated and washed twice with 1X PBS. the blocking buffer was prepared by adding 10% (v/v) Normal goat serum (Sigma Aldritch, Cat. No. G9023) and 0.1% (v/v) Triton X100 (Sigma-Aldrich, Cat. No. 9036-19-5) in 1X PBS and were then added to the slides at RT for 2 hours to prevent non-specific binding of antibodies and to permeabilize the cells. Then, the blocking buffer was removed, and a circle was drawn with a Liquid Blocker pen (Agar Scientific, Cat. No. AGL4197S.) to hold the blocking buffer within the samples. Primary antibodies solution was prepared in blocking buffer according to the designed concentrations. Detailed information of the primary antibodies is listed in **Table 3.4.**

Table 3.4. Primary antibodies and the concentrations that they were used in.

Primary Antibodies. Name	Supplier	Species	Catalogue Number	Concentration
Anti-NDUFB10	Abcam	Rabbit	Ab196019	1:300
MAP2 Antibody (Conjugated PE)	Santacruz Biotechnology	Mouse	Sc-74421	1:200
Anti-GFAP Antibody	Abcam	Chicken	Ab4674	1:200
Anti-mtTFA Antibody (Conjugated Alexa flour® 488)	Abcam	Mouse	Ab198308	1:200
VDAC1/Porin Antibody (Conjugated Alexa flour® 647)	Santacruz Biotechnology	Mouse	Sc-390996	1:200
Anti-SOX2 Antibody	Abcam	Rabbit	Ab97959	1:100
Anti-MAP2 Antibody	Abcam	Chicken	Ab5392	1:100
Recombinant Anti-GFAP antibody	Abcam	Mouse	Ab279289	1:200

Blocking buffer containing primary antibodies were added to the samples in enough volume to completely cover the samples. Primary antibody staining samples were incubated in the dark for 48 hours at 4°C. The primary antibodies were then aspirated, and the samples were washed with 1X PBS by repeated frequent rinsing for 2 hours. Secondary antibodies prepared in blocking

buffer solution and Hoechst 33324 nuclear counterstain (1:5000, Thermo Fisher Scientific, Cat. No. 62249.) were added and incubated for 48 hours in the dark at 4°C. Secondary antibodies and the concentrations used are given in **Table 3.5**.

Table 3.5. Secondary antibodies and the concentrations they were used in.

Secondary Antibodies.			
Name	**Supplier**	**Catalogue Number**	**Concentration**
Goat anti-Rabbit IgG (H+L), Alexa Fluor™ 488	Thermo Fisher Scientific	A11008	1:800
Goat anti-Chicken IgY (H+L), Alexa Fluor™ 647	Thermo Fisher Scientific	A21449	1:800
Goat anti-Rabbit IgG (H+L), Alexa Fluor™ 594	Thermo Fisher Scientific	A11012	1:800
Goat anti-Mouse IgG2b, Alexa Fluor™ 488	Thermo Fisher Scientific	A21141	1:800
Goat anti-Chicken IgY (H+L) Secondary Antibody, Alexa Fluor™ 594	Thermo Fisher Scientific	A11042	1:800
Goat anti-Mouse IgG (H+L) Highly Cross-Adsorbed Secondary Antibody, Alexa Fluor™ 647	Thermo Fisher Scientific	A21236	1:800

After the incubation of the secondary antibodies the remaining buffer was aspirated, and the samples were washed with 1x PBS by quick repetitive rinsing and then kept with PBS containing 0.01% (v/v) of sodium azide incubate overnight at 4°C in the dark to prevent contamination. Next day, the solution was removed, and the samples were mounted by adding 20µl of Flourmount-G mounting medium (SouthernBiotech, Cat. No. 0100-20.) onto each sample and covering them with a 1.5 mm coverslip. The mounting medium was left to polymerize at RT in dark for 24 hours and then were stored at -20°C until imaging.

3.5.2 Imaging in Sp8 & fluorescence intensity analysis.

Images for fluorescent intensity analysis were taken with The Leica TCS SP8 STED 3X (Leica microsystems). Images were captured by locating areas with high amount of well-defined brightly DAPI stained nuclei. Z-level was adjusted to capture the outermost layer where staining efficiency seemed to be optimal. At least 5 images of distinct regions were captured per organoid.

Fluorescent intensity analysis was performed using ImageJ. First, single channel images were imported into ImageJ. The images were then converted to 8-bit, by selecting "Image > Type > 8-bit" this converts the image to grayscale and is necessary for using the 'Threshold' feature in the next step. Next the threshold was set by selecting "Image > Adjust > Threshold". The threshold feature allows to select the required fluorescence intensity of a pixel to be taken into account for the measuring feature. The thresholds were individually selected for each channel based on images taken from control CO, threshold setting was chosen to maximize positive signal while minimizing amount of signal from background fluorescence. The fluorescent intensity was then measured using the 'Measure' function by selecting "Analyze > Measure". This process was repeated on a per image basis to acquire the fluorescent values for each image. A macro was created to optimize this process and reduce the risk of human error. The macro is a set of code created within the ImageJ program that allowed the process to be automatically performed on an image with the press of a button, so that the process need not be manually performed on every image. The values used for the fluorescent intensity analysis were obtained from the 'Integrated density' (IntDen) value obtained from the measure function.

3.6 Flow cytometry.

Before performing flow cytometry, it was necessary to dissociate COs into single cells. Dissociation of COs was performed by the following method. To begin, COs were transferred from culture to a 15ml Eppendorf tube containing 10ml DPBS-/- and left to sediment for 5 minutes. DPBS-/- was then aspirated and 2ml of prewarmed accutase was added per tube to facilitate dissociation. Tubes were incubated in water bath for 10 minutes, to aid dissociation of COs into single cells repeated pipetting with a 1000ul pipette was performed after 5 minutes of, and at end of 10 minutes of incubation. To neutralize accutase a neutralization medium was prepared from IMDM (Thermo Fisher Scientific, Cat. No. 21980-032) and 10% FBS. 4ml of neutralization medium was added per tube. The cell suspension was then centrifuged for 5

minutes at 600g. The supernatant was removed, and the cell pellet was resuspended with 200ul of DPBS-/-, cell pellet was resuspended to single cells by mechanical force through repeated pipetting. Another 200ul DPBS-/- were added to create a final 400ul of cell suspension per sample.

Live/Dead (L/D) stain (Thermo Fisher Scientific, Cat. No. L10119) were added to the single cell suspension at a concentration of 1:1000 and were incubated at RT in darkness for 30 minutes. After incubation of L/D stain each sample was split into two tubes, one sample for staining and one sample to be kept unstained. 10ml of DPBS-/- was added and centrifuged for 5 minutes at 600g to wash away excess antibodies. Supernatant was removed and sample was resuspended in 400µl DPBS-/-. 1 ml of ice cold 90% methanol was added dropwise to fixate the cells, and then incubated for 20 minutes in -20°C. From this point onwards samples were kept on ice. Flow buffer was prepared from PBS added 0.2% v/v BSA (Sigma Aldritch, Cat. No. 9647). 4ml of ice-cold flow buffer was added per tube, and then centrifuged for 5 minutes at 600g. Supernatant was removed leaving 200µl to resuspend the sample back into single cell solution. Antibodies were prepared and added to the stained samples, antibody panel used for flow cytometry is listed in **Table 3.6**. Antibodies were incubated for 30 minutes on ice in darkness. Each sample was added 4ml flow buffer, then centrifuged at 600G for 5 minutes. Supernatant was then aspirated leaving 300µl to resuspend the sample. Samples were kept on ice in the dark until flow cytometry was performed, data acquisition was performed within a few hours of the sample preparation Flow cytometry was ran on the BD LSR Fortessa (BD Biosciences).

Table 3.6 Antibodies used for flow cytometry with concentrations used.

Flow Cytometry Antibodies.			
Name	**Supplier**	**Catalogue Number**	**Concentration**
Human/Mouse SOX2 Alexa Fluor® 488-conjugated Antibody	Biotechne	IC2018G	1:200
MAP-2 Antibody (A-4) (PE)	Santa Cruz Biotechnology	SC-74421	1:200
VDAC1/Porin Antibody (B-6) (647)	Santa Cruz Biotechnology	SC-390996	1:200
NDUFB10 Antibody (OTI1H6)	Novus Biologicals	NBP2-72915AF405	1:200

3.6.1 Gating Strategy and Analysis.

Flow cytometry data was analyzed using FlowJo V10.8.1. For the analysis we identified the main population of live single cells. First, we displayed the cell population in forward scatter area (FSC-A) against side scatter area (SSC-A) to identify the main cell population as shown in **Figure 3.1A**. Second, single cells were identified, and gates were created by visualizing forward scatter height (FSC-H) against FSC-A, and side scatter height (SSC-H) against SSC-A as shown in **Figure 3.1B & 3.1C**, these gates are created to exclude cells that have clumped together in 2 or more cells and are thus read by the flow cytometer as a single cell. Lastly the live cell population was selected by visualizing cells stained positive for APC-Cy7-A, the channel where we expect to see the L/D stain. L/D stain is expected to stain dead cells, so the negative population was selected for creating the gate as shown in **Figure 3.1D**.

Gating for positive expression was created from the unstained samples individually for each cell line, serving as a negative control. Gates were created over the main population visualized in each channel against FSC-A while trying to minimize the amount that ends up within the gate from autofluorescence (kept to at least less than 10%.) as shown in **Figure 3.1E, 3.1F, 3.1G, & 3.1H**, the gates created were then transferred to the stained population to give a quantification of the cells that are positively stained for each marker. For quantification, the median fluorescent intensity (MFI) was calculated for each stain using the "median" statistics function. The final MFI value was calculated by subtracting the MFI value of the unstained samples from the MFI of the stained samples individually for each stain.
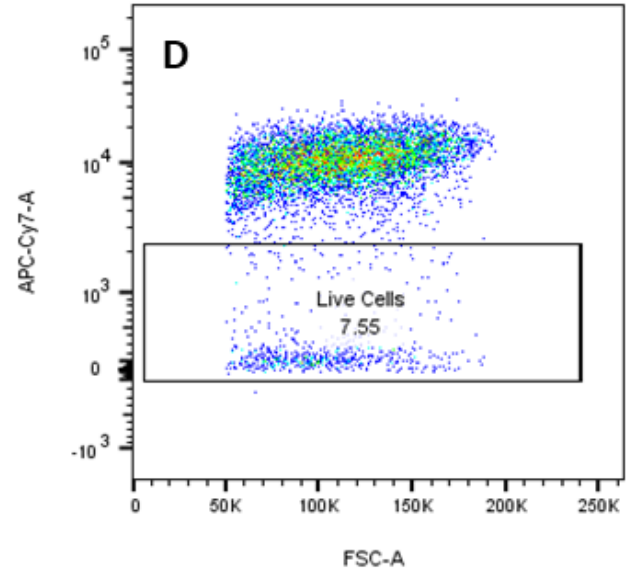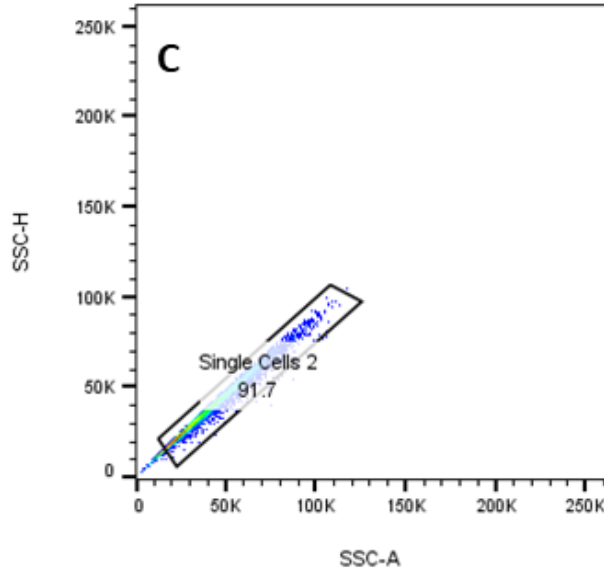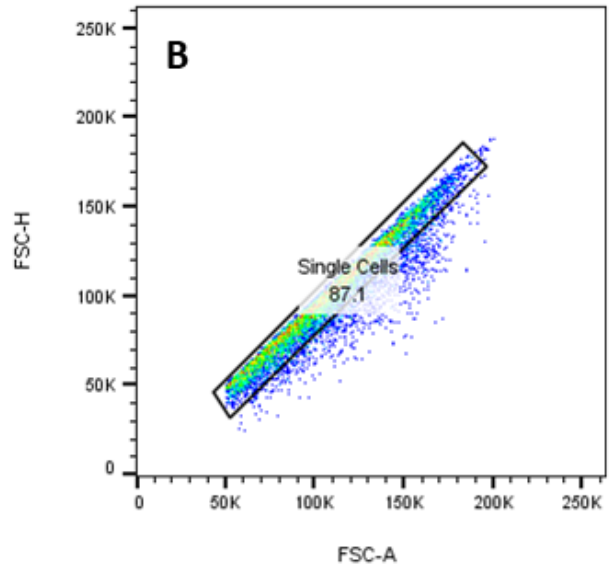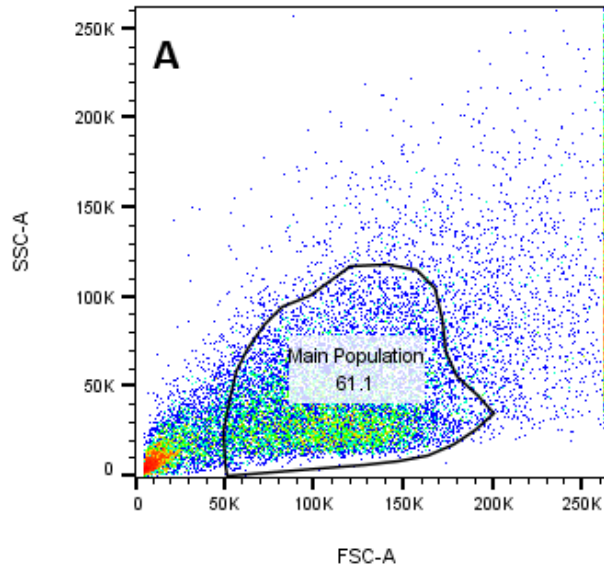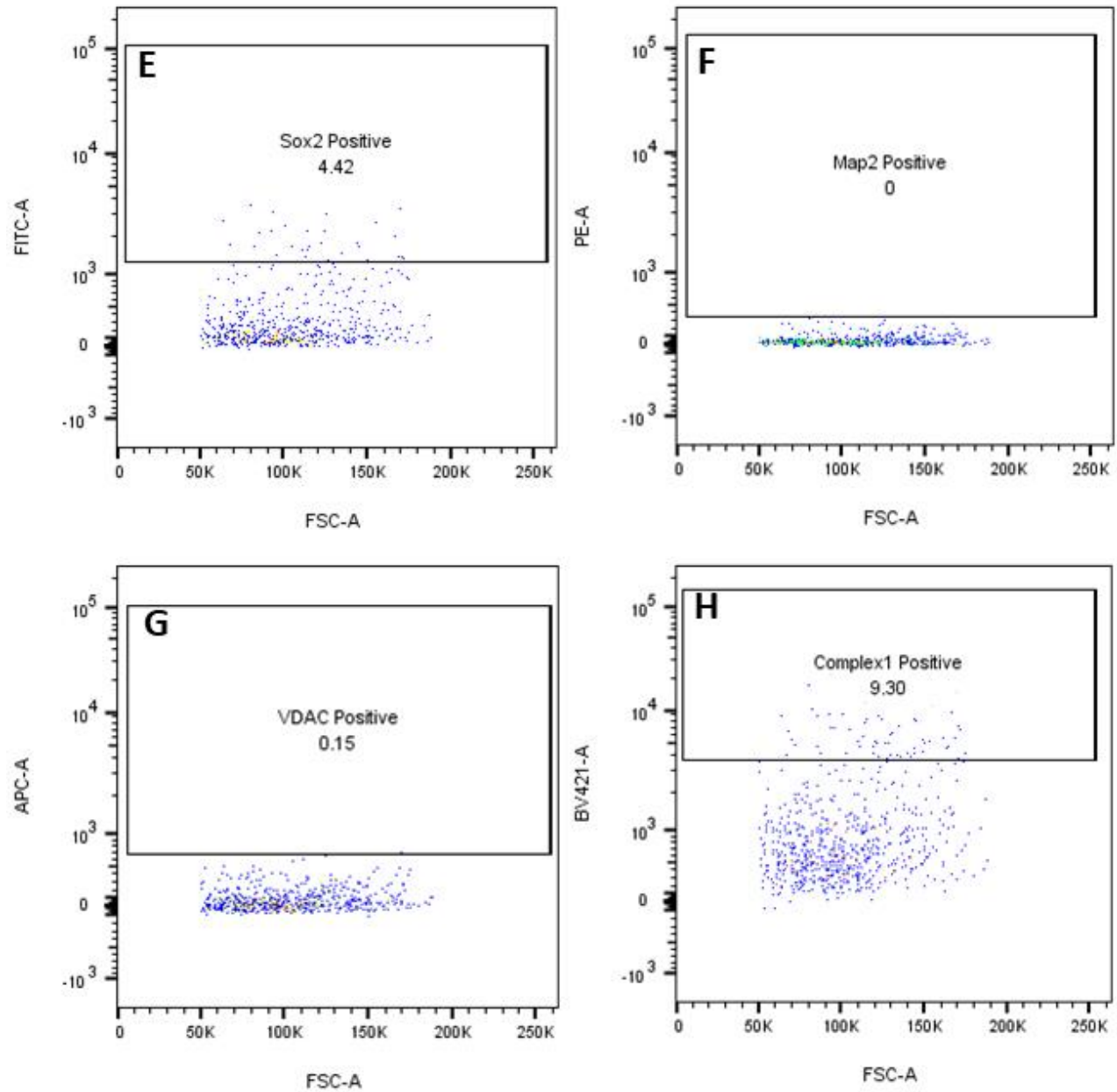
Figure 3.1 Flow cytometry gating strategy. A*: Gating for main population.* ***B & C****: Gating for single cell population as a result of FSC and SSC.* ***D****: Gating for live cell population as a result of L/D staining, the negative population is selected as L/D stain is expected to stain positivley in dead cells.* ***E****: Gating for Sox2 positive cells.* ***F****: Gating for Map2 positive cells.* ***G****: Gating for VDAC positive cells.* ***H****: Gating for C1 positive cells (NDUFB10). Data aquisistion was performed using BD LSR Fortessa. Data analysis was performed in FlowJo V10.8.1. All shown gates are from unstained control sample.*

3.7 Single cell RNA (scRNA) analysis

The scRNA analysis was performed in collaboration with Singleron Biotechnologies. Preparation of COs used for the scRNA analysis was performed before the start of this project and data analysis was performed externally as part of the collaboration. This collaboration is still ongoing but some of the results have been included to help further elucidate our other data. The protocols used relevant to this project are detailed below.

3.7.1 Preparation and lysis of organoids

Organoids were collected from their culture medium, washed with 1x PBS (Gibco, Cat. No.10010-23) and dissociated with ophthalmic scissors to finely cut pieces of 1-2 mm. The pieces were digested in 2 ml CellLive™ Tissue Dissociation Solution (Singleron Biotechnologies, Cat. No. 1190062) at 37°C for 15 minutes in a 15-ml centrifuge tube (Sarstedt, Cat. No. 62.5544.003) with continuous agitation on a thermal shaker. The state of dissociation was checked at regular intervals under a light microscope. Following digestion, the suspension was filtered using a 40-µm sterile strainer (Greiner, Cat. No. 542040). The cells were centrifuged at 350xg for 5 minutes at 4°C and the cell pellets were resuspended in 1 ml PBS. Cells were stained with a 0.4% v/v solution of Trypan Blue (Gibco, Cat. No. 15250-061) and the cell number and viability were calculated in a hemacytometer under a light microscope.

3.7.2 Tagging and analysis of RNA

The single cell RNA-seq libraries were constructed using (GEXSCOPE™ Single Cell RNAseq Library Kit, Singleron Biotechnologies, cat no. 4161031) according to manufacturer´s instructions. Briefly, for each library, the concentration of the single-cell suspension was adjusted to $3x10^5$ cells/ml with PBS and the suspension was loaded onto an SD microfluidic chip to capture 6000 cells. Paramagnetic beads conjugated to oligodT probes that carry a unique molecular identifier (UMI) and a barcode unique to each bead (from the same kit) were loaded, after which the cells were lysed. The beads bound to polyadenylated mRNA were extracted from the chip and reverse transcribed into cDNA at 42°C for 1.5 hours, and the cDNA amplified by PCR. The cDNA was then fragmented and ligated to indexed Illumina adapters. The fragment size distribution of the final amplified library was obtained on an Agilent Fragment Analyzer.

3.7.3 Cell type annotation

To identify distinct cell populations based on shared and unique patterns of gene expression, we performed dimensionality reduction and unsupervised cell clustering using single cell multi-resolution marker-based annotation scMRMA[32] (https://github.com/JiaLiVUMC/scMRMA) with cutoff of significant p value smaller than 0.05 for the fisher test for the significant cell type enrichment from 20 nearest neighbors. Cell type marker genes were obtained from the PanglaoDB database (https://panglaodb.se/).

3.8 Data analysis

Statistical analyses were performed on data from MFI-analysis of fixed immunofluorescent samples, to determine if differences between Patient lines and control were significant, as well as on differences between Patient and NR-treated Patient lines. Significance was determined by non-directional Mann-Whitney U-test, $P \leq .05$ were considered significant and $P \leq .01$ were considered highly significant. Critical values for determining P-values were selected as shown in **Table 3.1**.

Table A5.07: Critical Values for the Wilcoxon/Mann-Whitney Test (U)

Nondirectional α=.05 (Directional α=.025)

n_1 \ n_2	1	2	3	4	5	6	7	8	9	10	11	12	13	14	15	16	17	18	19	20
1	-	-	-	-	-	-	-	-	-	-	-	-	-	-	-	-	-	-	-	-
2	-	-	-	-	-	-	-	0	0	0	0	1	1	1	1	1	2	2	2	2
3	-	-	-	-	0	1	1	2	2	3	3	4	4	5	5	6	6	7	7	8
4	-	-	-	0	1	2	3	4	4	5	6	7	8	9	10	11	11	12	13	13
5	-	-	0	1	2	3	5	6	7	8	9	11	12	13	14	15	17	18	19	20
6	-	-	1	2	3	5	6	8	10	11	13	14	16	17	19	21	22	24	25	27
7	-	-	1	3	5	6	8	10	12	14	16	18	20	22	24	26	28	30	32	34
8	-	0	2	4	6	8	10	13	15	17	19	22	24	26	29	31	34	36	38	41
9	-	0	2	4	7	10	12	15	17	21	23	26	28	31	34	37	39	42	45	48
10	-	0	3	5	8	11	14	17	20	23	26	29	33	36	39	42	45	48	52	55
11	-	0	3	6	9	13	16	19	23	26	30	33	37	40	44	47	51	55	58	62
12	-	1	4	7	11	14	18	22	26	29	33	37	41	45	49	53	57	61	65	69
13	-	1	4	8	12	16	20	24	28	33	37	41	45	50	54	59	63	67	72	76
14	-	1	5	9	13	17	22	26	31	36	40	45	50	55	59	64	67	74	78	83
15	-	1	5	10	14	19	24	29	34	39	44	49	54	59	64	70	75	80	85	90
16	-	1	6	11	15	21	26	31	37	42	47	53	59	64	70	75	81	86	92	98
17	-	2	6	11	17	22	28	34	39	45	51	57	63	67	75	81	87	93	99	105
18	-	2	7	12	18	24	30	36	42	48	55	61	67	74	80	86	93	99	106	112
19	-	2	7	13	19	25	32	38	45	52	58	65	72	78	85	92	99	106	113	119
20	-	2	8	14	20	27	34	41	48	55	62	69	76	83	90	98	105	112	119	127

Nondirectional α=.01 (Directional α=.005)

n_1 \ n_2	1	2	3	4	5	6	7	8	9	10	11	12	13	14	15	16	17	18	19	20
1	-	-	-	-	-	-	-	-	-	-	-	-	-	-	-	-	-	-	-	-
2	-	-	-	-	-	-	-	-	-	-	-	-	-	-	-	-	-	-	0	0
3	-	-	-	-	-	-	-	-	0	0	0	1	1	1	2	2	2	2	3	3
4	-	-	-	-	-	0	0	1	1	2	2	3	3	4	5	5	6	6	7	8
5	-	-	-	-	0	1	1	2	3	4	5	6	7	7	8	9	10	11	12	13
6	-	-	-	0	1	2	3	4	5	6	7	9	10	11	12	13	15	16	17	18
7	-	-	-	0	1	3	4	6	7	9	10	12	13	15	16	18	19	21	22	24
8	-	-	-	1	2	4	6	7	9	11	13	15	17	18	20	22	24	26	28	30
9	-	-	0	1	3	5	7	9	11	13	16	18	20	22	24	27	29	31	33	36
10	-	-	0	2	4	6	9	11	13	16	18	21	24	26	29	31	34	37	39	42
11	-	-	0	2	5	7	10	13	16	18	21	24	27	30	33	36	39	42	45	46
12	-	-	1	3	6	9	12	15	18	21	24	27	31	34	37	41	44	47	51	54
13	-	-	1	3	7	10	13	17	20	24	27	31	34	38	42	45	49	53	56	60
14	-	-	1	4	7	11	15	18	22	26	30	34	38	42	46	50	54	58	63	67
15	-	-	2	5	8	12	16	20	24	29	33	37	42	46	51	55	60	64	69	73
16	-	-	2	5	9	13	18	22	27	31	36	41	45	50	55	60	65	70	74	79
17	-	-	2	6	10	15	19	24	29	34	39	44	49	54	60	65	70	75	81	86
18	-	-	2	6	11	16	21	26	31	37	42	47	53	58	64	70	75	81	87	92
19	-	0	3	7	12	17	22	28	33	39	45	51	56	63	69	74	81	87	93	99
20	-	0	3	8	13	18	24	30	36	42	46	54	60	67	73	79	86	92	99	105

U_{obt} is the lesser of the two calculated test statistics (U_1 & U_2). If $U_{obt} \leq U_{crit}$, reject H_0.

Dashes (-) indicate that the sample size is too small to reject the Null Hypothesis at the chosen α level.

If n > 20 this table cannot be used. A **p** can be computed for U_{obt}, using the normal distribution approximation:

$$z_U = \frac{\left| U_{obt} - \left(\frac{n_1 n_2}{2} \right) \right|}{\sqrt{\dfrac{n_1 n_2 (n_1 + n_2 + 1)}{12}}}$$

Table 3.1 Critical Values for Mann-Whitney U-test. *Table taken from (Hanifah, n.d.)*

4. Results

4.1 Human iPSCs

In this study, we included two clones of iPSCs generated from POLG patients carrying the mutations p.A467T (c.1399G>A) and p.P589L (c.1766C>T), referred to in results as Patient 1 and Patient 2. A control iPSC clone generated from commercially available fibroblast line CRL2097 fibroblasts (ATCC, CRL-2097™.), referred to as simply Control in results. Reprogramming of iPSCs were performed by overexpression of the transcription factors Sox2, Oct4, KLF4, and c-Myc, delivered through Sendai virus vectors to fibroblasts. The quality of iPSCs were assessed during culture by observation of cell morphology, with a preference for undifferentiated colonies with clear edges (**Figure 4.1**).
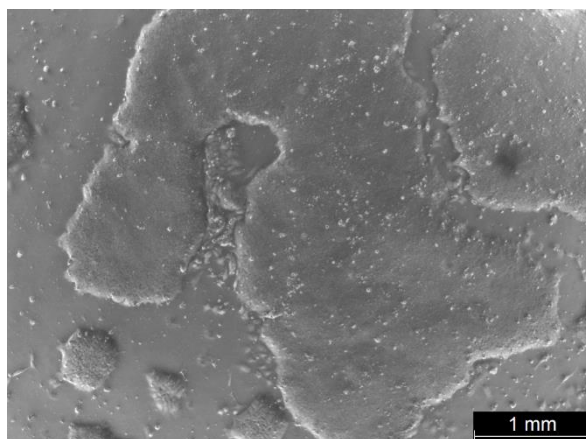
Figure 4.1 Representative image of iPSC culture showing large colony of undifferentiated cells. The image was taken with Leica brightfield microscope. Scalebar is set to 1 mm.

4.2 Generation of COs from iPSCs

To establish the differentiation protocol, the control line was used. Control iPSCs were dissociated into single cells and seeded in 96 well plate at a density of 9000 cells per well to form EBs. Neuroectodermal lineage was promoted by addition of NIM for 10 days. Transfer of iPSCs to neural induction culture marked as day 0 of CO differentiation. Clear formation of EBs could be observed by day3 (**Figure 4.2**). Differentiation and formation of neural sphere structure progressed through day 3 to day 10.

On day 10 of differentiation, EBs were embedded in Matrigel membrane matrix and transferred from neural induction culture to organoid spinning co-culture in 6 well plates. By day 13, organoids within Matrigel matrix beads exhibited rapid expansion. Organoids expressed continuous rapid growth from day 13 and onward. This accelerated growth persisted from day 13 onwards, with organoids gradually shedding their Matrigel beads. On day 39 of differentiation, organoids were considered mature, presenting as large heterogenous structures measuring approximately 4 to 5mm in diameter (**Figure 4.2**).
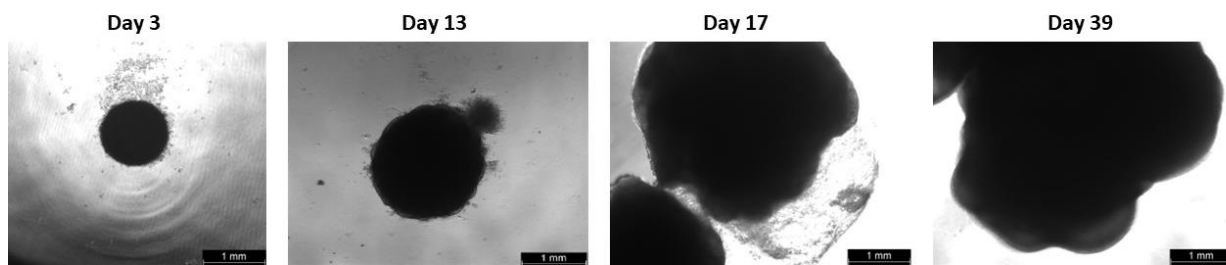
Figure 4.2 Representative images of CO generation from day 3, day 13, day 17 and day 39 of differentiation highlighting the growth over time. *Images captured in Leica brightfield microscope. Scalebar is set to 1mm.*

4.3 Characterization of the COs differentiated from iPSCs.

The successful conversion of iPSCs into COs was assessed by immunofluorescent staining of mature organoids with specific markers that are characteristic of mature COs (3-month-old). These markers were: Microtubule associated protein 2 (MAP2) a marker found in mature neurons, Sex-determining region box-2 (SOX2) as a marker found mostly in pluripotent or self-renewing cells, and Glial fibrillary acidic protein (GFAP), commonly found in developing brain astrocytes and glial cells. Nuclear staining with DAPI was used to distinguish individual cells.
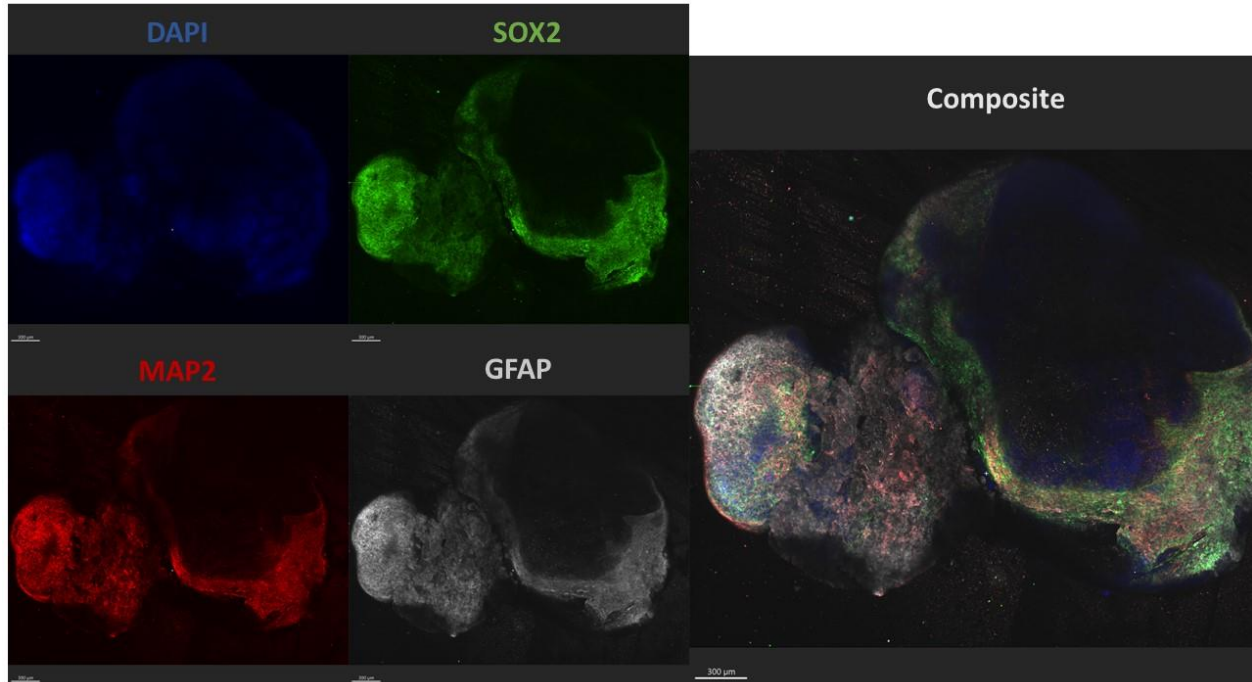
Figure 4.3 Representative image of expression of MAP2, SOX2, and GFAP in whole organoid fluorescent imaging. Images are created as composites of several images. Images were taken with Andor Dragonfly fluorescent microscope. Scalebar (bottom left) is set to 300 μm.

Upon examination of whole organoid fluorescent images, we observed positive staining for all three tested markers, primarily concentrated in the outer layers of the organoids (**Figure 4.3**). With the exception of the more permeable DAPI stain, marker expression remained largely confined to the edges of the organoid. All markers were uniformly expressed across the stained sample, without apparent spatial segregation.

In the stained COs, MAP2 staining was e highly specific in the stained tissues, with distinct neuronal morphology clearly visible axons (**Figure 4.4**). SOX2 expression appeared ubiquitous across the sample tissue and seemed primarily localized in the cell body (**Figure 4.4**). GFAP staining showed strong positive staining throughout the stained COs, though it lacked specificity and displayed considerable of overlap with both MAP2 and SOX2 expression (**Figure 4.4**).

In deeper sections of the organoids, we observed nuclei arranged in circular patterns surrounding an empty space (**Figure 4.5**). These formations are reminiscent of the columnar neuroepithelium comprising neural rosettes (**Figure 4.5**).
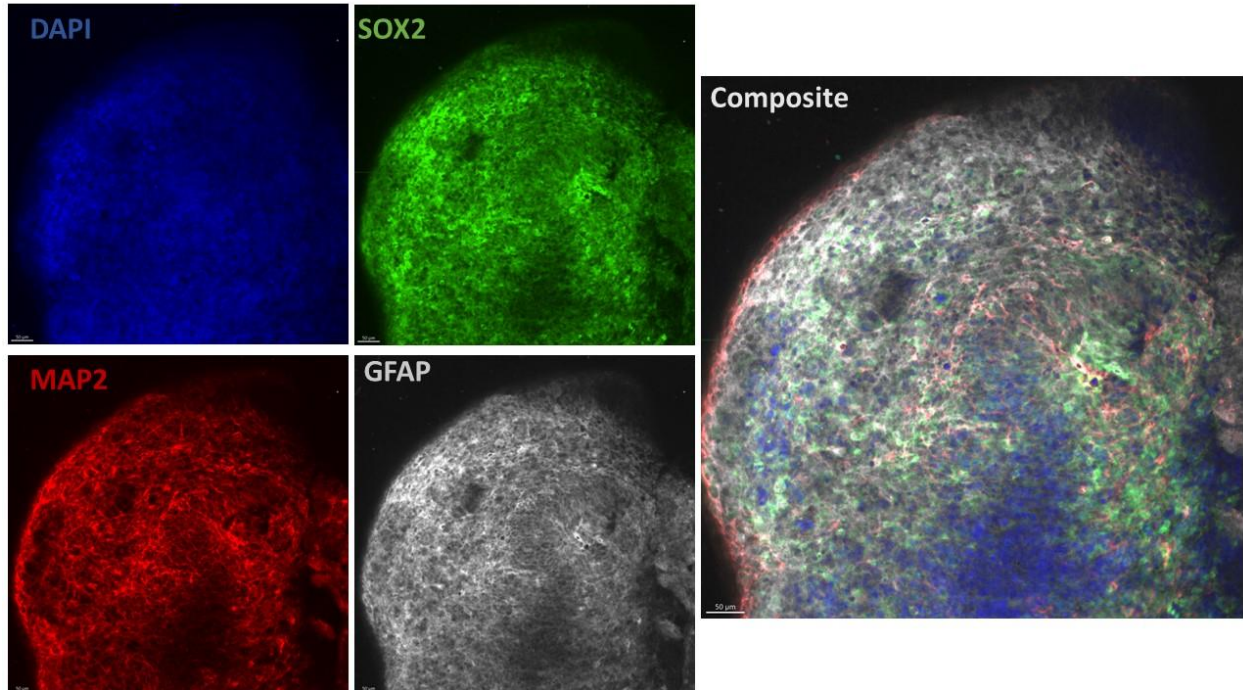
Figure 4.4 Representative image of an area of a whole-body stained organoid. Images were taken with Andor Dragonfly fluorescent microscope. Scalebar (bottom left) is set to 50 µm.
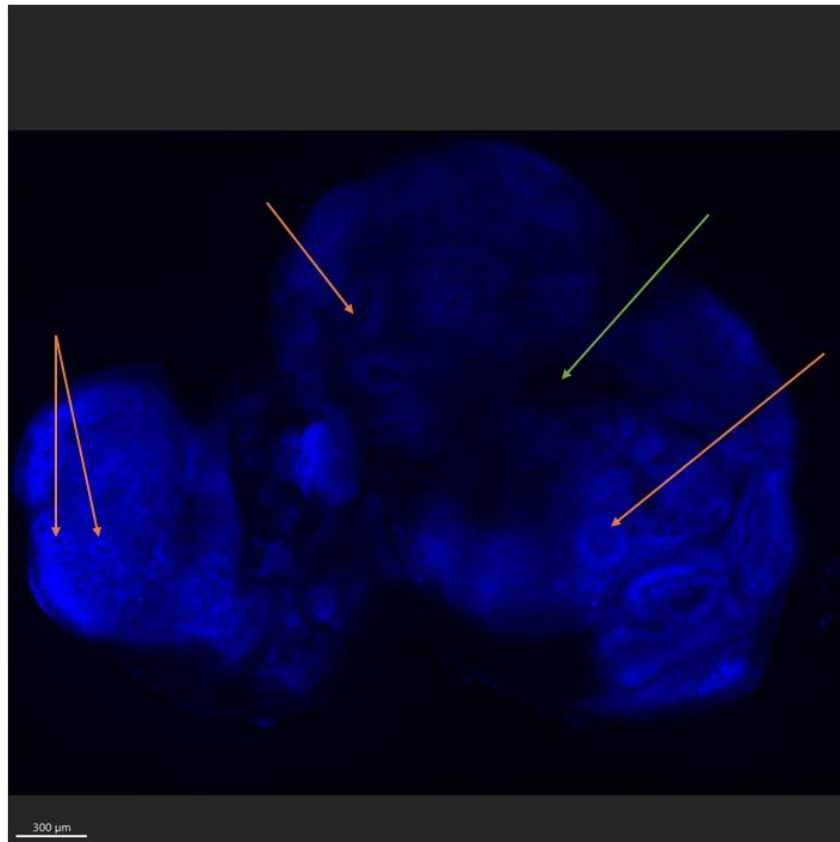
Figure 4.5 Representative image of deep layer of organoid with DAPI stain. Orange arrows point to circular configuration of nuclei reminiscent of neural rosette structures. Green arrow shows area devoid of DAPI assumed to be either apoptotic or left unstained due to limited permeability. Scalebar (bottom left) is set to 300 μm.

4.4 Comparison of the morphological changes in control and patient COs.

During the differentiation process, no noticeable differences were found between the control and patient lines in terms of the size, morphology, or timing of EB formation. However, an interesting observation was made with regards to organoid fusion in patient lines. It was frequently noted that multiple organoids from patient lines would merge with one another when in co-culture, resulting in fused structures. In most cases, these organoids appeared to combine with at least one other, but instances of three to four organoids fusing together were also documented (**Figure 4.6**).

In contrast, the organoids from the control line did not exhibit similar fusion behavior. The factors leading to these differing outcomes could be manifold. For example, the patient-derived organoids may have alterations in cell adhesion molecules or in the expression of extracellular

matrix proteins, which could facilitate fusion. Further research is necessary to elucidate the mechanisms and implications of this distinctive fusion phenomenon in patient-derived organoids.
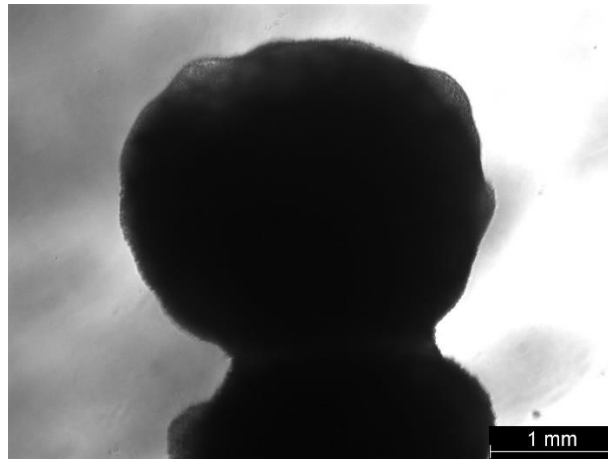

Figure 4.6 Representative image of two fused organoids. The image was taken with Leica Brightfield Microscope. Scalebar is set to 1 mm.

The staining for characterization was also carried out on a patient organoid to investigate any differences in the layout, or composition between patient and control. The patient organoid was not seen to show any substantial differences to the control organoid beyond being smaller sized and displaying a more varied topography (**Figure 4.7**). Distinct MAP2 positive cells bearing neuronal morphology were seen, as well as seemingly ubiquitous expression of SOX2 and GFAP with GFAP expression seeming unspecific with high overlap with both SOX2 and MAP2 expression (**Figure 4.8**). Similar neural tube structures were observed in the control were observed in the deeper layers with DAPI staining (**Figure 4.9**).
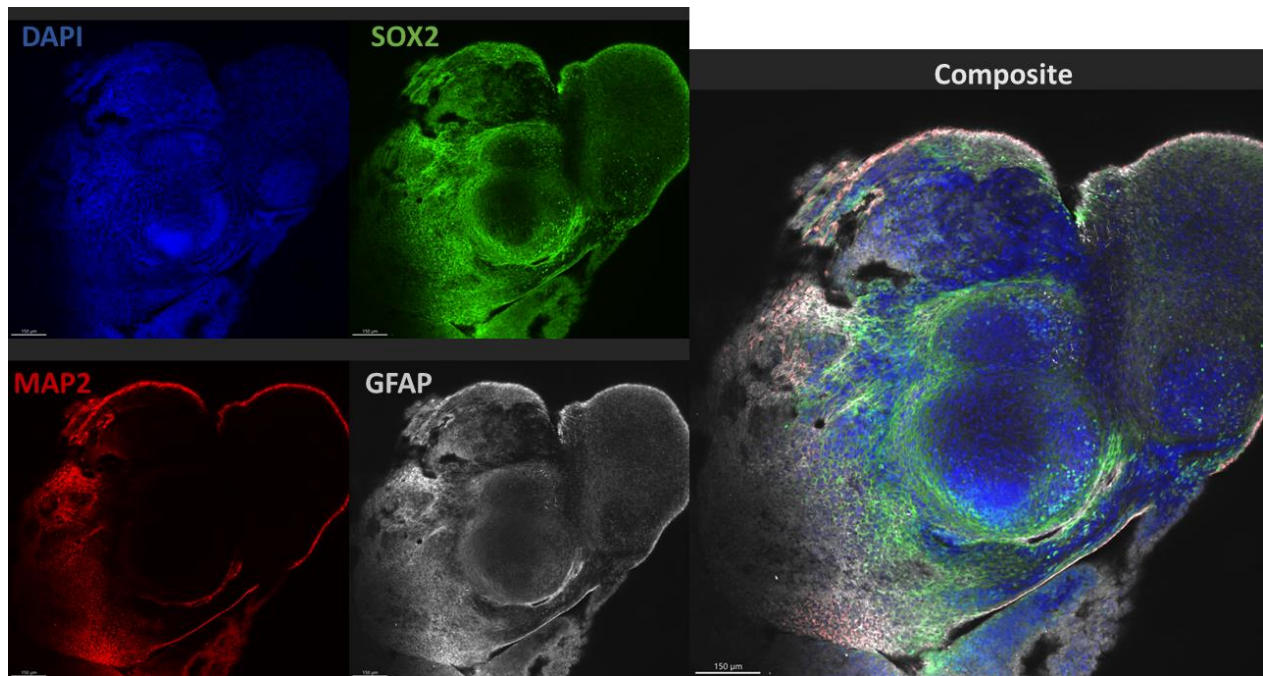
Figure 4.7 Representative image of expression of MAP2, SOX2, and GFAP in whole organoid fluorescent imaging of patient line organoid. Images are created as composites of several images. Limited stain distribution is as a result of varied topography and limited stain permeability. Images were taken with Andor Dragonfly fluorescent microscope. Scalebar (bottom left) is set to 150 μm.
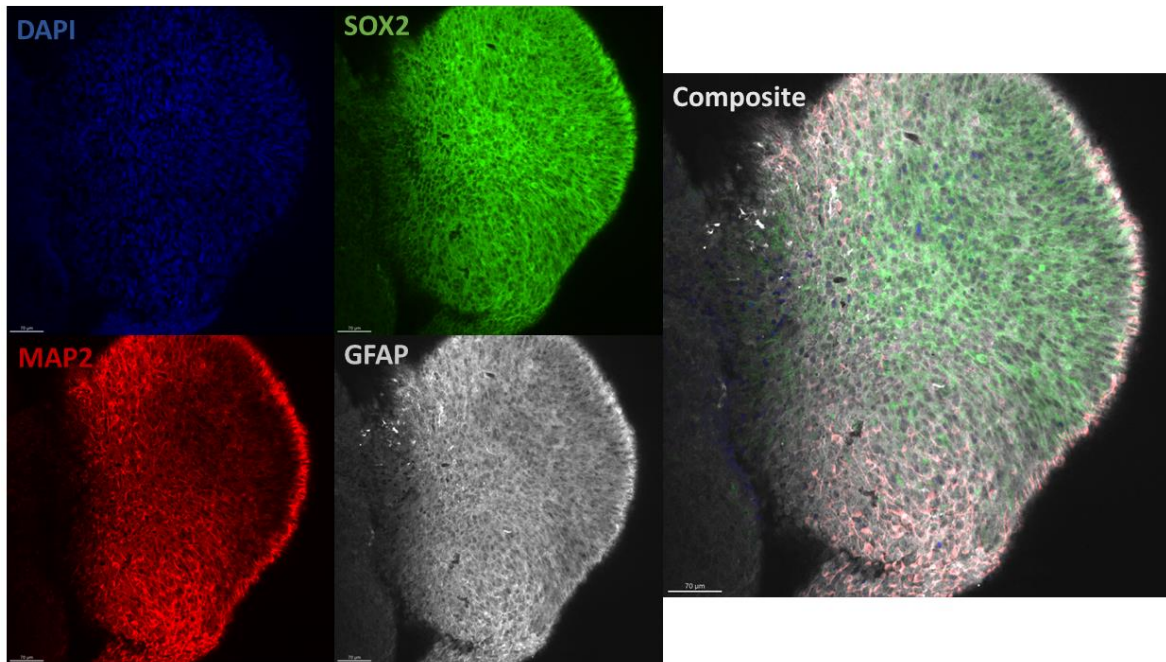
Figure 4.8 Representative image of an area of a whole-body stained patient organoid. Images were taken with Andor Dragonfly fluorescent microscope. The scalebar (bottom left) is set to 70 µm.
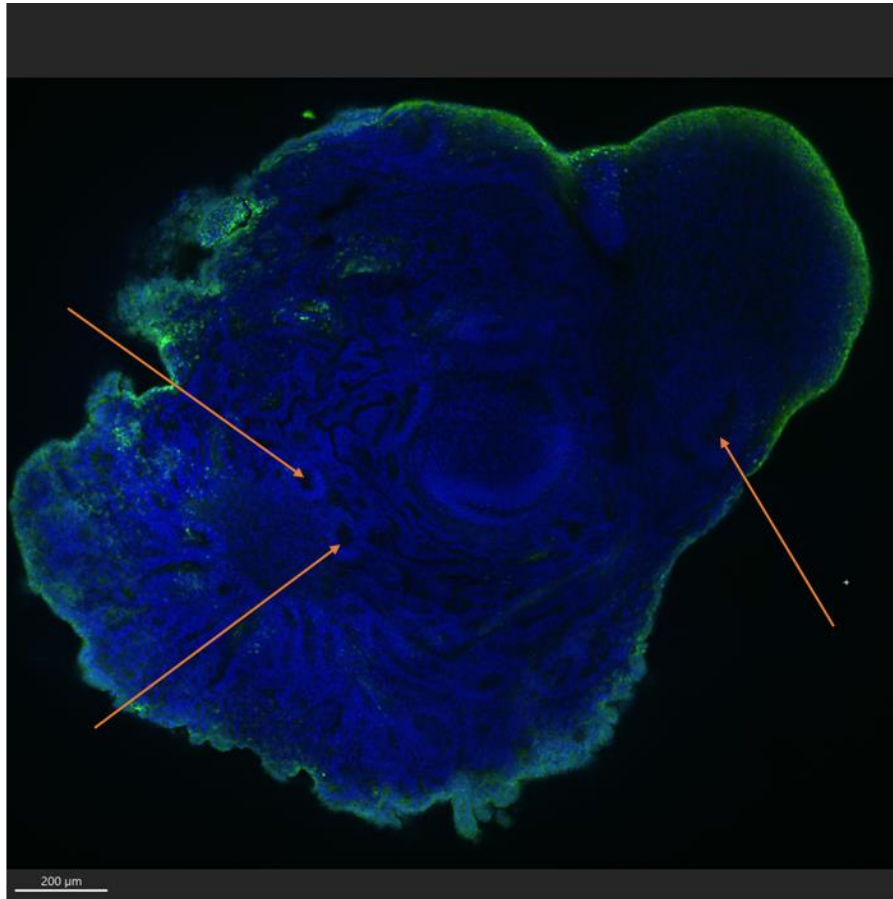
Figure 4.9 Representative image of deep layer of patient line organoid with DAPI stain.
Orange arrows point to circular configuration of nuclei reminiscent of neural rosette structures.
Scalebar (bottom left) is set to 200 μm.

4.5 Comparison of mitochondrial changes in control and patient COs using flow cytometry.

Previous studies involving tissues derived from POLG-disease patients have reported C1 deficiency, neural loss, and a decline in mtDNA copy numbers (Tzoulis et al., 2013). In our current investigation, we aimed to determine if the same phenotypes would be observed in COs derived from iPSCs.

We used flow cytometry to analyze the dissociated COs, employing a set of markers which included: MAP2 for identifying mature neurons, VDAC for quantifying mitochondrial mass, mitochondrial transcription factor A (TFAM) for estimating mtDNA volume, and NDUFB10, a marker for C1, to evaluate any potential C1 depletion. At the time of this experiment, the patient-derived organoids were at day 93 post-EB formation, while the control organoids were at day 65.

Cell viability was assessed using the L/D stain, which selectively labels dead cells that have a compromised cell membrane. After gating out the positively stained cells (**Figure 3.1 D**), further analysis was conducted on the live cell populations of each line. Using our gating strategy, we found that all cell lines displayed a very low percentage of live cells (**Figure 4.10**), with fewer than 10% of the gated single-cell populations appearing as live cells. Interestingly, both patient-derived lines seemed to contain a smaller proportion of live cells compared to the control line.

We quantified the expression levels of the selected markers by calculating the MFI of the positively stained cells. The final MFI values for each sample were obtained by subtracting the MFI values of unstained samples from the stained samples, which allowed us to account for any autofluorescence. These comparative MFI values are illustrated in **Figure 4.11**.

We observed a significant decrease in MAP2 expression in both patient lines compared to the control line, suggesting a reduction in the neuronal population within the patient-derived COs. Expression of VDAC showed a slight decrease in patient 1, and a more marked reduction in Patient 2 when compared to the control, indicating diminished overall mitochondrial mass in the patient organoids. No significant change was noted in the expression of TFAM between the patient-derived lines and control, suggesting that the overall mtDNA copy number remained consistent across all samples. Finally, a reduction in NDUFB10 was noted in both patient lines relative to the control, hinting at potential C1 deficiency in the patient organoids. Further in-depth analysis will be needed to confirm these preliminary observations.
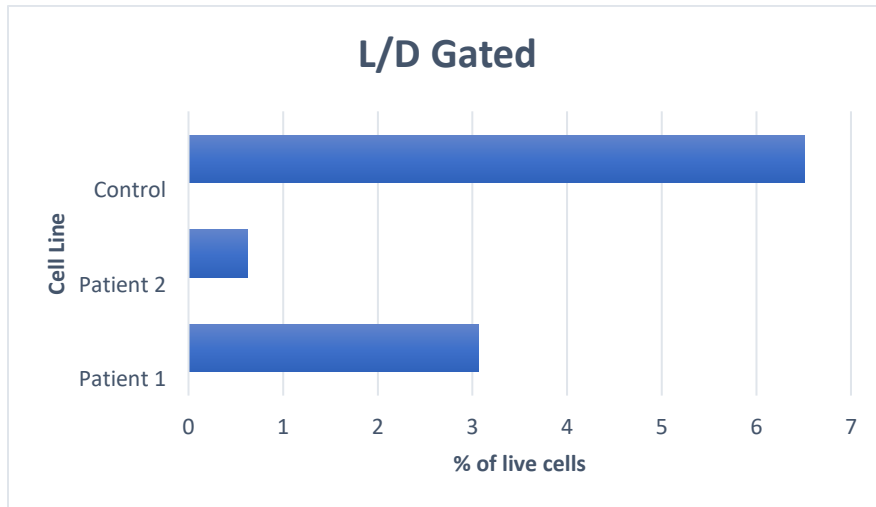
Figure 4.10 Flow cytometry data showing proportion of live cells in each sample as a result of L/D staining. *X-axis shows the percentage of live cells out of the gated single cell population, and y-axis shows the different cell lines.*
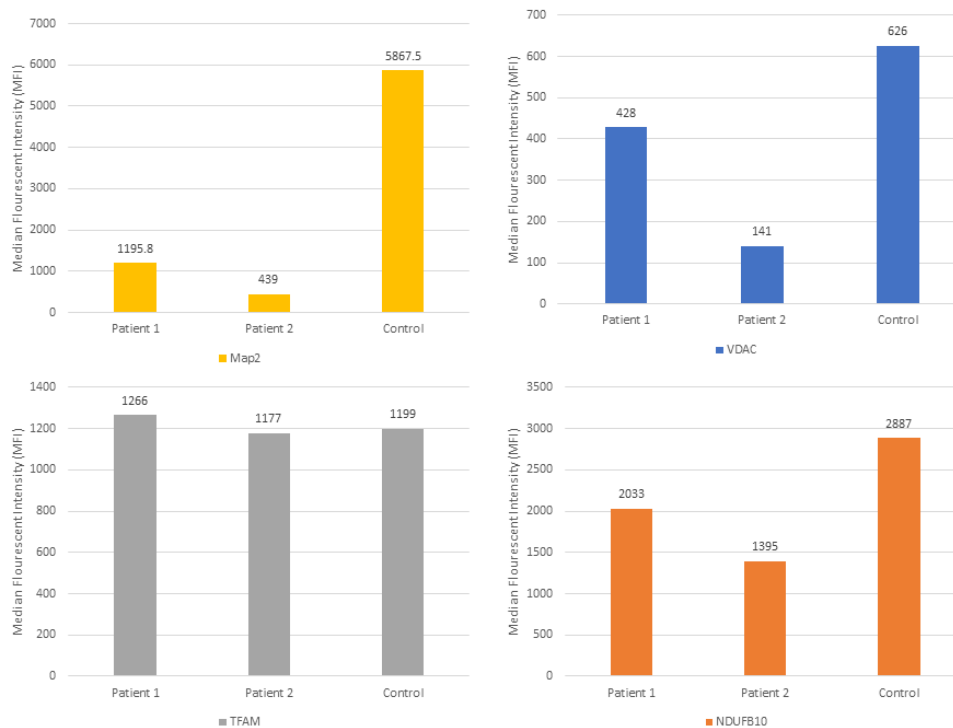

Figure 4.11 Result of flow cytometry analysis for MFI of COs*. MAP2 is used as a quantification of neuronal population, VDAC is used as a measure for mitochondrial mass, TFAM is used for quantification of mtDNA and NDUFB10 is used as a quantification of C1.*

To investigate mitochondrial depletion, we normalized the MFI values of the VDAC positive population to the MAP2 positive population for each sample. We also aimed to determine whether the mtDNA and C1 expressions were reduced in relation to the total mitochondrial volume. This we assessed by normalizing the MFI value of TFAM and NDUFB10 to the MFI value of the VDAC.

Compared to the control, the patient organoids demonstrated a significant increase in mitochondrial mass relative to the neuronal population (**Figure 4.12**). MtDNA, when normalized to mitochondrial mass, showed a minor increase in Patient 1 and a substantial increase in Patient 2 compared to the control. A similar increase was observed in C1 expression when compared to mitochondrial mass. However, these observations might be influenced by the remarkably high values in relation to the low live cell population. We noticed a substantial increase in C1 and TFAM, which could potentially be linked to autofluorescence in their respective channels.
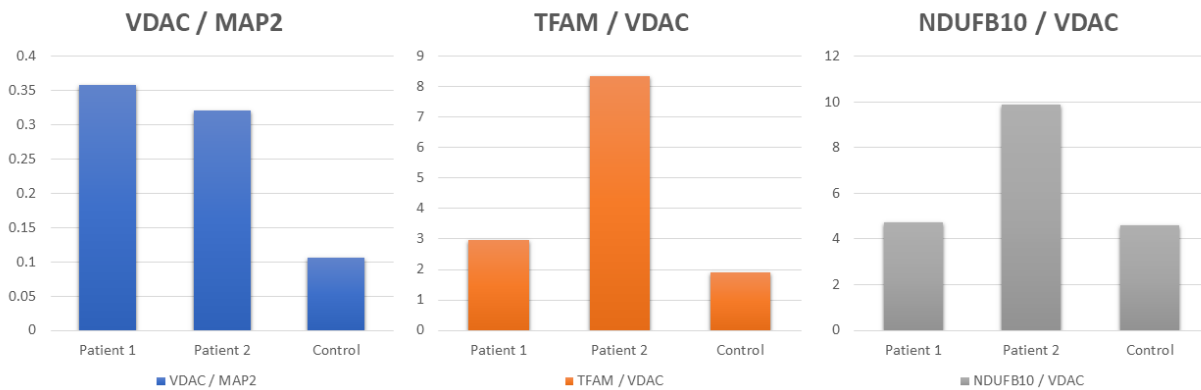

Figure 4.12 Median fluorescent values of COs obtained through flow cytometry giving values of VDAC normalized to MAP2, and TFAM and NDUFB10 normalized to VDAC.

We also measured the proportion of positively. Cells with positive staining were identified based on their respective channels, as shown in **Figure 3.1 E, F, G, and H**. The proportions of positively stained live cells are shown in **Figure 4.13.**

The analysis of the live cell proportions showed a minor decrease in MAP2 positive cells in both patient lines compared to control, but the difference was considerably smaller than what was observed in the MFI-analysis (**Figure 4.13**). Compared to the control, patient COs showed a substantial decrease in the cells stained positively for NDUFB10 and VDAC, consistent with the MFI-analysis. The patient lines also exhibited a substantial decrease in TFAM positive staining compared to what was observed in the MFI-analysis (**Figure 4.11**).

We conducted an analysis of mitochondrial mass, C1 and mtDNA depletion in the same manner as in the MFI-analysis (**Figure 4.14**). We observed a decrease in VDAC positive cells relative to MAP2 positive cells in patient lines compared to control, as well as a decrease in NDUFB10 positive stained cells relative to VDAC positive cells (**Figure 4.14**). However, compared to the control, patient line COs displayed an increase in TFAM positive cells relative to VDAC positive cells.
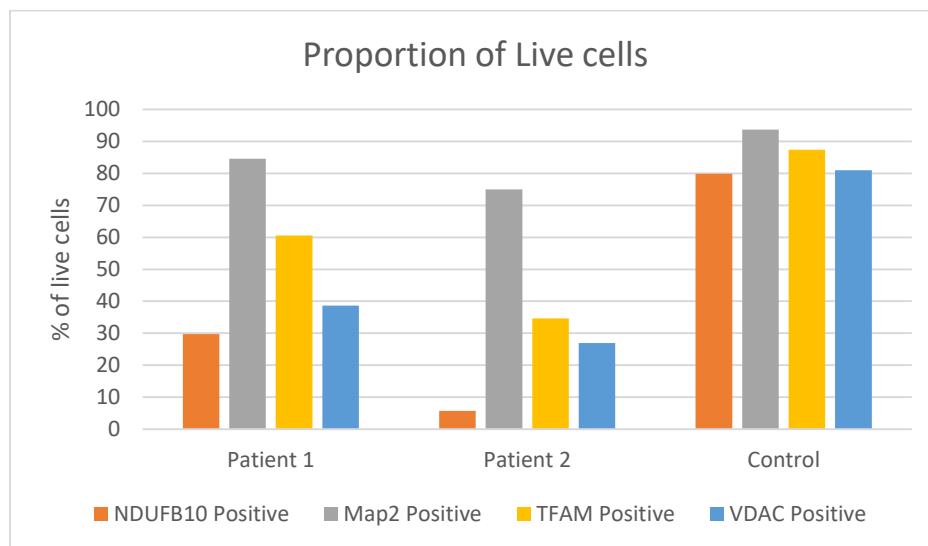

F*igure 4.13 shows the proportion of live cell gated positively stained cells based on the gating shown in Figure 3.1. Y-axis shows proportion of cells that stained positive for respective markers as percentages of the total live cell population. X-axis shows the different cell lines.*
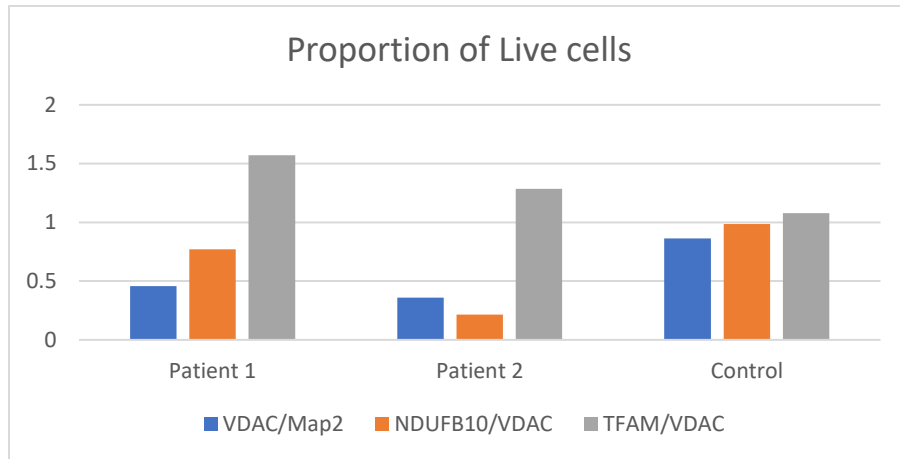
Figure 4.14 VDAC normalized to MAP2, and TFAM and NDUFB10 normalized to VDAC.
Values are calculated from proportions of live cells showing positive expression of each marker.

4.6 Comparison of the mitochondrial changes in control and patient COs using immunostaining.

In order to substantiate the findings from the flow cytometry, we undertook a fluorescent intensity evaluation of samples that were fixed and stained immunohistochemically. At the time of fixation, COs were aged 80 days for patient and 52 days for control, the staining procedure encompassed both mitochondrial and cell lineage markers.

Immunofluorescent analysis was conducted on images captured in SP8 confocal microscope. Subsequent image analysis was performed in ImageJ software, employing the threshold and measure functions. Thresholds were individually defined for each stain, based on staining pattern observed in the control samples. Thresholds were set to maximize the capture of specific staining while minimizing background noise or unspecific staining.

We executed two separate sets of the immunofluorescent analysis, The first set incorporated the mature neuronal marker MAP2, C1 marker NDUFB10 and glial/astrocyte marker GFAP. The intention of this set was to assess variations in the neuronal population and depletion of C1. The second set included VDAC, TFAM, and NDUFB10, which aimed to evaluate the potential depletion C1 and mtDNA depletion c in relation to mitochondrial mass.

Measurements from ImageJ fluorescent analysis provided the fluorescence analysis results as integrated density values, which were obtained by measuring various regions of each CO. In the

first set of staining (**Figure 4.15**), we observed a decrease in MAP2 and NDUFB10 expression in patient-derived COs compared to control COs. In contrast, the patient sample demonstrated an increase in GFAP expression compared to the control.

In the second set of staining (**Figure 4.16**) revealed a reduction in VDAC, TFAM, and NDUFB10 expression in the Patient 1 line -derived COs relative to the control. However, the Patient 2 line-derived COs did not exhibit a decrease in VDAC and NDUFB10 expression, although there was a noticeable reduction in TFAM expression. These findings highlight the intricate variations between individual patient-derived cell lines and underscore the complexity of the disease pathology.
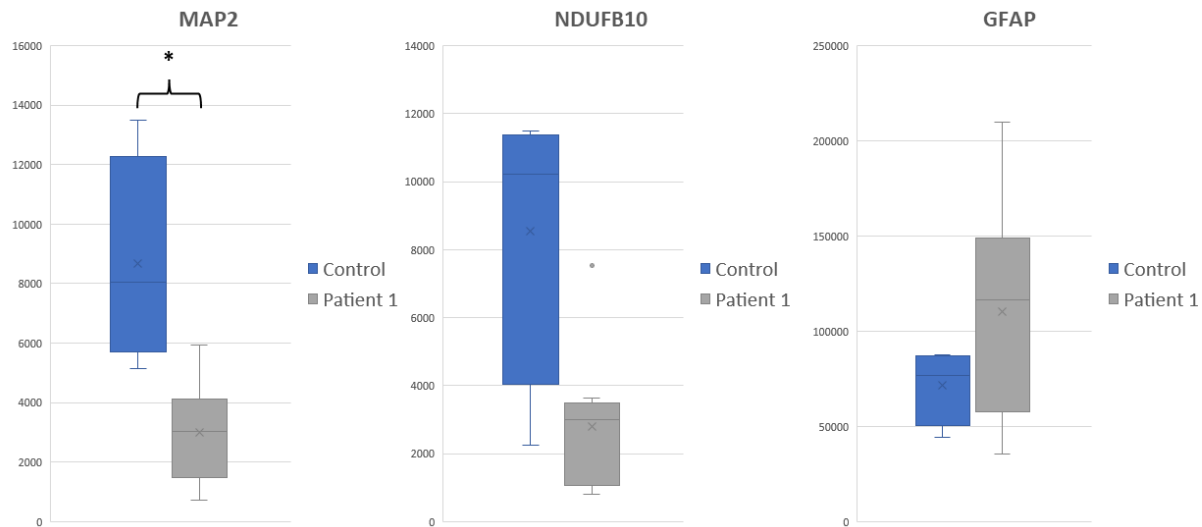

Figure 4.15 Showing integrated density values of patient and control COs for marker MAP2, NDUFB10 and GFAP. Values are obtained from measuring different regions of an individual CO of each line. Boxes show median values and upper and lower quartiles. X indicates the mean value. Whiskers show the highest and lowest values. Dots indicate outlier values. Fluorescent analysis was performed in ImageJ using the threshold and measure function. The data was represented as mean +/- SD, n= ≥ 4. Significant values (P ≤ .05) are annotated with (*).
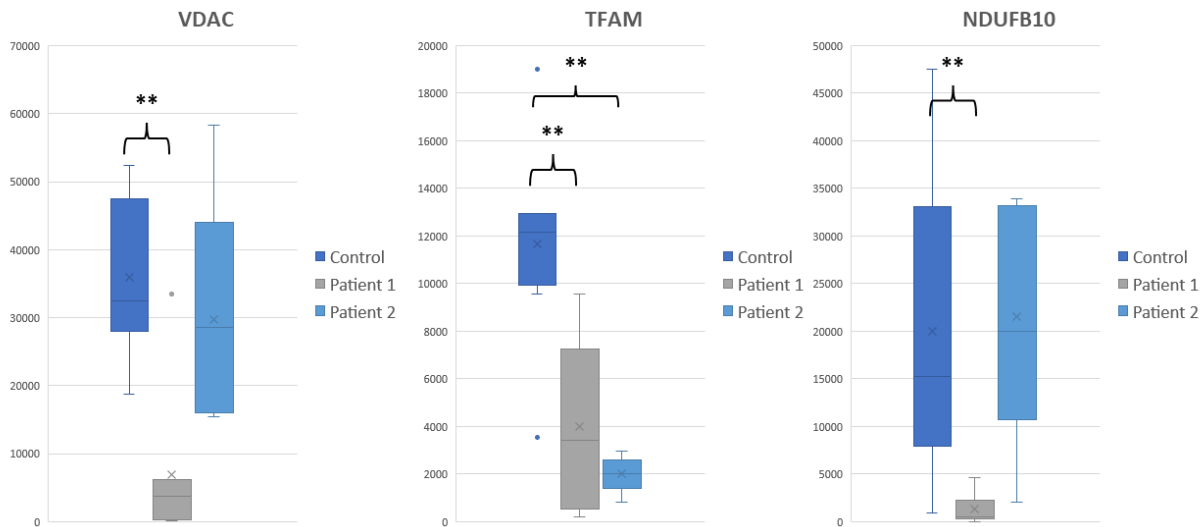
Figure 4.16 Showing integrated density values of patient and control COs for marker VDAC, TFAM and NDUFB10. Values are obtained from measuring different regions of an individual CO of each line. Boxes show median values and upper and lower quartiles. X indicates the mean value. Whiskers show the highest and lowest values. Dots indicate outlier values. Fluorescent Analysis was performed in ImageJ using the threshold and measure function. The data was represented as mean +/- SD, n= ≥ 5. Highly Significant values (P ≤ .01) are annotated with (**).

4.7 Single cell transcriptomic profiling in control

To create a better understanding of the cellular composisiton of COs we perfomed single cell RNA analysis of diccosiated COs. Cellular identity was determined for individual cells based on protein expression of certain markers using single cell multi-resolution marker-based annotation scMRMA[32] using cell type marker genes obtained from the PanglaoDB database.

scRNA analysis showed that cultured COs contained several distinct cell populations as shown in **Figure 4.17** including both varied neuronal populations, and various glial cell types such as astrocytes, ependymal cells and radial glia. The majority of neurons found in the control CO showed dopaminergic neuronal identification (70.23% of total neuronal population) with a neuronal subgroup of neuron expressing markers of both dopaminergic and glutminergic signaling dubbed 'dopamin-glutamate co-expressing neurons' (DA GLU neurons) coming in second (16.97%). Most of the rest were identified as glutaminergic neurons (10.83%) with also small populations of neural progenitors (1.92%) and GABAergic interneurons (0.05%) being

found. Among the remaining cell types radial glial cells were the most dominant consisting 16.40% of the total number of counted cells. Minor populations of astrocytes (0.04%) and ependymal cells were also identified (0.04%).
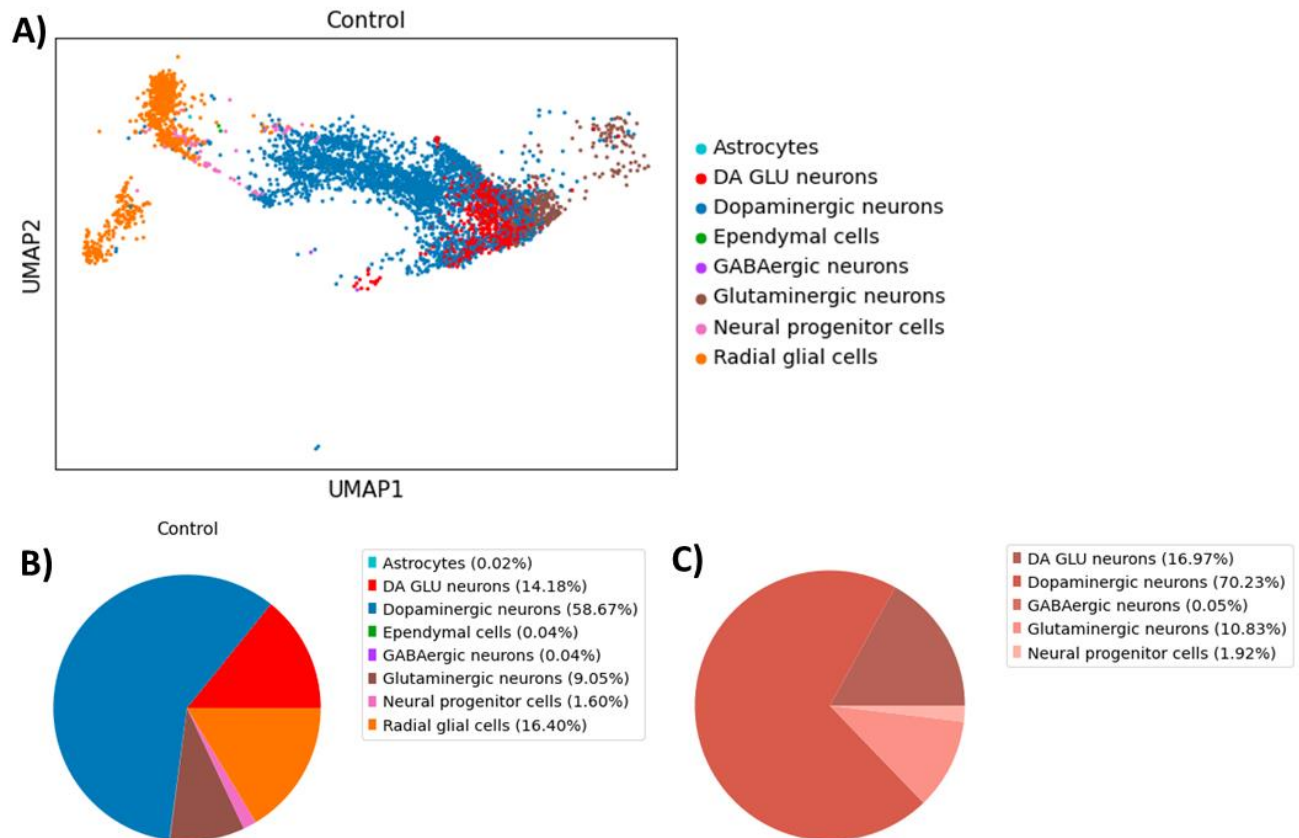

Figure 4.17. scRNA analysis data of control COs. The figure shows distribution of single cells by type according to protein expression analysis displayed in UMAP projection (A). As well as pie charts showing percentage of population by cell type (B), and distribution of neuronal types as percentages of overall neuronal population (C).

4.8 Single cell transcriptomic profiling in control versus patient

We also performed scRNA analysis on patient COs to see if we could identify changes in the cellular composition of the COs from patient to control (one organoid for each sample, **Figure 4.18**).

In patient COs we found a more varied distribution of cell types were identified compared to what was found in the control COs, including some cell types that are not expected to be found in

developing brain tissues such as fibroblasts and melanocytes. Additionaly a population of tanycytes, a type of specialized ependymal cell, was found. Patient COs showed a large decrease in the dopaminergic neuron population (40.03% of neuronal population) compared to what was found in the control COs, as well as a complete depletion of the DA GLU neuron population. Patient CO showed an increase in the population of glutaminergic (41.14%), GABAergic (8.09%) neurons and neural progenitor cells (10.74%) compared to what was seen in the control CO. We also observed an increase in all the supporting glial cell types with radial glia consisting 22.41% of the total population, astrocytes 1.27% and ependymal cells 5.25%, with the addition of 1.74% tanycytes.
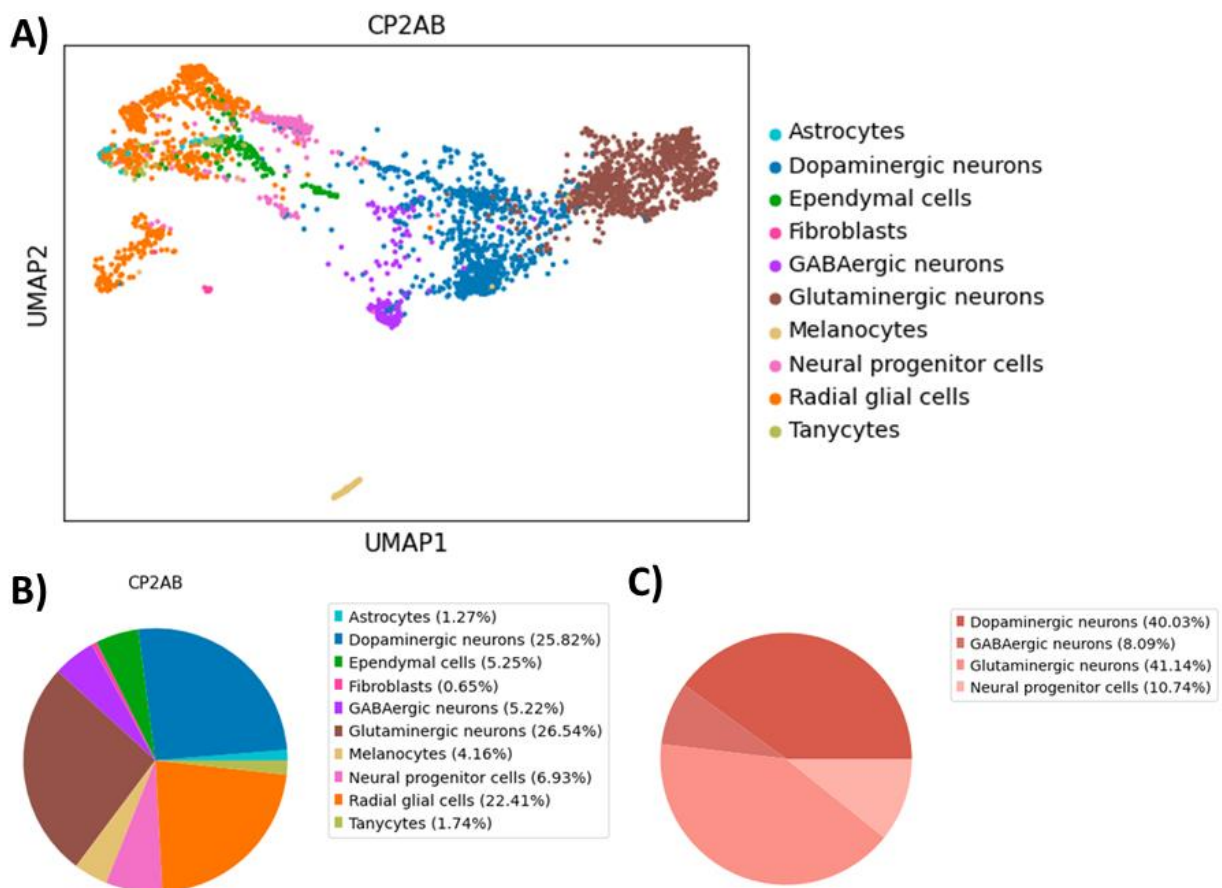

Figure 4.18 scRNA data analysis of Patient COs *showing distribution of single cells by type according to protein expression analysis displayed in UMAP projection (A). As well as pie charts showing percentage of population by cell type (B), and distribution of neuronal types as percentages of overall neuronal population (C).*

4.9 Treatment of NR in patient COs

To investigate whether NR supplementation could have a rescuing effect on organoids we treated patient-derived COs with 1 mM NR from 20th day of differentiation. We then compared data from flow cytometry of NR-treated COs to untreated COs to investigate if NR supplementation ameliorated the patient phenotype.

Initially, we investigated if NR supplementation influenced the proportion of the live cell population in a sample by comparing L/D staining of NR treated vs untreated COs (**Figure 4.19**). Patient lines showed an increase in the percentage of live cells in NR treated COs compared to untreated COs. However, NR treated control COs showed a decrease in the live cell percentage compared to the untreated sample.
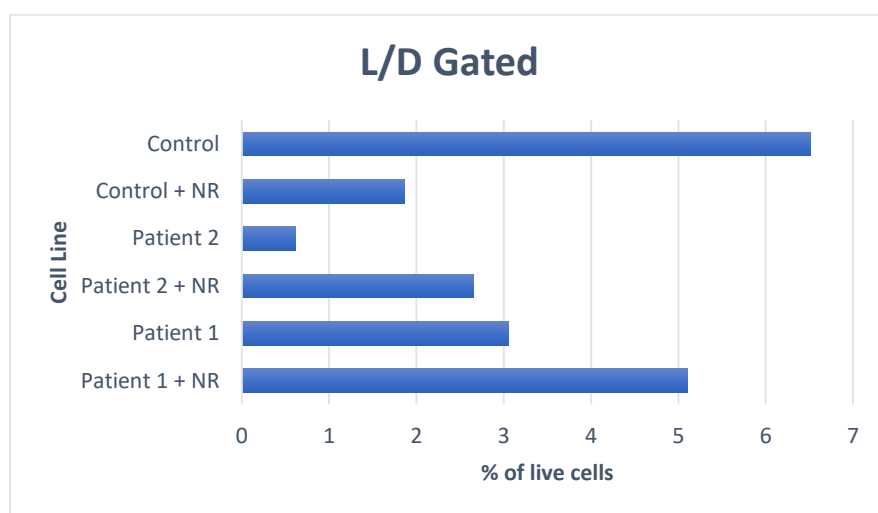

Figure 4.19 Flow cytometry data showing proportion of live cells in each sample as a result of L/D staining, comparing NR treated patient and control COs to untreated COs. X-axis shows the percentage of live cells out of the gated single cell population, and y-axis shows the different cell lines.

Subsequently, we performed MFI-analysis comparing the MFI of NR-treated COs compared to untreated ones to quantify any changes in the organoid composistion. The analysis, presented in **Figure 4.20**, showed a substantial increase in MAP2 expression in both NR-treated patient lines compared to untreated samples. However, the NR-treated control COs showed a significant decrease in MAP2 expression compared to the untreated sample.

Changes were also observed in VDAC expression, where both NR-treated patient lines showed a substantial increase in VDAC expression compared to their untreated counterparts (**Figure 4.20**),

while the NR-treated control showed a decrease in VDAC expression compared to the untreated sample. TFAM expression exhibited an increase in both NR-treated patient samples and NR-treated control sample compared to the untreated samples NR-treated control sample. For NDUFB10 expression, an increase in the NR-treated patient samples compared to the untreated samples, while NR-treated control showed no change in NDUFB10 expression compared to the untreated control.

We gauged the extent of mitochondrial, C1 and mtDNA depletion by normalizing VDAC to MAP2, and TFAM and NDUFB10 to VDAC, as done earlier (**Figure 4.21**). Contrary to the overall expression, VDAC relative to MAP2 decreased in NR-treated patient samples compared to the untreated samples, while NR-treated control showed an increase compared to the untreated control. Similarly, TFAM expression relative to VDAC was seen to decrease in both NR-treated patient samples compared to the untreated samples, while an increased was observed in the NR-treated control, compared to their untreated equivalents. NDUFB10 expression relative to VDAC expression showed a substantial decrease in the NR-treated Patient 2 sample compared to its untreated equivalent, with a slight decrease also seen in the NR-treated Patient 1 sample, albeit to a lesser extent. The NR-treated control group, on the other hand, showed a slight increase in NDUFB10 expression compared to its untreated sample.
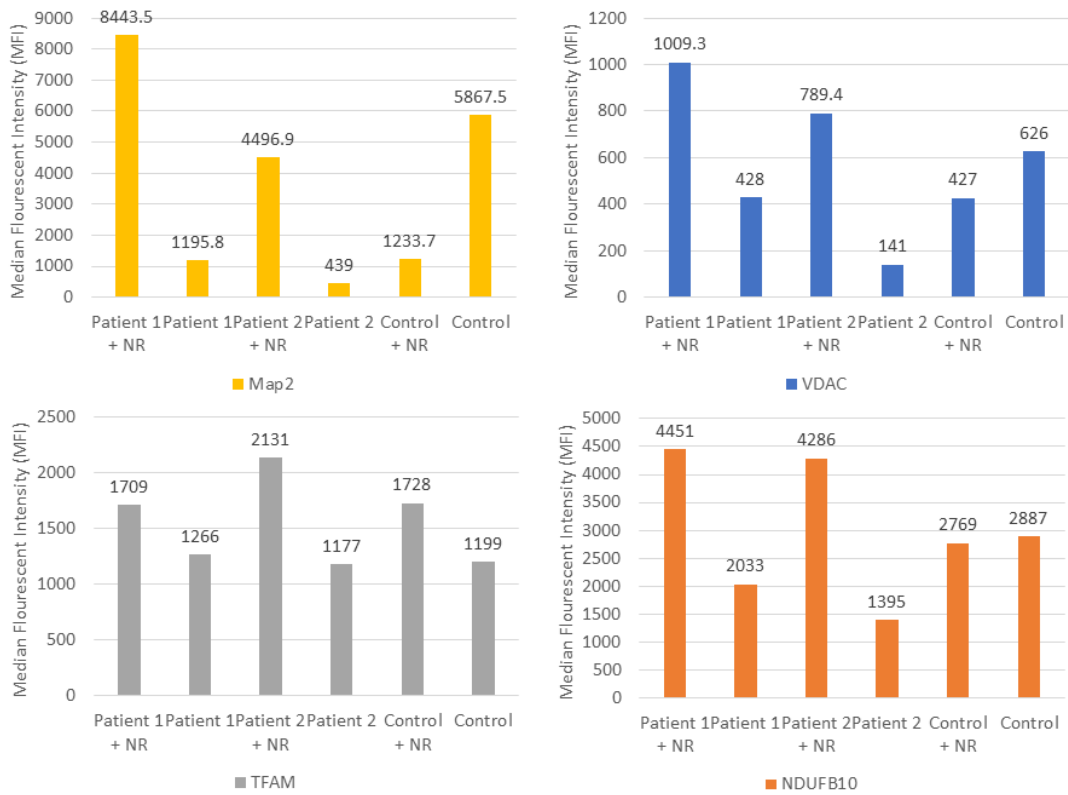
Figure 4.20 Result of flow cytometry analysis for MFI of NR-treated compared to untreated COs. Y-axis shows median fluorescent values for the given stain, and the different cell lines are presented on the X-axis.
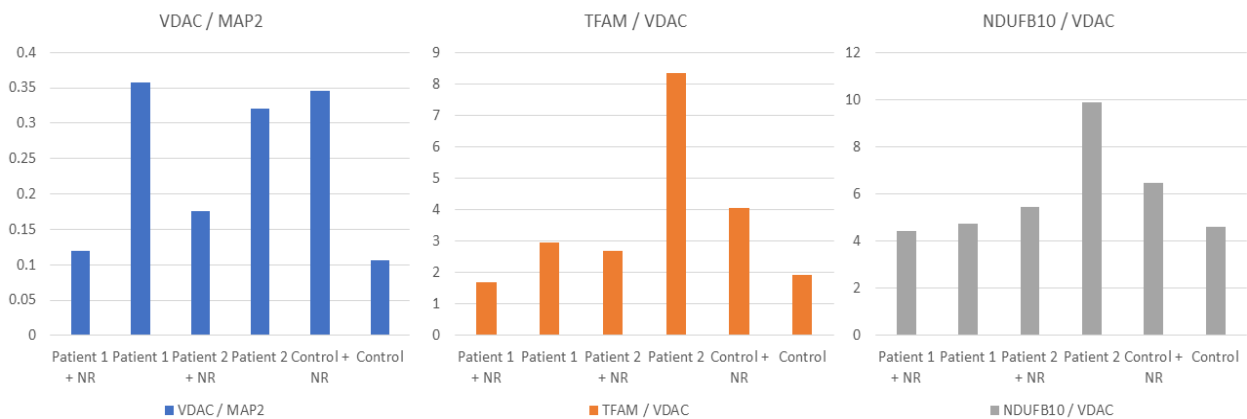

Figure 4.21 Median fluorescent values of COs obtained through flow cytometry giving values of VDAC normalized to MAP2, and TFAM and NDUFB10 normalized to VDAC.

We investigated for mitochondrial, C1, and mtDNA depletion in a similar manner as previously described, comparing NR-treated samples to untreated samples compared to untreated to determine whether NR had an impact on the depletion on the population level (**Figure 4.22**). When looking at the ratio of live cells, we noted a minor increase in the proportion of VDAC in NR-treated patient samples compared to untreated patient samples. On the other hand, the NR-treated control showed a decrease in the proportion of VDAC positive cells relative to MAP2 positive cells.

For the ratio of NDUFB10 positive cells to VDAC positive cells, an increase was noticed in the NR-treated Patient 2 sample when compared to the untreated sample. However, there was negligible to no difference observed in the NR-treated Patient 1 sample and NR-treated control sample when compared to their respective untreated samples (**Figure 4.23**).

Regarding to the ratio of TFAM positive cells to VDAC positive cells, the NR-treated Patient 1 sample showed a decreased amount compared to the untreated sample, while the NR-treated Patient 2 sample demonstrated a lesser decrease relative to the untreated sample. The NR-treated control revealed an increase in TFAM to VDAC expression when compared to the untreated control. These results posed a significant contrast to those found in the MFI-analysis.
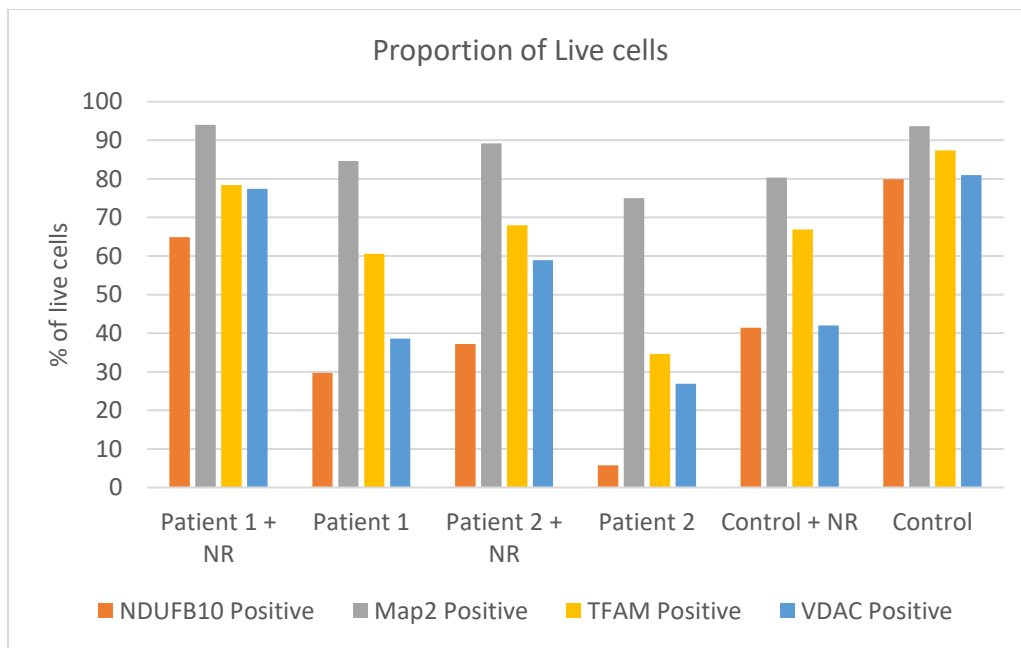

Figure 4.22 shows the proportion of live cell gated positively stained cells based on the gating shown in Figure 3.6.1, *including NR-treated COs. Y-axis shows proportion of cells that stained*

positive for respective markers as percentages of the total live cell population. X-axis shows the different cell lines.
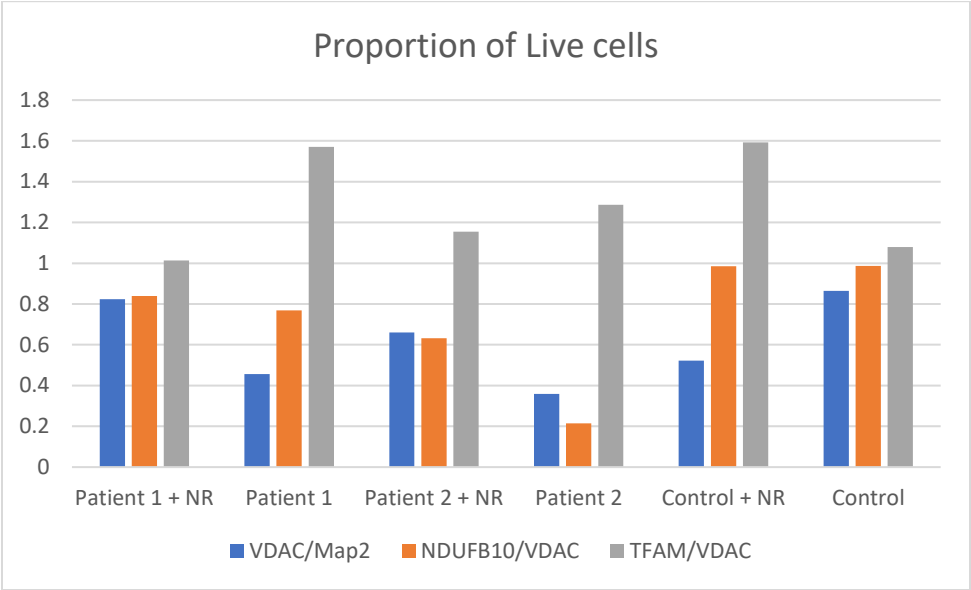
Figure 4.23 *VDAC normalized to MAP2, and TFAM and NDUFB10 normalized to VDAC. Values are calculated from proportions of live cells showing positive expression of each marker.*

Figure 4.24 Values are obtained from measuring different regions of an individual COs of each line. *Boxes show median values and upper and lower quartiles. X indicates the mean value. Whiskers show the highest and lowest values. Dots indicate outlier values. Fluorescent Analysis was performed in ImageJ using the threshold and measure function. The data was represented as mean +/- SD, n= ≥ 4. No significant differences were detected. (Note: Significant differences between patient and control are not given in this figure, see **Figure 4.15**).*

Figure 4.25 Values are obtained from measuring different regions of an individual COs of each line. *Boxes show median values and upper and lower quartiles. X indicates the mean value. Whiskers show the highest and lowest values. Dots indicate outlier values. Fluorescent Ana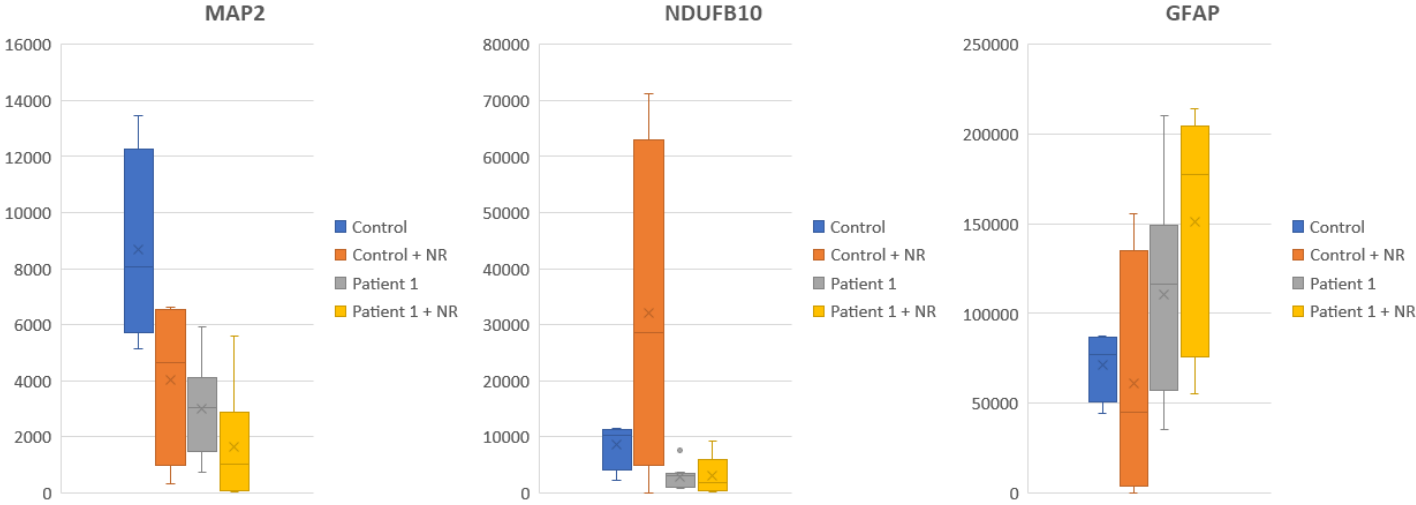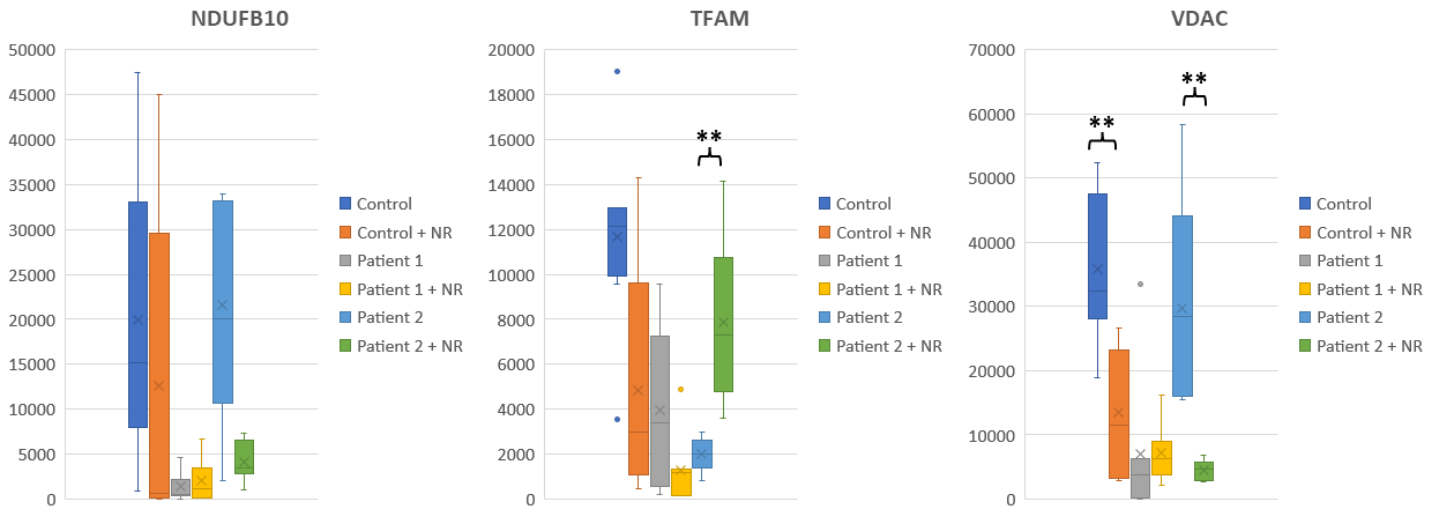lysis was performed in ImageJ using the threshold and measure function. The data was represented as mean +/- SD, n= ≥ 5. Highly significant differences (P ≤ .01) are annotated with (**). (Note: Significant differences between patient and control are not given in this figure, see **Figure 4.16**).*

5. Discussion

5.1 Differentiation protocol of COs

We successfully generated COs from iPSCs by a system of aggregating iPSCs from 2D culture into 3D aggregates. Neural induction was performed on these EBs, before embedding in Matrigel and transferring to spinning culture. The differentiation process was carried out over a period of 40 days, during this period organoids exhibited significant growth and formation of structures reminiscent of brain tissues. Characterization was performed by staining of organoids after 40 days of differentiation with the following markers, MAP2 a marker found in mature neurons, SOX2 a marker for pluripotent or self-renewing cells, and GFAP a marker for glial cells and astrocytes of the brain.

5.2 Differentiation in patient sample compared to controls

In this project we successfully created COs derived from POLG-patient fibroblasts carrying the compound heterozygous mutations p.A467T (c.1399G>A) and p.P589L (c.1766C>T). Both these gene mutations have been associated with AHS (Copeland, n.d.). No substantial differences were

observed between patient lines and the control line in the differentiation stages prior to the maturation stage in spinning culture. We did not find any major differences in size or morphology between patient and control COs during any of the developmental stages. We did however observe that patient line organoids tended to fuse individual organoids together at a greater rate than what we observed in the control COs. We theorize that this increase in fusion might be the result of stimulation of damage associated pathways due to neurodegeneration leading to an increase in cell adhesion, however we have not been able to find any past literature that supports this theory. The cause for these fusions remains unclear, and whether these fusions have an effect on the composition, and arrangement of the COs or not and to what degree is also unclear. Overall, we saw limited changes in the CO cultures, this may be because these cultures are still young at this point of differentiation and the more severe symptoms are yet to manifest at this stage. This is supported by earlier findings that mitochondrial diseases mainly manifest in post-mitotic tissues (Balaban et al., 2005), while our COs still seem to be in an developmental expansion stage.

We were able to show that both patient line and control COs at 40 days after differentiation expressed cells with neuronal morphology with MAP2 expression, as well as containing structures reminiscent of neural tubes although these were only seen with DAPI stain (**Figures 4.3 – 4.5 & 4.7 – 4.9**). From this we can conclude that both patient and control are successfully differentiated into neural organoids. However, universal expression of SOX2 and GFAP indicate that these COs were still at an immature stage at the time of fixation, and that while some neuronal morphology was found it is likely that most of these cells are still at a neural progenitor stage, while GFAP is thought to be an astrocyte specific marker it has been found that it may also be expressed by radial glia cells and neural progenitors in developing organoids (Ma et al., 2022). As GFAP expression appeared to be expressed equally throughout the tissue we were not able to determine whether supportive astrocytes were yet present in these tissues. We also saw a limited permeability for MAP2, GFAP, and SOX2 staining to penetrate to the inner sections of the tissues, as such we have limited information on the layout of these inner regions.

5.3 Flow cytometry showed patient COs had lowered live cell population

Flow cytometric analysis was performed on COs aged 93 days for patient and 65 days for control using BD LSR Fortessa, and analysis were performed in FlowJo. Comparative analysis of patient

and control COs by flow cytometry revealed that all samples expressed a very low live cell percentage from L/D, staining with all COs having less than 10% live cells (**Figures 4.10**). Patient line COs seemed to trend towards having lower live cell population than what we saw in the control. It is unclear exactly why there is such a low live cell population found in the generated COs. One cause might be that due to low access of oxygen and nutrients to inner regions of the COs lead to extensive cell death in the inner regions of the organoids. It has been previously found that limited permeability of organoids often lead to the formation of a necrotic region in the organoid core (Qian et al., 2019; Shi et al., 2020), However with the found 90% and over being dead cells it's unlikely that this is the only cause. Another reason may be a problem with the dissociation protocol. With COs forming complex interconnected tissues with neurons and astrocytes projecting axons and dendrites throughout the tissue, it is possible that these tissues are sensitive to the mechanical force exerted on them during the dissociation protocol leading to the membrane becoming fractured leading to positive L/D staining.

We observed a large decrease in the neuronal marker MAP2, and mitochondrial membrane marker VDAC expression in patient lines than what we observed in the control, suggesting that patient lines had reduced neuronal population, and mitochondrial mass (**Figure 4.11**). However, for C1 marker NDUFB10 we saw a much smaller decrease, while mtDNA marker TFAM showed no change between control and patient (**Figure 4.11**). This is unusual as we would expect with decrease in mitochondrial mass we would at least observe just as big of a decrease in the amount of C1 and mtDNA, unusually when we normalized the NDUFB10, and TFAM expression to VDAC we saw an increase in both compared to control (**Figure 4.12**). We reason that this is most likely a result of auto-fluorescent signal in the channels for VDAC, and TFAM, as even in unstained samples we could see a large expression of these markers (Data not shown), and expression in these channels seemed to increase proportionally to the percentage of dead cells. While we took measures to minimize the amount of autofluorescence by adapting the gating to the unstained samples of each line, we conclude this effort was not enough to completely eliminate the false-positive population. As such it is not possible to conclude from this result whether patient organoids recapitulate depletion of mtDNA or C1 depletion as seen in patient tissues. We used VDAC normalized to MAP2 as a measure of the mitochondrial mass proportionate to the neuronal population (**Figure 4.12**). Here we also observed a large increase in the patient lines compared to what was seen in control. However, we did not observe a large

amount of autofluorescence in the channels for either MAP2 or VDAC, we also did not see the pattern of the proportion rising as the live cell count depleted. The cause of this pattern is unclear. One theory could be that as a result of the dying population, that a pattern of selection occurs, where there is selection pressure towards cells with higher mitochondrial content.

Looking at the proportion of live cells we saw a large decrease in live cells showing positive staining for TFAM, NDUFB10, and VDAC compared to control (**Figure 4.13**). In contrast to the huge decrease of MAP2 expression in the MFI-analysis we only saw a minor decrease in the proportion of live cells that stained positive for MAP2 (**Figure 4.13**). This might indicate that while there is still a substantial neural population, the activity or size of the neurons present might be reduced in the patient organoids. In further contrast looking at the proportion of VDAC positive cells to MAP2 positive cells, we see a decrease in the patient COs compared to the control (**Figure 4.14**). This taken together with the last point might indicate that the increase in VDAC to MAP2 expression seen in the MFI-analysis could be caused by the decrease in neuronal mass causing the mitochondrial mass to appear much larger as a result. Meaning that we might be comparing the mitochondrial content of smaller reduced neurons to larger spanning neurons, leading to what would then appear as an increase in mitochondrial mass is rather caused by a decrease of the neuronal mass. Interestingly, also unlike what we observed in the MFI-analysis we see an overall decrease in TFAM positive cells in patients compared to control, but still an increase when taken into proportion of VDAC positive cells. As well as a decrease in NDUFB10 positive normalized to VDAC positive cells in patients versus control. It is not clear why the dynamics observed in the live cell populations vary so much from what is observed in the MFI-analysis but may also be associated with decreased cellular mass.

5.4 Immunofluorescent staining and MFI analysis

For the MFI analysis we prepared immunohistochemical whole body COs fixed at days 82 for patient, and 52 for control. Images were captured with the Leica TCS SP8 STED 3X fluorescent microscope, and image analysis was performed in ImageJ.

Image analysis of the captured SP8 images revealed a myriad of problems. To select the areas to image we searched for areas with high DAPI staining through the microscope as these we assumed would have high cellular concentration and good stain efficiency. We then adjusted the

z-level to capture the outermost layer as we saw that the inner layers had poor staining efficiency due to limited permeability.

We found that COs expressed a high degree of variability in the efficacy in the quality of staining both between individual COs but also a high degree of heterogeneity in different regions of the same CO, with individual stains showing varying efficiency based on region. We also observed varying degrees of specificity of the staining based on regional distribution, unspecific staining may have been caused by necrotic cells and might be an indication that the observed low live cell count in the flowcytometry analysis may be also present in non-dissociated tissue (Magaki et al., 2019).

One of the factors that played into this was varying permeability of the stains, some stains were only seen to stain the very most outer regions, while others had greater permeability but were still limited to regions surrounding the surface regions of the COs. Another challenge that arose from this was the largely varied topography of the COs, with a high degree of small projecting lobes and general sloped topography at the surface level presented a high degree of difficulty of selecting areas with good staining. We also observed that some regions would produce blurry images when pictured in the microscope, we reached the conclusion that this was also caused by the topography of the organoid in this case causing the coverslip to be placed unevenly at an angle atop the sample. With all of these challenges taken together it was made extremely difficult to locate and select comparable regions when imaging with the SP8. We conclude that the whole-body organoids are not suited for SP8-imaging, and that an alternative methodology should be considered for use in MFI-analysis of fixed immunohistochemical samples. An alternative strategy that may be used is to prepare 2-D slice samples from COs. We presume that this will lessen the complications from topography and dye permeability and as such may be a good option to investigate the inner layers of the COs.

The sample preparation was troubled by issues of the BB containing the antibodies spilling over the liquid blocker surrounding the fixed samples leading to dehydration and incomplete coverage of COs. This may have negatively affected the staining efficiency and might have played a part in the variable degree of staining observed throughout the samples. We also experienced problems where samples would be lost from detaching from the slides during washing steps. We should

explore protocols performing staining in contained environments such as in tubes or well plates to eliminate these challenges.

Taking into account all of the above deliberations I do not believe that the data acquired from the MFI-analysis presents representative results of the COs, and it is currently not possible for us to draw any conclusions based off this data.

5.5 Single cell transcriptomic profiling

The single cell transcriptome profiling analysis showed a complete depletion of DA GLU neurons and a strong decrease in the portion of dopaminergic neurons in the patient line CO. In the human brain dopaminergic neurons are mainly located in the substantia nigra of the midbrain (Chinta and Andersen, 2005), this indicates that organoids bear characteristics of midbrain identity. Depletion of dopaminergic neurons are consistent with earlier findings of dopaminergic neuron loss in POLG patient postmortem brain tissues (Tzoulis et al., 2013). DA GLU co-expressing neurons have been found as a specialized population of neurons in the midbrain with specific projections to the nucleus accumbens (Chuhma et al., 2009; Stuber et al., 2010), further hinting towards mid brain identity. The depletion of these neuronal types in the patient organoid may indicate selective neurodegeneration of dopaminergic neurons or could be indicative of a subtle shift in regional identity. Previous studies have shown an increased tendency for dopaminergic neurons to accumulate mtDNA deletions (Elstner et al., 2011; Reeve et al., 2008), therefore the selective depletion of dopaminergic neurons in patient CO may be caused by increased stress due to defective Pol-γ mtDNA maintenance. We also saw an increase in the glial and astrocyte populations in the patient CO. This increase might be connected to reactive gliosis in response to neurodegeneration (Phatnani and Maniatis, 2015). While it would seem that generated organoids seem to express a midbrain regionality according to the results of this analysis, we see a clear difference in the cellular composition between patient and control organoids. The increase in different cell types as well as the presence of cell types that are not expected to be present in the brain tissue (Melanocytes, Fibroblasts.) may indicate an increase in undirected differentiation in patient organoids.

5.6 Treatment rescue

In this study we investigated the efficacy of NR supplementation as a potential therapeutic approach for treatment of POLG-related disorders.

NR-treatment was not observed to noticeably change the morphological changes seen in patient organoids, namely the increased tendency for patient organoids to fuse together. However, at the point NR-treatment was started at day… several fusions had already occurred. It would be interesting if a rescuing effect can be observed also here if treatment is started earlier.

NR treatment of COs showed a pattern of increased cell survival in patient COs, curiously however we also saw a decrease in the live cell count in the NR treated control CO compared to the untreated control (**Figure 4.19**). NAD+ serves many important functions in the cell, notably it is a critical component in cellular bioenergetics as one of the primary electron donors of the ETC but also serves roles in genomic stability, mitochondrial homeostasis and adaptive stress responses (Lautrup et al., 2019). Due to the critical role of NAD+ in maintaining OXPHOS it is possible that NR supplementation ameliorates the hampered mitochondrial functions caused by *POLG* defects e.g, C1 depletion, and loss of membrane potential leading to lowered ATP production. Thereby leading to a rescuing effect in the patient COs. It is however unclear why we would observe a decrease in cell viability in the NR treated control CO. One theory we propose is similarly linked to the metabolic regulatory effect of NAD+. We suggest that while we see a rescuing effect in the POLG-COs due to increase in metabolic activity, a similar increase in metabolic activity occurs in the supplemented control leading to an over expenditure of nutrients causing starvation. To control for this in the future we should experiment with alternate seeding densities for COs to see if this can lead to an increase in cellular viability.

Flow cytometric analysis revealed similar patterns to what was found earlier for the characterization panel, where we see a strong positive correlation for MAP2 and VDAC expression towards live cell proportion, while there is a strong negative correlation between TFAM and NDUFB expression where lower live cell proportions have high expression of these markers as a result of autofluorescence (**Figure 4.20**). The autofluorescence does not completely overshadow the changes but obscures the difference, especially in the normalized values.

Interestingly we see an even higher expression of MAP2 in one of the NR-supplemented patient lines compared to the untreated control, and higher VDAC expression in both the NR treated patient lines compared to the untreated control, even showing higher proportionate amount when normalizing VDAC to MAP2 (**Figure 4.21**). We also saw a high increase in NDUFB10 expression in the NR-treated patient lines compared to the untreated control, however as discussed before with the decreased live cell count and the resulting autofluorescence it is hard to tell how large this change is in reality. These results suggest that in terms of the neuronal population and mitochondrial mass, NR supplementation had a strong rescuing effect on patient COs. NR-treated samples showing higher expression of MAP2, and VDAC compared to the untreated control indicates that has a greater effect on rescuing the neuronal population and mitochondrial mass than just what is caused by an increase in the live cell population. The higher proportionate amount of VDAC/MAP2 may also be an effect of increased maturity in the patient line COs as these have been cultured for longer.

5.7 Limitations

This study, like any study, had several limitations that must be taken into account when interpreting the results. Some of the main limitations present in this study are discussed below, these include weaknesses from the methodology utilized in this study as well as inherent weaknesses of the organoid modeling system.

Limited repeats and lack of statistical analysis: An important weakness to note in this study is that the analysis performed was only tested on a single repeat for each cell line for every method. Currently organoids as modeling systems are often found to suffer from limited replicability due to a large degree of heterogeneity of cultured tissues (Lancaster et al., 2013). With only one sample it is impossible to know for certain whether the observed effects are due to actual effects brought on by the disease, and subsequently whether the NR-supplementation had a tangible effect or whether these results are due to inherent heterogeneity of the cultured tissues. While the obtained results show a promising trend, there is a need to repeat these studies with more replicates and perform statistical analysis to confirm if these findings are replicable and significant.

Differing organoid ages: Another important point to take into consideration is the varying age from differentiation between patient and control organoid. This variation was caused by

complications in the culturing of organoids leading us to need to establish a new control at a later time point. We recognize that the optimal approach would separate running the tests of the controls and wait until they had reached the same age before running the samples. Unfortunately, time constraints made this impossible, so it is important to keep in mind that some of the differences observed may be caused by patient and control COs being at different differential stages at the time of analysis. The COs used for the scRNA analysis were part of a separate batch that did not suffer from this complication.

Limitations of the organoid modeling system: While organoids provide complex multicellular tissues, they are still limited to modeling only interactions within the tissue and do not for example model interactions with outside systems such as the immune system, endocrine signaling and interactions between different brain regions. As such it may be beneficial in the future to also explore in vivo models and to compare our results with clinical data to validate our results.

With these limitations in mind, it is important to consider these results as preliminary. Although in our opinion they show significant promise as a starting point in our investigations into the use of COs as a system for modeling of POLG-related diseases.

5.8 Future perspectives

Organoid modeling systems are recently emerged systems, and we are still in the early stages of developing this as a robust platform. While organoid cultures have the potential to be extremely powerful tools in the studies of various diseases, cellular and tissue mechanisms, developmental, and drug screening studies. There are still some key challenges that need to be overcome before this platform reaches its full potential. Among the main challenges currently being faced in the generation of organoid cultures are, large heterogeneity between generated samples and lack of standardized methods leading to low replicability (Giandomenico and Lancaster, 2017; Kim et al., 2020). Organoids show a large degree of variance when it comes to size, shape, and structural layout. An example of this is that in the human embryonic development neurogenesis originates from a singular tube, while in organoids there are several neural tube-like structures present the quantity of which vary highly from organoid to organoid. Another key challenge is the limited lifespan of organoids. A key component behind this is thought to be the limited nutrient availability and limited oxygen supply to central organoids tissues, forming a central hypoxic zone. These hypoxic zones suffer from limited energy supply due to lack of nutrients and a lack

of oxygen to drive OXPHOS. The limited oxygen supply also affects the differentiation ability of neural progenitors and may limit the migration of axons through these hypoxic zones (Giandomenico and Lancaster, 2017). A lot of work is currently being put into this field in attempt to overcome these challenges, of course in native human tissues this is overcome through vascularization of the tissue allowing steady supply of oxygen and nutrients to be diffused through the blood. In organoids there are also attempts to establish vascularized structures to mediate these supply requirements. Recently a platform for creating blood vessel organoids has been developed (Wimmer et al., 2019), and efforts are being made to create organoids that contain endothelium capable of differentiating into tissue specific vasculature (Garreta et al., 2021), recently developments have been made to generate vascularized organoids (Strobel et al., 2023) including a successful generation of vascularized COs that facilitated oxygen-nutrient transport, with a lifespan of over 200 days in culture (Shi et al., 2020). Another method that has been used is the application of in vivo vascularization by implantation into a host. Brain organoids implanted into mouse brain have in a recent study been shown to form vasculature as well as forming functional neuronal projections to surrounding brain tissues when implanted in the brain of immunodeficient mice (Mansour et al., 2018), however this method is less desirable for large scale studies, due to costs, the use of animals, and the specialization needed for surgery. It does, however, provide a system for studying intersystem interactions. There has also been made progress in developing ways to enhance oxygen-nutrient supply without the induction of vasculature, a protocol has been established for slice culturing of cerebral organoids at the air liquid interface. Shortly organoids at the maturation stage are cut into slices which are then cultured at a membrane that keep the slices in contact with the medium but not submerged to facilitate nutrient availability, the slices not being submerged facilitates greater oxygen transport from the air. Cerebral organoids cultured in this manner showed increased survival, and where found to form neural circuits both within and between slices (Giandomenico et al., 2019). These studies should be taken into consideration as we continue to seek ways to enhance our study and to optimize our protocols.

Once we have established a robust system for modeling of POLG-disease there are many directions we could explore in the future. It would be interesting to extend our scRNA studies to look more into the mechanistic functions of POLG-diseases and investigating differential gene expression and epigenetic factors to further our understanding of the underlying mechanisms of

POLG-related diseases. It will also be interesting to further investigate NR-supplemented samples to receive a better understanding of the rescuing effects.

As discussed POLG-diseases are extremely heterogenous when it comes to both phenotype and age of onset. In this study we have only studied two clones of the same mutation, as well as have done this in a very limited time frame. As such we do not yet know how our findings relate to POLG-related disease as a whole, or how indicative the time points of our study have been. It is possible that the phenotype brought on in the patient sample is still in the early phases, and it would be interesting to conduct a longitudinal study to see how this progresses and if the rescuing effects of NR maintain efficacy over time. In this situation it would be fascinating to compare organoids generated from a patient expressing early onset POLG-disease versus a patient expressing a late onset variation. POLG-diseases also affect a variety of tissues outside the brain, notably including skeletal muscle and liver. It would be an interesting prospect for the future to extend our study to both varied tissues of the brain, as well as comparing these to outside tissues to compare the levels of effect.

Another exciting prospect is the potential utilization within the fields of drug screening and the development of personalized medicine. Once a robust platform has been established, we have the potential to upscale it to perform high-throughput drug screening, with potential to aid in the discovery of novel drugs for treatment of POLG-related diseases. Further, with the capability of establishing patient specific organoids, we open the door to investigations of personalized medicine specifically screened on a per patient basis.

6. Conclusion

In this study we successfully differentiated patient derived iPSCs into COs, using iPSCs reprogrammed from patient fibroblasts carrying the mutations p.A467T (c.1399G>A) and p.P589L (c.1766C>T). Controls were generated from commercially available fibroblasts CRL2097 fibroblasts.

We showed that both patient and control organoids generated using our methods produce tissues resembling the cortical region of the brain, showing positive staining of the markers MAP2, SOX2, and GFAP, as well as distinct structures resembling neural tubes in both patient and control indicating successful CO differentiation. We saw a trend towards lower cell viability in

patient COs, and reduced expression of MAP2, VDAC, NDUFB10, and TFAM compared to control COs. Indicating loss of neuronal population, mitochondrial mass, C1 depletion and mtDNA depletion, respectively. However, these changes did not remain when normalizing to neuronal mass and mitochondrial mass, we suspect due to confounding factors including autofluorescence. NR-supplementation seemed to have a rescuing effect in patient COs, showing increased cell viability and increased MAP2, VDAC, NDUFB10, and TFAM expression compared to the untreated samples. NR-supplementation was seen to have a negative effect on the control sample, reducing cell viability and lowered expression of MAP2, and VDAC while showing an increase in TFAM expression.

scRNA-analysis revealed that generated COs contained substantial dopaminergic neuron population, accompanied by smaller populations of DA GLU co-expressing neurons and glutaminergic neurons. Glutaminergic and DA GLU populations strongly imply midbrain regional identity. Patient COs expressed complete depletion of the DA GLU neuronal population and a strong depletion of dopaminergic neurons, replaced by an increase in glutaminergic neurons and GABAergic interneurons. Dopaminergic neuron depletion is consistent with earlier findings of dopaminergic neuron loss in patient postmortem tissues indicating a replication of POLG-phenotype in generated COs. Patient COs were also seen to have increased astrocyte/glial population consistent with gliosis as well as presence of fibroblasts and melanocytes potentially indicating undirected differentiation.

The conducted study had several limitations including limited replicates, and differing ages of analyzed COs. We also experienced several complications with the utilized protocols. The results presented are therefore meant to be taken as preliminary and further studies are required to confirm these results. While there are still several challenges to overcome, we expect that with further effort that the developed model system will become a powerful tool for both studying the mechanisms of disease in POLG-related disorders, as well as provide a beneficial platform for testing of novel treatments.

7. References

Ahmad, M., Wolberg, A., Kahwaji, C.I., 2023. Biochemistry, Electron Transport Chain, in: StatPearls. StatPearls Publishing, Treasure Island (FL).

Alberts, B., Johnson, A., Lewis, J., Raff, M., Roberts, K., Walter, P., 2002. Molecular Biology of the Cell, 4th ed. Garland Science.

Balaban, R.S., Nemoto, S., Finkel, T., 2005. Mitochondria, Oxidants, and Aging. Cell 120, 483–495. https://doi.org/10.1016/j.cell.2005.02.001

Berridge, M.J., Bootman, M.D., Roderick, H.L., 2003. Calcium signalling: dynamics, homeostasis and remodelling. Nat Rev Mol Cell Biol 4, 517–529. https://doi.org/10.1038/nrm1155

Bieganowski, P., Brenner, C., 2004. Discoveries of Nicotinamide Riboside as a Nutrient and Conserved NRK Genes Establish a Preiss-Handler Independent Route to NAD+ in Fungi and Humans. Cell 117, 495–502. https://doi.org/10.1016/S0092-8674(04)00416-7

Bogenhagen, D., Clayton, D.A., 1974. The Number of Mitochondrial Deoxyribonucleic Acid Genomes in Mouse L and Human HeLa Cells. Journal of Biological Chemistry 249, 7991–7995. https://doi.org/10.1016/S0021-9258(19)42063-2

Calvo, S.E., Clauser, K.R., Mootha, V.K., 2016. MitoCarta2.0: an updated inventory of mammalian mitochondrial proteins. Nucleic Acids Res 44, D1251–D1257. https://doi.org/10.1093/nar/gkv1003

Cavalier-Smith, T., 2006. Origin of mitochondria by intracellular enslavement of a photosynthetic purple bacterium. Proc Biol Sci 273, 1943–1952. https://doi.org/10.1098/rspb.2006.3531

Chan, S.S.L., Copeland, W.C., 2009. DNA polymerase gamma and mitochondrial disease: understanding the consequence of POLG mutations. Biochim Biophys Acta 1787, 312–319. https://doi.org/10.1016/j.bbabio.2008.10.007

Chinnery, P.F., 1993. Primary Mitochondrial Disorders Overview, in: Adam, M.P., Mirzaa, G.M., Pagon, R.A., Wallace, S.E., Bean, L.J., Gripp, K.W., Amemiya, A. (Eds.), GeneReviews®. University of Washington, Seattle, Seattle (WA).

Chinta, S.J., Andersen, J.K., 2005. Dopaminergic neurons. The International Journal of Biochemistry & Cell Biology, Cancer and Aging at the Crossroads 37, 942–946. https://doi.org/10.1016/j.biocel.2004.09.009

Chocron, E.S., Munkácsy, E., Pickering, A.M., 2019. Cause or casualty: The role of mitochondrial DNA in aging and age-associated disease. Biochimica et Biophysica Acta (BBA) - Molecular Basis of Disease 1865, 285–297. https://doi.org/10.1016/j.bbadis.2018.09.035

Chuhma, N., Choi, W.Y., Mingote, S., Rayport, S., 2009. DOPAMINE NEURON GLUTAMATE COTRANSMISSION: FREQUENCY-DEPENDENT MODULATION IN THE MESOVENTROMEDIAL PROJECTION. Neuroscience 164, 1068–1083. https://doi.org/10.1016/j.neuroscience.2009.08.057

Claassen, D.A., Desler, M.M., Rizzino, A., 2009. ROCK Inhibition Enhances the Recovery and Growth of Cryopreserved Human Embryonic Stem Cells and Human Induced Pluripotent Stem Cells. Mol Reprod Dev 76, 722–732. https://doi.org/10.1002/mrd.21021

Copeland, B., n.d. Human DNA Polymerase Gamma Mutation Database [WWW Document]. National Institute of Environmental Health Sciences. URL https://tools.niehs.nih.gov/polg/index.cfm (accessed 6.14.23).

Culturing Pluripotent Stem Cells (PSCs) in Essential 8^{TM} Medium - NO [WWW Document], 2016. . ThermoFisher Scientific. URL https://www.thermofisher.com/uk/en/home/references/protocols/cell-culture/stem-cell-protocols/ipsc-protocols/culturing-puripotent-stem-cells-essential-8-medium.html (accessed 5.5.23).

D'Autréaux, B., Toledano, M.B., 2007. ROS as signalling molecules: mechanisms that generate specificity in ROS homeostasis. Nat Rev Mol Cell Biol 8, 813–824. https://doi.org/10.1038/nrm2256

Dawson, T.M., Golde, T.E., Tourenne, C.L., 2018. Animal Models of Neurodegenerative Diseases. Nat Neurosci 21, 1370–1379. https://doi.org/10.1038/s41593-018-0236-8

Eichmüller, O.L., Knoblich, J.A., 2022. Human cerebral organoids — a new tool for clinical neurology research. Nat Rev Neurol 18, 661–680. https://doi.org/10.1038/s41582-022-00723-9

Elstner, M., Müller, S.K., Leidolt, L., Laub, C., Krieg, L., Schlaudraff, F., Liss, B., Morris, C., Turnbull, D.M., Masliah, E., Prokisch, H., Klopstock, T., Bender, A., 2011. Neuromelanin, neurotransmitter status and brainstem location determine the differential vulnerability of catecholaminergic neurons to mitochondrial DNA deletions. Mol Brain 4, 43. https://doi.org/10.1186/1756-6606-4-43

Euro, L., Farnum, G.A., Palin, E., Suomalainen, A., Kaguni, L.S., 2011. Clustering of Alpers disease mutations and catalytic defects in biochemical variants reveal new features of molecular mechanism of the human mitochondrial replicase, Pol γ. Nucleic Acids Res 39, 9072–9084. https://doi.org/10.1093/nar/gkr618

Falkenberg, M., Larsson, N.-G., Gustafsson, C.M., 2007. DNA Replication and Transcription in Mammalian Mitochondria. Annual Review of Biochemistry 76, 679–699. https://doi.org/10.1146/annurev.biochem.76.060305.152028

Fang, E.F., Lautrup, S., Hou, Y., Demarest, T.G., Croteau, D.L., Mattson, M.P., Bohr, V.A., 2017. NAD+ in Aging: Molecular Mechanisms and Translational Implications. Trends Mol Med 23, 899–916. https://doi.org/10.1016/j.molmed.2017.08.001

Fusté, J.M., Wanrooij, S., Jemt, E., Granycome, C.E., Cluett, T.J., Shi, Y., Atanassova, N., Holt, I.J., Gustafsson, C.M., Falkenberg, M., 2010. Mitochondrial RNA Polymerase Is Needed for Activation of the Origin of Light-Strand DNA Replication. Molecular Cell 37, 67–78. https://doi.org/10.1016/j.molcel.2009.12.021

Garreta, E., Kamm, R.D., Chuva de Sousa Lopes, S.M., Lancaster, M.A., Weiss, R., Trepat, X., Hyun, I., Montserrat, N., 2021. Rethinking organoid technology through bioengineering. Nat. Mater. 20, 145–155. https://doi.org/10.1038/s41563-020-00804-4

Giandomenico, S.L., Lancaster, M.A., 2017. Probing human brain evolution and development in organoids. Current Opinion in Cell Biology, Cell Architecture 44, 36–43. https://doi.org/10.1016/j.ceb.2017.01.001

Giandomenico, S.L., Mierau, S.B., Gibbons, G.M., Wenger, L.M.D., Masullo, L., Sit, T., Sutcliffe, M., Boulanger, J., Tripodi, M., Derivery, E., Paulsen, O., Lakatos, A., Lancaster, M.A., 2019. Cerebral organoids at the air-liquid interface generate diverse nerve tracts with functional output. Nat Neurosci 22, 669–679. https://doi.org/10.1038/s41593-019-0350-2

Gonzalez, C., Armijo, E., Bravo-Alegria, J., Becerra-Calixto, A., Mays, C.E., Soto, C., 2018. Modeling amyloid beta and tau pathology in human cerebral organoids. Mol Psychiatry 23, 2363–2374. https://doi.org/10.1038/s41380-018-0229-8

Guerrero-Castillo, S., Baertling, F., Kownatzki, D., Wessels, H.J., Arnold, S., Brandt, U., Nijtmans, L., 2017. The Assembly Pathway of Mitochondrial Respiratory Chain Complex I. Cell Metabolism 25, 128–139. https://doi.org/10.1016/j.cmet.2016.09.002

Halevy, T., Urbach, A., 2014. Comparing ESC and iPSC—Based Models for Human Genetic Disorders. J Clin Med 3, 1146–1162. https://doi.org/10.3390/jcm3041146

Hanifah, Z., n.d. Table A5.07: Critical Values for the Wilcoxon/Mann-Whitney Test (U.

Hikmat, O., Tzoulis, C., Chong, W.K., Chentouf, L., Klingenberg, C., Fratter, C., Carr, L.J., Prabhakar, P., Kumaraguru, N., Gissen, P., Cross, J.H., Jacques, T.S., Taanman, J.-W., Bindoff, L.A., Rahman, S., 2017. The clinical spectrum and natural history of early-onset diseases due to DNA polymerase gamma mutations. Genetics in Medicine 19, 1217–1225. https://doi.org/10.1038/gim.2017.35

Hollenbeck, P.J., Saxton, W.M., 2005. The axonal transport of mitochondria. J Cell Sci 118, 5411–5419. https://doi.org/10.1242/jcs.02745

Hou, Y., Lautrup, S., Cordonnier, S., Wang, Y., Croteau, D.L., Zavala, E., Zhang, Y., Moritoh, K., O'Connell, J.F., Baptiste, B.A., Stevnsner, T.V., Mattson, M.P., Bohr, V.A., 2018. NAD+ supplementation normalizes key Alzheimer's features and DNA damage responses in a new AD mouse model with introduced DNA repair deficiency. Proc Natl Acad Sci U S A 115, E1876–E1885. https://doi.org/10.1073/pnas.1718819115

Kaguni, L.S., 2004. DNA Polymerase γ, The Mitochondrial Replicase. Annual Review of Biochemistry 73, 293–320. https://doi.org/10.1146/annurev.biochem.72.121801.161455

Khan, N.A., Auranen, M., Paetau, I., Pirinen, E., Euro, L., Forsström, S., Pasila, L., Velagapudi, V., Carroll, C.J., Auwerx, J., Suomalainen, A., 2014. Effective treatment of mitochondrial myopathy by nicotinamide riboside, a vitamin B3. EMBO Mol Med 6, 721–731. https://doi.org/10.1002/emmm.201403943

Kim, J., Koo, B.-K., Knoblich, J.A., 2020. Human organoids: model systems for human biology and medicine. Nat Rev Mol Cell Biol 21, 571–584. https://doi.org/10.1038/s41580-020-0259-3

Kunitomi, A., Hirohata, R., Arreola, V., Osawa, M., Kato, T.M., Nomura, M., Kawaguchi, J., Hara, H., Kusano, K., Takashima, Y., Takahashi, K., Fukuda, K., Takasu, N., Yamanaka, S., 2022. Improved Sendai viral system for reprogramming to naive pluripotency. Cell Reports Methods 2, 100317. https://doi.org/10.1016/j.crmeth.2022.100317

Lancaster, M.A., Renner, M., Martin, C.-A., Wenzel, D., Bicknell, L.S., Hurles, M.E., Homfray, T., Penninger, J.M., Jackson, A.P., Knoblich, J.A., 2013. Cerebral organoids model human brain development and microcephaly. Nature 501, 10.1038/nature12517. https://doi.org/10.1038/nature12517

Lasserre, J.-P., Dautant, A., Aiyar, R.S., Kucharczyk, R., Glatigny, A., Tribouillard-Tanvier, D., Rytka, J., Blondel, M., Skoczen, N., Reynier, P., Pitayu, L., Rötig, A., Delahodde, A., Steinmetz, L.M., Dujardin, G., Procaccio, V., di Rago, J.-P., 2015. Yeast as a system for modeling mitochondrial disease mechanisms and discovering therapies. Dis Model Mech 8, 509–526. https://doi.org/10.1242/dmm.020438

Lautrup, S., Sinclair, D.A., Mattson, M.P., Fang, E.F., 2019. NAD+ in Brain Aging and Neurodegenerative Disorders. Cell Metab 30, 630–655. https://doi.org/10.1016/j.cmet.2019.09.001

Lee, J.-H., Sun, W., 2022. Neural Organoids, a Versatile Model for Neuroscience. Mol Cells 45, 53–64. https://doi.org/10.14348/molcells.2022.2019

Li, X., Meng, G., Krawetz, R., Liu, S., Rancourt, D.E., 2008. The ROCK Inhibitor Y-27632 Enhances the Survival Rate of Human Embryonic Stem Cells Following

Cryopreservation. Stem Cells and Development 17, 1079–1086. https://doi.org/10.1089/scd.2007.0247

Liang, K.X., Kristiansen, C.K., Mostafavi, S., Vatne, G.H., Zantingh, G.A., Kianian, A., Tzoulis, C., Høyland, L.E., Ziegler, M., Perez, R.M., Furriol, J., Zhang, Z., Balafkan, N., Hong, Y., Siller, R., Sullivan, G.J., Bindoff, L.A., 2020. Disease-specific phenotypes in iPSC-derived neural stem cells with POLG mutations. EMBO Mol Med 12, e12146. https://doi.org/10.15252/emmm.202012146

Lim, S.E., Longley, M.J., Copeland, W.C., 1999. The Mitochondrial p55 Accessory Subunit of Human DNA Polymerase γ Enhances DNA Binding, Promotes Processive DNA Synthesis, and Confers N-Ethylmaleimide Resistance *. Journal of Biological Chemistry 274, 38197–38203. https://doi.org/10.1074/jbc.274.53.38197

Longley, M.J., Graziewicz, M.A., Bienstock, R.J., Copeland, W.C., 2005. Consequences of mutations in human DNA polymerase γ. Gene, Cross-Talk between Nucleus and Organelles 354, 125–131. https://doi.org/10.1016/j.gene.2005.03.029

Ma, H., Chen, J., Deng, Z., Sun, T., Luo, Q., Gong, H., Li, X., Long, B., 2022. Multiscale Analysis of Cellular Composition and Morphology in Intact Cerebral Organoids. Biology (Basel) 11, 1270. https://doi.org/10.3390/biology11091270

Magaki, S., Hojat, S.A., Wei, B., So, A., Yong, W.H., 2019. An Introduction to the Performance of Immunohistochemistry. Methods Mol Biol 1897, 289–298. https://doi.org/10.1007/978-1-4939-8935-5_25

Mansour, A.A., Gonçalves, J.T., Bloyd, C.W., Li, H., Fernandes, S., Quang, D., Johnston, S., Parylak, S.L., Jin, X., Gage, F.H., 2018. An in vivo model of functional and vascularized human brain organoids. Nat Biotechnol 36, 432–441. https://doi.org/10.1038/nbt.4127

Nicholas Russo, S., Shah, E.G., Copeland, W.C., Koenig, M.K., 2022. A new pathogenic POLG variant. Mol Genet Metab Rep 32, 100890. https://doi.org/10.1016/j.ymgmr.2022.100890

Nikiforov, A., Dölle, C., Niere, M., Ziegler, M., 2011. Pathways and subcellular compartmentation of NAD biosynthesis in human cells: from entry of extracellular precursors to mitochondrial NAD generation. J Biol Chem 286, 21767–21778. https://doi.org/10.1074/jbc.M110.213298

Parikh, S., Goldstein, A., Koenig, M.K., Scaglia, F., Enns, G.M., Saneto, R., Anselm, I., Cohen, B.H., Falk, M.J., Greene, C., Gropman, A.L., Haas, R., Hirano, M., Morgan, P., Sims, K., Tarnopolsky, M., Van Hove, J.L.K., Wolfe, L., DiMauro, S., 2015. Diagnosis and management of mitochondrial disease: a consensus statement from the Mitochondrial Medicine Society. Genet Med 17, 689–701. https://doi.org/10.1038/gim.2014.177

Phatnani, H., Maniatis, T., 2015. Astrocytes in Neurodegenerative Disease. Cold Spring Harb Perspect Biol 7, a020628. https://doi.org/10.1101/cshperspect.a020628

Pizzino, G., Irrera, N., Cucinotta, M., Pallio, G., Mannino, F., Arcoraci, V., Squadrito, F., Altavilla, D., Bitto, A., 2017. Oxidative Stress: Harms and Benefits for Human Health. Oxid Med Cell Longev 2017, 8416763. https://doi.org/10.1155/2017/8416763

Preiss, J., Handler, P., 1958. Biosynthesis of Diphosphopyridine Nucleotide. Journal of Biological Chemistry 233, 488–492. https://doi.org/10.1016/S0021-9258(18)64789-1

Progressive external ophthalmoplegia: MedlinePlus Genetics [WWW Document], n.d. . MedlinePlus. URL https://medlineplus.gov/genetics/condition/progressive-external-ophthalmoplegia/ (accessed 6.15.23).

Protasoni, M., Zeviani, M., 2021. Mitochondrial Structure and Bioenergetics in Normal and Disease Conditions. Int J Mol Sci 22, 586. https://doi.org/10.3390/ijms22020586

Protocol for Neural Organoid Culture [WWW Document], 2020. . Stemcell Technologies. URL
https://www.stemcell.com/neural-organoid-culture.html (accessed 5.5.23).

Qian, X., Song, H., Ming, G., 2019. Brain organoids: advances, applications and challenges.
Development 146, dev166074. https://doi.org/10.1242/dev.166074

Quadrato, G., Nguyen, T., Macosko, E.Z., Sherwood, J.L., Min Yang, S., Berger, D.R., Maria,
N., Scholvin, J., Goldman, M., Kinney, J.P., Boyden, E.S., Lichtman, J.W., Williams,
Z.M., McCarroll, S.A., Arlotta, P., 2017. Cell diversity and network dynamics in
photosensitive human brain organoids. Nature 545, 48–53.
https://doi.org/10.1038/nature22047

Rahman, S., Copeland, W.C., 2019. POLG-related disorders and their neurological
manifestations. Nat Rev Neurol 15, 40–52. https://doi.org/10.1038/s41582-018-0101-0

Reeve, A.K., Krishnan, K.J., Elson, J.L., Morris, C.M., Bender, A., Lightowlers, R.N., Turnbull,
D.M., 2008. Nature of Mitochondrial DNA Deletions in Substantia Nigra Neurons. Am J
Hum Genet 82, 228–235. https://doi.org/10.1016/j.ajhg.2007.09.018

Rossignol, R., Faustin, B., Rocher, C., Malgat, M., Mazat, J.-P., Letellier, T., 2003.
Mitochondrial threshold effects. Biochem J 370, 751–762.
https://doi.org/10.1042/BJ20021594

Russell, O.M., Gorman, G.S., Lightowlers, R.N., Turnbull, D.M., 2020. Mitochondrial Diseases:
Hope for the Future. Cell 181, 168–188. https://doi.org/10.1016/j.cell.2020.02.051

Schöndorf, D.C., Ivanyuk, D., Baden, P., Sanchez-Martinez, A., Cicco, S.D., Yu, C., Giunta, I.,
Schwarz, L.K., Napoli, G.D., Panagiotakopoulou, V., Nestel, S., Keatinge, M., Pruszak,
J., Bandmann, O., Heimrich, B., Gasser, T., Whitworth, A.J., Deleidi, M., 2018. The
NAD+ Precursor Nicotinamide Riboside Rescues Mitochondrial Defects and Neuronal
Loss in iPSC and Fly Models of Parkinson's Disease. Cell Reports 23, 2976–2988.
https://doi.org/10.1016/j.celrep.2018.05.009

Shi, Y., Sun, L., Wang, M., Liu, J., Zhong, S., Li, R., Li, P., Guo, L., Fang, A., Chen, R., Ge, W.-
P., Wu, Q., Wang, X., 2020. Vascularized human cortical organoids (vOrganoids) model
cortical development in vivo. PLoS Biol 18, e3000705.
https://doi.org/10.1371/journal.pbio.3000705

Silva-Pinheiro, P., Pardo-Hernández, C., Reyes, A., Tilokani, L., Mishra, A., Cerutti, R., Li, S.,
Rozsivalova, D.-H., Valenzuela, S., Dogan, S.A., Peter, B., Fernández-Silva, P.,
Trifunovic, A., Prudent, J., Minczuk, M., Bindoff, L., Macao, B., Zeviani, M.,
Falkenberg, M., Viscomi, C., 2021. DNA polymerase gamma mutations that impair
holoenzyme stability cause catalytic subunit depletion. Nucleic Acids Res 49, 5230–5248.
https://doi.org/10.1093/nar/gkab282

Strobel, H.A., Moss, S.M., Hoying, J.B., 2023. Vascularized Tissue Organoids. Bioengineering
(Basel) 10, 124. https://doi.org/10.3390/bioengineering10020124

Stuber, G.D., Hnasko, T.S., Britt, J.P., Edwards, R.H., Bonci, A., 2010. Dopaminergic terminals
in the nucleus accumbens but not the dorsal striatum corelease glutamate. J Neurosci 30,
8229–8233. https://doi.org/10.1523/JNEUROSCI.1754-10.2010

Stumpf, J.D., Saneto, R.P., Copeland, W.C., 2013. Clinical and Molecular Features of POLG-
Related Mitochondrial Disease. Cold Spring Harb Perspect Biol 5, a011395.
https://doi.org/10.1101/cshperspect.a011395

Takahashi, K., Tanabe, K., Ohnuki, M., Narita, M., Ichisaka, T., Tomoda, K., Yamanaka, S.,
2007. Induction of Pluripotent Stem Cells from Adult Human Fibroblasts by Defined
Factors. Cell 131, 861–872. https://doi.org/10.1016/j.cell.2007.11.019

Takahashi, K., Yamanaka, S., 2006. Induction of Pluripotent Stem Cells from Mouse Embryonic and Adult Fibroblast Cultures by Defined Factors. Cell 126, 663–676. https://doi.org/10.1016/j.cell.2006.07.024

Tilokani, L., Nagashima, S., Paupe, V., Prudent, J., 2018. Mitochondrial dynamics: overview of molecular mechanisms. Essays Biochem 62, 341–360. https://doi.org/10.1042/EBC20170104

Tzoulis, C., Tran, G.T., Schwarzlmüller, T., Specht, K., Haugarvoll, K., Balafkan, N., Lilleng, P.K., Miletic, H., Biermann, M., Bindoff, L.A., 2013. Severe nigrostriatal degeneration without clinical parkinsonism in patients with polymerase gamma mutations. Brain 136, 2393–2404. https://doi.org/10.1093/brain/awt103

Verdin, E., 2015. NAD$^+$ in aging, metabolism, and neurodegeneration. Science 350, 1208–1213. https://doi.org/10.1126/science.aac4854

Vinothkumar, K.R., Zhu, J., Hirst, J., 2014. Architecture of mammalian respiratory complex I. Nature 515, 80–84. https://doi.org/10.1038/nature13686

Walters, G.C., Usachev, Y.M., 2023. Mitochondrial calcium cycling in neuronal function and neurodegeneration. Front Cell Dev Biol 11, 1094356. https://doi.org/10.3389/fcell.2023.1094356

Wimmer, R.A., Leopoldi, A., Aichinger, M., Wick, N., Hantusch, B., Novatchkova, M., Taubenschmid, J., Hämmerle, M., Esk, C., Bagley, J.A., Lindenhofer, D., Chen, G., Boehm, M., Agu, C.A., Yang, F., Fu, B., Zuber, J., Knoblich, J.A., Kerjaschki, D., Penninger, J.M., 2019. Human blood vessel organoids as a model of diabetic vasculopathy. Nature 565, 505–510. https://doi.org/10.1038/s41586-018-0858-8

Xiang, Y., Yoshiaki, T., Patterson, B., Cakir, B., Kim, K.-Y., Cho, Y.S., Park, I.-H., 2018. Generation and Fusion of Human Cortical and Medial Ganglionic Eminence Brain Organoids. Curr Protoc Stem Cell Biol 47, e61. https://doi.org/10.1002/cpsc.61

Yi, M., Weaver, D., Hajnóczky, G., 2004. Control of mitochondrial motility and distribution by the calcium signal. J Cell Biol 167, 661–672. https://doi.org/10.1083/jcb.200406038

Yu, D.X., Di Giorgio, F.P., Yao, J., Marchetto, M.C., Brennand, K., Wright, R., Mei, A., Mchenry, L., Lisuk, D., Grasmick, J.M., Silberman, P., Silberman, G., Jappelli, R., Gage, F.H., 2014. Modeling Hippocampal Neurogenesis Using Human Pluripotent Stem Cells. Stem Cell Reports 2, 295–310. https://doi.org/10.1016/j.stemcr.2014.01.009